INVESTIGATING THE CHANGES IN MATRIX AND FRACTURE PROPERTIES AND FLUID FLOW UNDER DIFFERENT STRESS-STATE CONDITIONS

A Thesis

by

VIVEK MURALIDHARAN

Submitted to the Office of Graduate Studies of
Texas A&M University
in partial fulfillment of the requirements for the degree of

MASTER OF SCIENCE

August 2004

Major Subject: Petroleum Engineering

INVESTIGATING THE CHANGES IN MATRIX AND FRACTURE PROPERTIES AND FLUID FLOW UNDER DIFFERENT STRESS-STATE CONDITIONS

A Thesis

by

VIVEK MURALIDHARAN

Submitted to Texas A&M University
in partial fulfillment of the requirements
for the degree of

MASTER OF SCIENCE

Approved as to style and content by:

David S. Schechter (Chair of Committee)	Daulat D. Mamora (Member)
Robert R.Berg (Member)	Stephen A. Holditch (Head of Department)

August 2004

Major Subject: Petroleum Engineering

ABSTRACT

Investigating the Changes in Matrix and Fracture Properties and Fluid Flow Under Different Stress-state Conditions. (August 2004)

Vivek Muralidharan, B.E., Regional Engineering College, India

Chair of Advisory Committee: Dr. David S. Schechter

The fracture aperture and fracture permeability are usually considered to remain the same during the production life of a naturally fractured reservoir, regardless of the degree of depletion; but reservoirs experience different stress state conditions, therefore understanding the fracture behavior becomes more complex. This research analyzes the effect of fracture aperture and fracture permeability on the fluid flow under different overburden pressures. This research investigates the fracture apertures under different stress-state conditions. The equations to quantify the flow through the matrix and the fracture at different overburden pressures are provided. An X-ray CT scanner was used to obtain fracture aperture distributions at various overburden pressures to verify the use of log-normal distribution, which was commonly used for distributing fracture apertures. In addition, reservoir simulations are performed to duplicate the experimental results and to provide a valid model for future stress-sensitive reservoirs.

Our experimental results show that the fracture aperture and fracture permeability have significant pressure-dependent changes in response to applying variable injection rates and overburden pressures. The laboratory results show that the change in overburden pressure significantly affects the reservoir properties. The change in matrix permeability with different injection rates under variable overburden pressures is not significant in contrast with that effect on fracture aperture and fracture permeability. A calibration curve was obtained to determine fracture aperture from the X-ray CT scanner results. The aperture distribution from data obtained from X-ray CT scanner confirms lognormal distribution at various overburden pressures. This experimental research will increase the understanding of fluid flow behavior in fractured reservoirs.

DEDICATION

To my beloved grandparents, parents, uncle, aunt, sister, cousin, and my teachers and mentors in college.

ACKNOWLEDGMENTS

I would like to take this opportunity to express my deepest gratitude and appreciation to the people who have given me their assistance throughout my studies and during the preparation of this thesis. I would especially like to thank my advisor and committee chair, Dr. David S. Schechter, for his continuous encouragement, financial support, and especially for his academic and creative guidance. He has been my source for inspiration throughout my graduate studies.

I would like to thank Dr. Daulat D. Mamora and Dr. Robert R. Berg for serving as committee members, and I do very much acknowledge their friendliness, guidance, and helpful comments while working towards my graduation.

I wish to take the opportunity to thank and acknowledge Dr. Erwinsyah Putra, who is my mentor and guiding light in this research. I know in my heart that I would not be where I am today without the guidance I received from him. I do very much acknowledge his friendship, guidance, and patience throughout my graduate program.

I would like to thank Sandeep Kaul for his help and encouragement for successfully completing my masters thesis. He has given valuable suggestions and guided me throughout my research. I will remember him throughout my life. I would like to thank Dicman Alfred for his friendship and co-operation. I learned a lot from him and will continue our friendship forever.

I also thank my friends Zuher, Bada Deepak, Prasanna, Ashish, Manoj, and Harshal for extending their support and ideas for my research. Although Chotta Deepak joined the naturally fractured group lately, he has helped me a lot which made it possible to complete the final part of the thesis. I would like to thank members of the naturally fractured reservoir group, Mirko, Babs, Emeline, Kim, Orkhan, Hernandez, Jesus, and Jeff for their encouragement and appreciation. I would also thank my roommates Satish, Bhushan, Naveen, Nikhil and Mahavir for making my graduate years very pleasant.

I will always need your valuable advice wherever I work in future. Life is all about motivation, and friends are the source of it. I consider myself to be lucky with lots of helping hands and cheering friends around me all the time. I would like to quote my

favorite quote by Sir Winston Churchill, “This is not the end. It is not even the beginning of the end. But it is, perhaps, the end of the beginning”. Thank you very much.

TABLE OF CONTENTS

CHAPTER Page

CHAPTER Page

LIST OF FIGURES

FIGURE Page

FIGURE Page

FIGURE Page

FIGURE Page

FIGURE Page

LIST OF TABLES

TABLE Page

CHAPTER I

INTRODUCTION – INVESTIGATION OF FRACTURE PARAMETERS AND FLUID FLOW UNDER VARIOUS STRESS CONDITIONS

1.1 Introduction

Naturally fractured reservoirs have millions of barrels of oil left unrecovered due to the poor knowledge of the reservoirs; therefore studies on naturally fractured reservoirs have gained importance over the years. The parameters which govern fractured reservoirs are fracture permeability (and the fracture aperture) and fracture connectivity. The fracture aperture and fracture permeability are usually considered to remain the same during the producing life of the reservoir, regardless of degree of depletion, but reservoirs experience different stress state conditions, therefore understanding the fracture behavior becomes more complex. In this research fracture connectivity has not been discussed.

For many years overburden experiments have been conducted to duplicate the stress-state conditions in the reservoir, in order to investigate the changes in rock properties. The reduction in permeability with overburden pressure has been well known. Fatt and Davis[1] presented the changes in permeability with pressure at range of 0 to 15,000 psig and found that overburden pressure caused a reduction in permeability of the consolidated oil-bearing sandstone samples by as much as 50 percent at 10,000 psig. Gray *et al.*[2] enhanced the previous experiments by applying axial force and combining with overburden pressure (radial forces) to measure the anisotropy permeability changes at a more representative reservoir stress-state condition. They showed that permeability reduction subjected to overburden pressure as a function of the ratio of radial to axial stress and the permeability reduction under nonuniform stress (radial pressure different from axial pressure) is less than that under uniform stress. Although extensive work has established the effect of overburden pressure and stress-state on matrix permeability (Morita *et al.*[3] and Dobrynin[4]) some very interesting details of fractured rock behavior under stress have

---

This thesis follows the style of *SPE Reservoir Evaluation & Engineering*.

not been investigated such as change of fracture aperture, fracture permeability, matrix and fracture flow rates with the change in overburden pressure. This research proposes the analysis of the effect of fracture aperture and fracture permeability on the fluid flow under different overburden pressure. This research also proposes the investigation of fracture apertures under different stress-state conditions (confining stress, hydrostatic stress, and triaxial stress). In addition, the reservoir simulations will be performed to duplicate the experimental results and to provide a valid model for future stress-sensitive reservoirs.

With the introduction of X-ray CT scanner in the petroleum field, the behavior of fracture can be analyzed under different stress conditions. Although we can measure porosity and saturation using the CT number distribution, there is no direct measurement of fracture aperture. Keller[5] provided a calibration curve to measure fracture aperture as small as 35 μm. The best correlation between CT number and the fracture aperture is the integration of missing rock mass. Similar correlation was done by He[6]. But the line integration of the CT numbers in the missing rock region was used by both researchers, which is not a better calibration method. Hence an area integration method is used in this research to obtain a calibration curve to determine fracture aperture from missing rock information.

While a log-normal distribution was suggested for the variable fracture apertures with a single stress level (Bianchi and Snow[7], Bourke *et al.*[8]), the issue of the distribution pattern for different stress levels is still yet unresolved. Usually the fracture apertures were stochastically generated according to the particular distribution and sensitivity studies were made by changing the variance for a particular mean value (Tsang and Tsang[9], Alfred[10]), however, the mean and variance changes when the stress level changes, which might tend to close some of the small apertures. Therefore, distribution pattern cannot be assumed to be the same for all the stress levels unless proved by imaging and measuring the fracture apertures for various levels. This research uses X-ray CT scanner to image the fracture aperture under various overburden pressures and using the calibration curve, measures the fracture aperture at various points along the length of the core, thus generates sufficient data for characterizing the distributions of fracture apertures. The effect of stress level in the aperture distribution will be useful in analyzing

flow and transport phenomenon and tracer studies in the stress-sensitive reservoirs. This experimental research will increase the understanding of fluid flow behavior in fractured reservoirs and hence value to the petroleum industry.

1.2 Motivation

The fractured reservoir is very complex to understand. The fracture aperture changes due to stress acting on the reservoir, but there is no clear understanding of the change in magnitude of the fracture aperture with the change in stress level. Fracture aperture evaluation under stress is important to predict fracture permeability and matrix and fracture flow rates. As the stress level increases, the fracture aperture will be decreasing and matrix flow rate will be increasing. Nuezil and Tracy[11] modeled fracture flow, by representing fractures as a set of parallel openings with different apertures. However they did not take into consideration the matrix flow rate. Similar experiments were done by Tsang and Tsang[12]. None of the research determines the fracture aperture during fluid flow as well as quantifies the contribution of flow from both matrix and fracture. Uniaxial stress level will have less impact on the fracture aperture compared to triaxial and hydrostatic conditions because the axial stresses are not included in the uniaxial condition. Hence analyzing the effect of fracture aperture under different stress conditions becomes important to characterize the fractured reservoir.

Vision is one of the powerful senses of humans and hence X-ray CT scanner is useful to visualize the trend of fracture aperture decrease with increase in the overburden pressure. With the calibration curve between integrated rock mass and known fracture aperture, we can even quantify the fracture aperture using results from X-ray CT scanner.

1.3 Objectives

The objectives of this research are to investigate the changes in matrix and fracture properties and fluid flow under different stress state conditions such as uniaxial, triaxial and hydrostatic conditions. With the change in stress conditions we quantify the changes in fracture aperture, matrix and fracture permeability and matrix and fracture flow rates.

1.4 Methodology

In this research, experiments were performed with both unfractured and fractured core to study the flow behavior in matrix and fractures with increasing overburden pressures. The objective of these types of experiments is to quantify variation of matrix permeability, fracture aperture, fracture permeability, matrix and fracture flow rates with different overburden pressure. The laboratory measurements were analyzed and an effective fracture aperture width was inferred using cubic law. Similar types of experiments with hydrostatic and triaxial stress conditions were performed. A comparative study is performed among uniaxial, triaxial and hydrostatic stress conditions to verify whether which stress-state conditions represent the reservoir conditions closely. Also X-ray CT scanner is used to calculate fracture apertures and verify the lognormal distribution of fracture apertures used in the literature.

CHAPTER II

LITERATURE REVIEW

The reduction of permeability with the overburden pressure has been proved as early as 1952 by Fatt and Davis[1]. Eight cores were used for analysis. High pressure hydraulic bomb was used to place the core. They observed that the specific permeability of sandstone decreases with the increase in the overburden pressure and the permeability decrease more when the overburden pressure ranges from zero to 3000 psig. Wyble[13] did experiments with radial pressure instead of overburden pressure and evaluated the effects of applied radial pressure on conductivity, porosity and permeability of sandstones. Radial pressures up to 5000 psig was applied to rock samples, while the axial stresses were kept at the atmospheric pressure. Even though the radial pressurizing system was used, the permeability decreases when the overburden pressure increases.

McLatchie *et al.*[14] measured the oil permeability under various overburden pressures from 0 to 8000 psig. The reduction in permeability of reservoir rock is related to the compressibility of the rock. The reference permeability was obtained at zero overburden pressure. The oil permeability at each effective overburden pressure as a percentage of the reference permeability was plotted against the overburden pressure. They predicted that permeability reduction in clean sands was relatively small compared to sandstones with large amount of clay.

Dobrynin[4] analyzed the effect of overburden pressure on some properties of sandstones. He observed changes of permeability with pressure at room temperature using nitrogen as the flowing medium. He assumed that the reduction in permeability under pressure is mainly due to the contraction of pore channels. Small changes in permeability due to pressure depend upon an empirical coefficient γ, which in turn depends upon pore size distribution and pore compressibility. They developed empirical relations and presented several sets of curves. From these curves, the estimation of change of property can be determined at net overburden pressure, knowing the pore compressibility and porosity of the rock. Net overburden pressure is defined as (p_e − 0.85 p_i) where p_e is the hydrostatic pressure and p_i is the pore pressure.

While the applied overburden pressure is a case of uniaxial stress condition, some researchers focused their attention on triaxial and hydrostatic conditions, by which the stress conditions in the reservoir can be well represented. Gray *et al.*[2] showed that permeability anisotropy of sandstones is a function of overburden pressure. Both overburden pressure and axial force are applied to the core to give permeability changes close to those occurring in the reservoirs. In the absence of tectonic forces, the nonuniform stress loading will have horizontal stress component (axial force) to be one-third of the vertical stress component (overburden pressure), whereas in the uniform loading, the horizontal stress component is equal to the vertical stress component. A conventional Hassler sleeve was used for the experiment. The apparatus was designed to take 2 in diameter cores up to 3 in long. Pressures up to 5000 psig can be applied. A Carver hydraulic laboratory press was used to apply axial load. They observed that reduction in permeability under nonuniform stress is less than that under uniform stress. They also observed that the maximum reduction in permeability will be experienced under hydrostatic (uniform) loading. They concluded that reduction in permeability will always be less under nonuniform stress in the reservoir, provided the greatest principal stress is overburden pressure. Wilhelmi *et al.*[15] applied triaxial loading, which is the condition, in which two of the three principal stresses are equal. There are difficulties in measuring physical properties of rocks under polyaxial loading; therefore triaxial loading is used, which is commonly used in modern testing. The term deviator stress, which is the difference between the variable axial stress and the constant confining pressure, is used to represent the stress condition. Hydrostatic loading is represented by zero deviator stress at the particular confining pressure. The pore properties are plotted against the deviator stress. A significant observation is that the changes in permeability were of much greater magnitude than changes in porosity under triaxial loading. Even though the hydrostatic loading part of the cycle resulted in greatest change in permeability, significant additional reduction in permeability was observed upon application of deviator stress. This was an expected result because the decrease of porosity and permeability with increase in stress is exponential resulting in large initial decrease during hydrostatic loading. Morita *et al.*[3] performed uniaxial, triaxial and hydrostatic stress experiments on Berea core. When conducting triaxial stress test to failure they observed that at low confining pressures, the

stress/strain behavior is nonlinear at low axial stresses but is linear when the axial stress increases. Close to the failure of the rock, the stress/strain behavior becomes nonlinear again. During hydrostatic loading, the permeability was approximately constant for pore pressure variations at constant effective pressure. Radial and axial permeability decreased upon applying triaxial loading and then increased slightly before failure. Permeability hysteresis was caused by strain hysteresis. Holt[16] performed triaxial compression and extension test on high permeability Triassic sandstone. To compare the results, experiment with hydrostatic stress situations was performed and found that permeability decreased with the increase in hydrostatic stress. For increasing stress difference $|\sigma_a - \sigma_r|$, the permeability decreased further, where σ_a is the axial stress and σ_r is the radial stress. At low values of stress difference, the decrease in permeability was similar to hydrostatic stress condition, when the permeability was plotted with mean stress $\overline{\sigma} = \frac{1}{3}(\sigma_a + 2\sigma_r)$. The permeability increased with the increase in the axial stress close to the yielding point, but decreased again after the failure. The permeability reduction to failure varied from 10% to 95%. The permeability reduction was more when the confining pressure was set at a higher level.

While the stress conditions were taken into account for evaluating physical properties of the sandstones, often the pore pressure is not considered which may be affecting the results. Zoback *et al.*[17] measured the permeability of the Berea sandstone as a function of both confining pressure and pore pressure. Lubricating oil was used for the flow experiment because its density, viscosity and compressibility are known over a wide range of pressures and temperatures. A differential pressure transducer was used to measure pore pressure gradient. They showed that permeability not only depend on effective stress, but also depends on pore pressure. They observed that for a constant confining pressure, permeability increases significantly with increasing pore pressure. They also concluded that pore pressure was four times the effect of confining pressure in the direction normal to bedding planes, and therefore the flow in this direction causes significant reduction in permeability.

Although extensive work has established the effect of overburden pressure and stress-state on matrix permeability, there is also lot of researches being conducted on the

fractured reservoirs. Many reservoirs are fractured to some degree. Earlier, due to the poor knowledge of the fractured reservoirs millions of barrels of oil left unrecovered and hence studies on naturally fractured reservoirs have gained importance over the years. Many researchers (Baker[18], Huitt[19], Snow[20], and Gale[21]) used parallel plate approach for fracture, due to its simplicity. The matrix was considered to be a set of parallel plates separated by a constant aperture. The first comprehensive work on flow through open fractures was done by Lomize[22] in which he used parallel glass plates and demonstrated the validity of cubic law for the laminar flow. He modeled the fluid flow with different fracture shapes and investigated the effects of changing the fracture walls from smooth to rough.

The flow in a fracture is usually characterized by the classical cubic law equation (Witherspoon *et al.*[23]) $Q = 5.11\times10^{6}\left[\frac{w\Delta Pb^{3}}{L\mu}\right]$ where Q is fracture flow rate, w is width of the fracture face, L is the length of the fracture and b is the fracture aperture. This equation is valid only for steady-state isothermal, laminar flow between two parallel plates. This equation assumes that the walls of the fracture are smooth. Jones *et al.*[24] modified the classic cubic law to include the roughness effect, $Q = 5.06\times10^{4} w\left[\frac{\Delta Pb^{3}}{fL\mu}\right]^{0.5}$ where f is the friction factor. If the correct friction factor is used, then this equation can represent both laminar and turbulent flow regimes. For a smooth parallel plate, the friction factor is equal to $96/N_{\mathrm{Re}}$, where N_{Re} is the Reynold's number. If this equation is substituted in the modified cubic law equation, we get classic cubic law equation.

The fractures created artificially in the laboratory should be representative of the real fractures and hence fracture creating technique became important. Hubbert *et al.*[25] provided fracturing technique for laboratory experiments in which the fractures produced should be perpendicular to the axis of the least stress. Usually the underground stresses are assumed to be hydrostatic with the three principal stresses approximately equal, but actually the three principal stresses present in the underground are unequal. While reproducing the fractures in the laboratory, it should represent the stress condition in the

reservoir. Hence for creating a horizontal fracture in the core, the major principal stress should be along the axis and the least principal stress should be perpendicular to the axis of the core.

The comprehensive work on fractured carbonate cores was done by Jones[26] wherein he considered fluid flow through the fracture to be similar to the fluid flow in narrow duct and combined the flow equation with Darcy's law to arrive at an equation for calculating fracture aperture, $w^3 = \frac{12A\times10^{-8}}{D}k$. The fracture aperture is proportional to the cube root of the permeability. In this equation the fluid is assumed to flow only through the fracture. Since fracture porosity is proportional to fracture aperture, the fracture porosity in turn is proportional to the cube root of permeability. These values are ideal since fractures are not smooth and rough factor will have some effect on the fracture aperture and porosity. He normalized the data obtained on the basis of lower overburden pressure he arrived at a useful relationship, $\frac{\phi}{\phi_i} = \left(\frac{k}{k_i}\right)^{1/2}$ where i denotes the value at initial condition. Based on the experiments conducted on carbonate cores, he observed that the porosity and permeability decreased rapidly initially upon the application of overburden pressure when plotting normalized porosity and permeability against overburden pressure. Normalized porosity follows a linear trend with the overburden pressure and it's true for both artificial and natural fractures for limestone and dolomite. When plotting compound permeability against confining pressure, he observed that fracture permeability dominates at lower confining pressure and when the pressure increases, the matrix permeability starts to dominate. Although the fracture starts healing when the overburden pressure increases, the fracture does not heal completely even at 20,000 psig in dense carbonates. He concluded that fracture permeability is greatly affected by overburden pressure.

Flow in fractured media is determined to a large extent by the fracture aperture. Fracture aperture in turn is influenced by a number of factors among which are inclusions and other heterogeneities, stresses and changes in overburden pressure. The common assumption that the fracture aperture remains constant during the entire life of the reservoir is not a valid one. It is well known that the permeability decreases with an

increase in the overburden pressure (Fatt and Davis[1]; Gray *et al.*[2]; Morita *et al.*[3]). Putra *et al.*[27] also determined experimentally that the overburden pressure causes significant changes in fracture permeability and aperture. Hence, it becomes essential to obtain a fracture aperture distribution under different conditions of overburden pressure. Several methods have been used in the past for measurement of fracture aperture. Sharp[28] proposed an empirical law for natural fractures which is based on effective aperture. Witherspoon et al.[23] defines the effective aperture as the difference in the opening between the initial opening and the net flow rate obtained from the calculation of measured flow rate minus that observed under initial closed condition. Using the classic cubic law, the aperture is back calculated using a particular pressure drop and a flow rate. But the common problem associated with these methods is that they are intrusive and hence eliminate the possibility of using the fractured media for fluid flow experiments. Other intrusive techniques are simply inaccurate because of a risk of change in aperture during the course of the experiment. Schrauf and Evans[29] used gas injection into a single fracture and the calculation of fracture aperture based on the volume of gas within the fracture was performed. This technique uses Boyle's law. Because of the small fraction of gas being considered, the calculation of aperture is very difficult and is sensitive. Hence it becomes important to use a non-intrusive, accurate technique to measure fracture aperture. Jones *et al.*[24] developed a technique using high magnification photography to visually measure the aperture between inlet and outlet of the fracture. However the technique assumes that aperture within the center of the fracture is known when the inlet and outlet end of the apertures are measured. Also there should not be much damage of the surfaces under consideration. Averaging technique is needed for this technique. This technique is only suited for large aperture sizes, where the percentage deviation from the average size is very small.

With the advent of Computer Aided Tomography (CAT) X-ray scanning, understanding fluid flow in fractures and measurement of fracture apertures become possible (Johns[30], Keller[31]). With the introduction of X-ray CT scanner in the petroleum field, the behavior of fracture can be analyzed under different stress conditions. CAT scanning provides a good alternative to the existing techniques to measure fracture aperture. Computerized Tomography is a rapid, non-invasive imaging technique that uses

differences in density to image opaque 3D objects (Vinegar[32]). Hounsfield first developed the radiological tool in 1972 which was used extensively for medical purposes (Wellington and Vinegar[33]). CT scanners work on the principle of generation of cross-sectional slices of an object. Computerized Tomography is a process in which a ring of detectors encircles an object and an X-ray source concentric with the detector ring, rotates around the object to obtain one dimensional projections of X-ray attenuation at different angles. Multi-angular projections of an object are obtained by concentrating X-ray beams from a revolving X-ray tube. These projections are then used to reconstruct the image of the object based on the attenuation of X-ray beams (Wellington and Vinegar[33]). Digital image is composed of a finite number of elements referred to as Pixels. The CT scanner has previously been used effectively to perform a wide variety of experiments (Alajmi and Grader[34], Burger *et al.*[35], Stones *et al*.[36], and Hicks *et al.*[37]). Keller[5] made use of non-intrusive imaging to obtain aperture calibration curves for granite and sandstone. Using the curve, fracture apertures as small as 35μm can be obtained. A similar technique was followed by He[6]. Both these techniques use the integrated CT signal to determine fracture aperture. The integration is done by summing up the differences between a minimum rock CT number and the CT numbers pertaining to the fracture.

Fluid flow and solute transport through low-permeability tight rocks predominantly occurs in interconnecting fractures. Earlier studies by Snow[38] and Wilson[39] assumes fracture to be a set of parallel plates separated by a constant aperture and used cubic law to determine fluid flow through the fracture, but fractures have varied apertures along their path, therefore, the fluid flow behave differently from the parallel plate assumption. Upon applying overburden pressure, the rough-walled surfaces can block some portions of the fracture and hence, the fluid flow will not be the same amount as calculated from the parallel plate assumption. Witherspoon *et al.*[23] have conducted laboratory experiments to validate parallel plate theory and they showed that the parallel plate approximation tend to break down at higher normal stress (>10 MPa) across the fracture. Alfred[10] also confirmed that parallel plate assumption is not a valid theory to adequately model the fluid flow experiments when overburden pressure is significant.

Earlier studies on fluid flow through fractures assume that the fracture has constant aperture b_o, represented mathematically by an aperture density distribution $n(b)$,

where $n(b)db$ gives the probability of finding aperture values between b and $(b+db)$. This distribution takes the delta form in case of a parallel plate assumption, with a peak value of b_o, which is given by $\delta(b_o) = \lim_{\varepsilon \to 0} \frac{1}{\varepsilon}$. Analytical solution of a viscous incompressible flow through parallel plate for a steady laminar flow was given by Bear[40]. Once the parallel plate approach is no longer valid, the delta function cannot be assumed for a fracture. Tsang and Witherspoon[41] accounted for the variation of apertures in a rough fracture, which took a different shape rather than delta function. Tsang[42] modeled the variation of fracture apertures by electrical resistors with different resistance values placed on a two-dimensional grid. The results indicate that small apertures play a key role in depressing fluid flow. When the fracture contact area increases, tortuosity and connectivity of fractures become important. Pyrak *et al.*[43] performed laboratory experiments wherein they injected molten wood's metal into single fractures, at different applied stress conditions. The direct evidence of tortuous paths was observed upon opening the cooled metal in the fracture. However, the effect of tortuosity becomes less when the distribution is sharply peaked at large apertures with a long tail in the small apertures (Tsang[42]).

The flow in a single fracture took place in a limited number of channels which was evident from the field experiment carried out in a single fracture by Bourke *et al.*[8]. Upon drilling five holes in the fracture plane and pressurizing each to atmospheric pressure, the results showed that the channels occupied a total area of only about 10% of the fracture plane. Gentier[44] measured fracture surface roughness profiles in a granite fracture. Upon plotting the apertures, the aperture density distribution was approximated by a gamma function. The density distribution is given by $n(b) = \frac{1}{b_o^2} b e^{-b/b_o}$, where b_o represents the distribution peaks, and the mean aperture is $2b_o$. The same distribution was assumed by Tsang and Tsang[12] when considering the channeling of flow through fractured media. They assumed the channel width to be a constant of the same order as the correlation length λ, where correlation length is the spatial length within which the apertures have similar values. The reduction in channel apertures affected the tracer breakthrough curves when normal stress across a fracture is increased.

Although gamma distribution is considered, some authors (Bianchi and Snow[7], Bourke *et al.*[8]) observed the log-normal distribution of fracture apertures from the experiments conducted on cores and well logs. Later Moreno *et al.*[45] followed the same approach when conducting flow and tracer transport model in a single fracture. Using the approach, the flow patterns showed strong resemblance to field observations made by Bourke[46]. Tsang and Tsang[9] used log-normal approach to distribute fracture apertures for determining hydrological methods to obtain relationship between flow and transport measurements of variable apertures. The density function of the log-normal distribution is $n(b)db = \frac{1}{\sqrt{2\pi\sigma^2}} \exp[\frac{-(\log b - \log b_o)^2}{2\sigma^2}] \frac{1}{(\ln 10)b} db$, where σ is the logarithm of the apertures and ($\log b_o$) is the mean. The quantity b_o is the most probable aperture which is smaller than the mean aperture given by $\bar{b} = b_o \exp[(\sigma \ln 10)^2 / 2]$. They determined the mean aperture from flow and transport measurements and distributed the fractures in the log-normal approach. For a log-normal approach, the geometric mean b_o is smaller than the arithmetic mean b and the discrepancy increases with the spread of the aperture distribution σ. They determined aperture variance from tracer breakthrough. Upon injecting mercury in the fractures, an isolated patch in the larger aperture region occurred and spatial correlation length becomes small, the opportunity for the occurrence of the isolated patches is more. Alfred[10] also assumed lognormal distribution for the fracture apertures for considering fracture roughness. The parallel plate model could not adequately represent the fluid flow results of the laboratory experiment and hence using the fracture aperture distribution, he obtained a better match for the experimental results. He also concluded that beyond a particular value of the mean aperture, the effects of roughness and tortuosity is found to be insignificant.

Keller[31] imaged the fracture apertures using X-ray CT scanner and found that most of the apertures are in the range of 300 to 500 microns with the exception of some high aperture value as high as 4500 microns. Based on the study using three different cores, he concluded that the log-normal distribution is adequate in characterizing the fracture aperture. He also compared the geometric mean with the mechanical mean of the apertures and found out that the geometric mean was consistently lower than the

mechanical mean of the apertures. He suggested that for a perfect log-normal distribution, $\frac{a_h}{a_m} = \exp(-\frac{\sigma_h^2}{2})$ where a_h is the geometric mean of the aperture also known as hydraulic aperture and a_m is the mechanical mean of the apertures. The smaller aperture regions confirmed best with the log-normal distribution.

CHAPTER III

EXPERIMENTAL ANALYSIS TO QUANTIFY FRACTURE APERTURES AND FLOW CONTRIBUTIONS FROM MATRIX AND FRACTURE UNDER VARYING CONFINING PRESSURES

3.1 Flow of single fluid between parallel plates

The equation often used to represent flow in fractures wherein *b* is treated as the aperture width, also known as the 'cubic law', is given by:

$$q = \frac{w^3}{12\mu}\frac{(p_0 - p_L)}{L} \quad \text{..... (1)}$$

Darcy law for fluid flow through porous media is given by:

$$q = \frac{kA}{\mu}\frac{(p_0 - p_L)}{L}, \quad \text{..... (2)}$$

Comparing this equation with Darcy's law we have the value of the permeability given by:

$$k = \frac{w^2}{12} \quad \text{..... (3)}$$

3.2 Experimental procedure

For many years efforts have been performed in the laboratory experiments to duplicate the reservoir conditions. In this study, the permeability changes at different overburden conditions are investigated. For simplicity and the difficulty of applying force in the axial direction, these experiments assume the axial direction is in the atmospheric

pressure. Thus, only overburden pressure generated from hydraulic jack was applied to cylindrical face of the core. (Fig. 3.1)

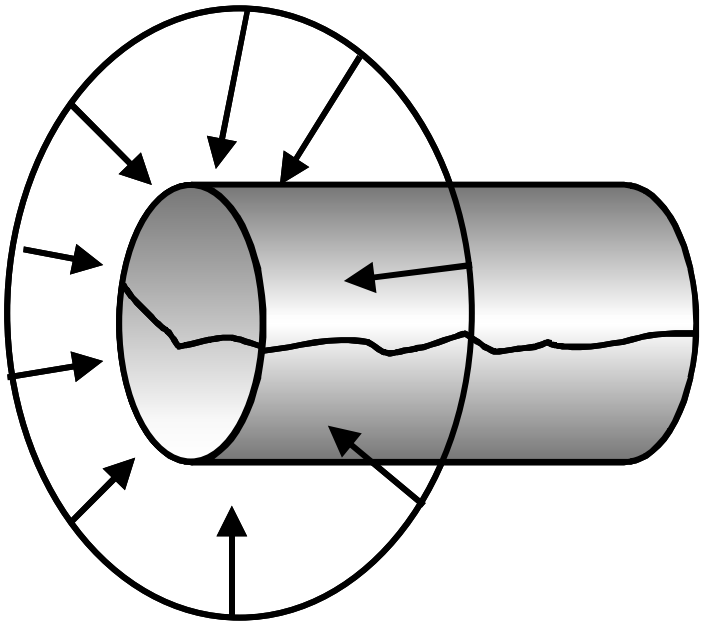

Fig. 3.1 – Illustration of the confining pressure applied on the core.

Synthetic brine was used in the experiments. The brine contains NaCl and $CaCl_2.H_2O$ mixed with distilled water. The clean core was saturated with brine then it was inserted into a Hassler-type core holder using a confining pressure of 500 psia. Then, core flooding was performed with different injection rates. After running set of injection rates at this pressure, we changed to other confining pressures and performed with different injection rates again. Similar procedure was performed using fractured core. Details of procedure for conducting core flooding experiments can be found in Appendix-A. The procedure can be used for single and two phase experiments. The current results are from the single-phase experiments. The experimental set up is shown in Fig. 3.2.

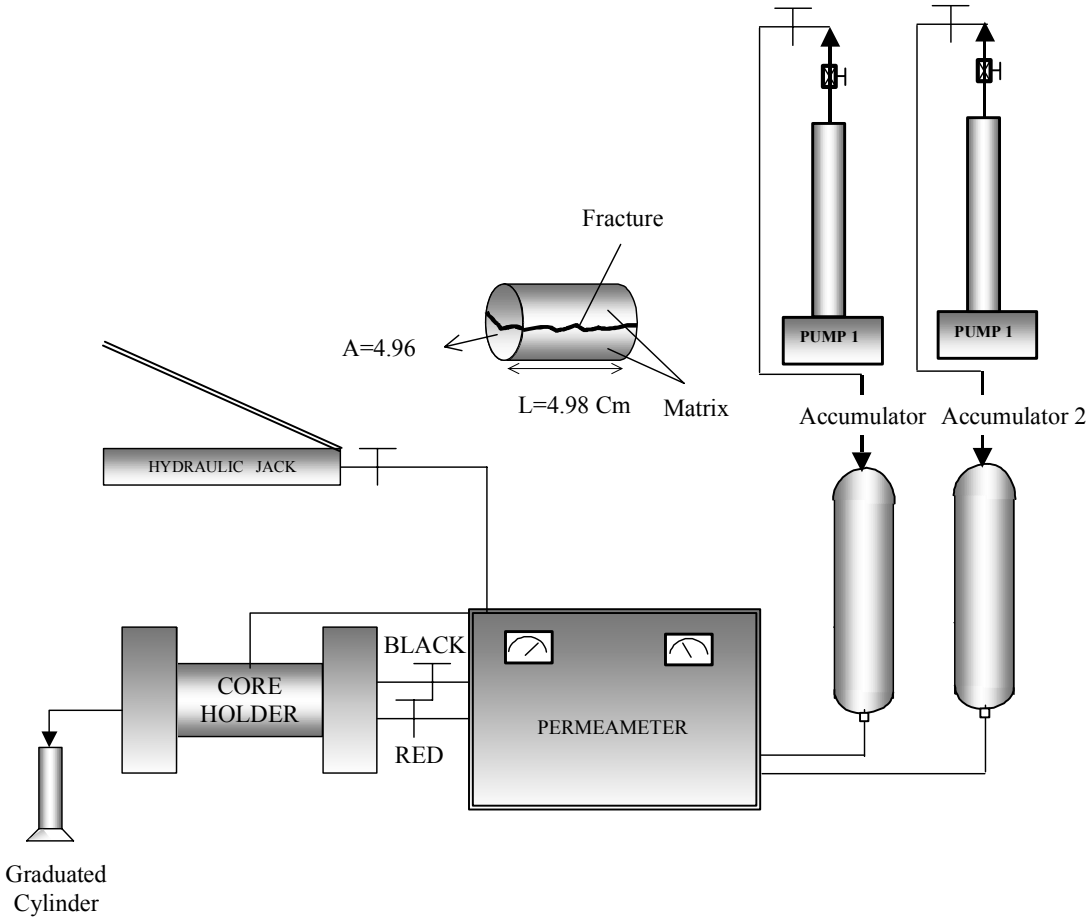

Fig. 3.2 – Schematic diagram of the two-phase core flooding experiment.

A Berea core was used during the core flooding experiments. The core properties are given in Table 3.1. Two sets of injection rates ranging from 5 cm^3/min to 20 cm^3/min were performed at each overburden pressure. Three different overburden pressures were applied started from 500 to 1500 psia for both unfractured and fractured Berea core. The core was cut using a hydraulic cutter to generate fracture horizontally along the axis of the core. During the experiments using a fractured core, the pressure drop across the core is lower and the core permeability increases about 3 times higher compared to those obtained using unfractured core.

Table 3.1 – Berea core properties.

NOTE:	
Berea Core Properties	
Length	4.9784 Cm
Diameter	2.5146 Cm
Viscosity	1.0 Cp
Area	10.9637 Cm^2
Porosity	23.58%

3.2.1 Flow of single fluid through the matrix

When water is injected through the already water saturated matrix, we obtain pressure difference between injecting and producing ends as shown in Fig. 3.3. According to Darcy's law, matrix permeability can be calculated by:

$$k_m = \frac{\mu q_{inj} L}{A \Delta p} \quad \text{.....(4)}$$

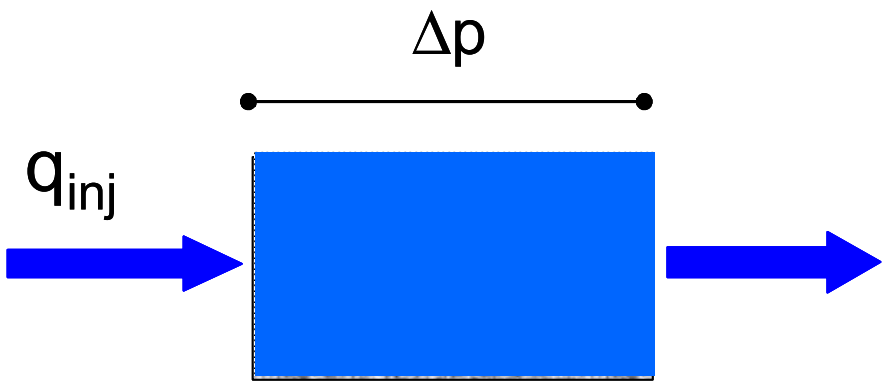

Fig. 3.3 – Water injection through water saturated matrix to measure permeability.

3.2.2 Flow of single fluid through matrix and fracture

When water is injected through matrix as well as fracture in the saturated core, we obtain the average pressure difference between matrix and fracture as shown in Fig. 3.4. According to Darcy's law, average permeability due to flow through matrix and fracture can be calculated by:

$$k_{avg} = \frac{\mu q_{inj} L}{A \Delta p_{avg}} \quad \text{.....(5)}$$

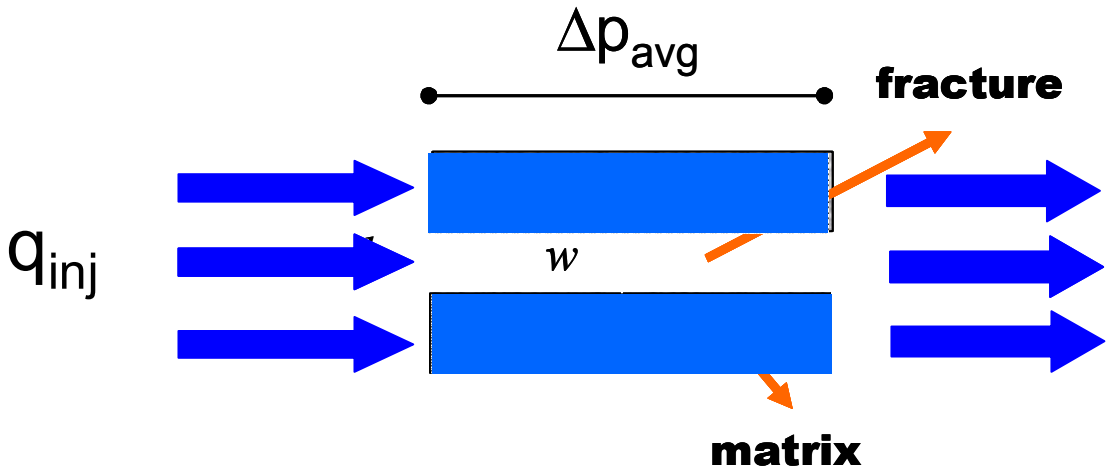

Fig. 3.4 – Water injection through matrix and fracture to measure average permeability.

Table 3.2 – Experimental observations for unfractured core.

Pob **psia**	***Dp*** **psia**	k_m **md**	***Q*** **Cm³/m**
485.7	4.1	299.7	5
506.4	8.1	303.4	10
502.9	12.4	297.2	15
504.4	16.5	297.85	20
501	4.2	292.5	5
504.9	8.5	289	10
501	13	283	15
502	17	289.1	20
1000.4	4.5	273	5
1002.4	9	273	10
1000.5	13.7	269	15
1000.5	18.2	270	20
1000.2	4.8	255.9	5
1003.5	9.7	253.3	10
1002.7	14.5	254.2	15
1004.1	19.2	255.96	20
1500	5.1	240.8	5
1500	10.4	236.3	10
1500.7	16.4	224.7	15
1503.1	22.1	222.4	20
1500.3	5.5	223.4	5
1501	11.2	219.4	10
1501.3	17.3	213	15
1502.3	22.7	216.5	20

Table 3.3 – Experimental observations for fractured core.

Pob **psia**	***Dp*** **psia**	k_{av} **md**	***Q*** **Cm^3/min**
501.3	1.4	877.5	5
500.2	2.8	877.6	10
503.3	4.1	898.9	15
503.3	5.4	910	20
494.8	1	1228.7	5
509.4	2.6	945.1	10
508.8	4.2	877.6	15
509.6	5.8	847.3	20
970.5	2.2	558.4	5
1000.5	4.8	511.9	10
1001	7.6	485	15
1016.7	11.3	434.9	20
1000.8	2.3	534	5
1002.2	5.8	423.6	10
1009.7	9.1	405	15
1002.7	13.9	353.6	20
1500.3	4.2	292.5	5
1504.6	9.3	268.2	10
1507.9	15.1	244.1	15
1504.8	21.4	229.6	20
1500.7	5	245.7	5
1506	10.9	225.4	10
1509.6	17.4	211.8	15
1509.6	22.5	218.4	20

Tables 3.2 and 3.3 show the data obtained from experiments with unfractured and fractured core and the calculated permeability values. Fig. 3.5 shows that the effect of varying overburden pressures on unfractured core is not significant in contrast with that effect on fractured core. The average permeability of fractured core significantly reduces and tends toward the permeability of unfractured core at 1500 psia. The trend lines are used to illustrate this phenomenon and not for any calculation purposes. The result suggests that the effect of stresses may be most pronounced in fractured reservoirs where large pressure changes can cause significant changes in fracture aperture and the related changes in conductivity within a reservoir.

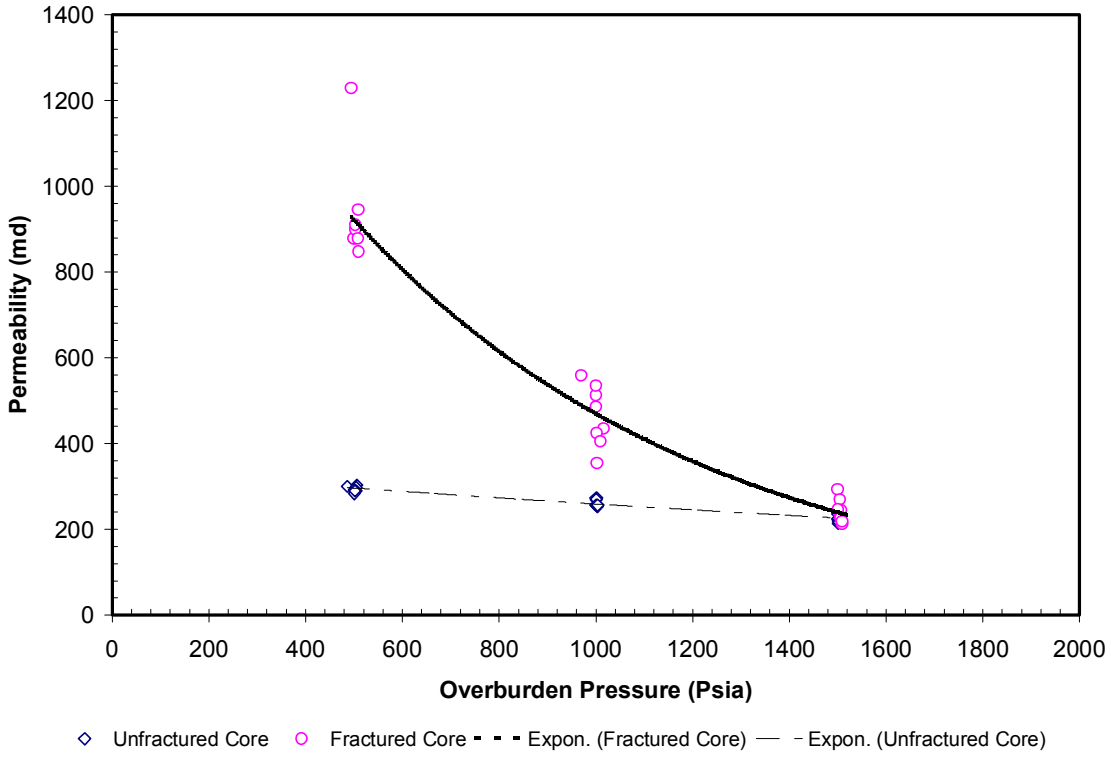

Fig. 3.5 – Comparison permeability reduction between unfractured and fractured cores due to increasing overburden pressure.

3.3 Data analysis

In order to properly quantify the effect of fracture permeability on the fluid flow, it is important to describe the equations describing the changes of this parameter under different overburden pressure. The equations governing the fluid flow through fractures have been widely published in the reservoir engineering literature and are not discussed here. However, the pertinent equations used for our analysis are presented in this section. Fig. 3.6 shows the cross-sectional view of matrix and fracture. The matrix is considered to be set of parallel plates separated by constant aperture, w. From experimental analysis, we obtained matrix and average permeabilities as discussed in section 3.2.

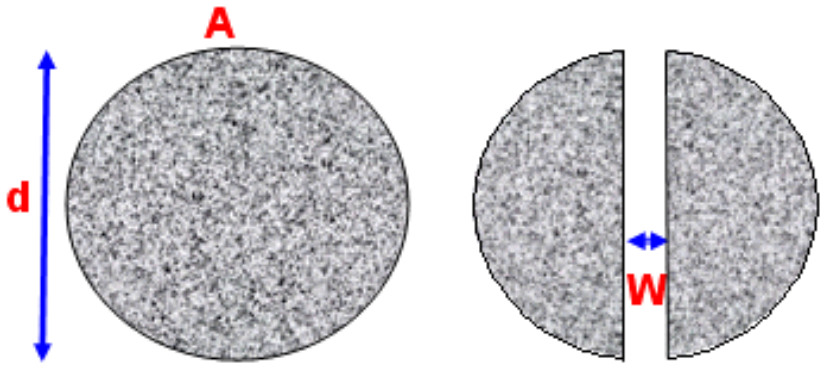

Fig. 3.6 – Cross-sectional view of matrix and fracture.

The fracture permeability, k_f, obtained by combining the viscous force and Darcy equation for flow through fractures as given below,

$$k_f = 8.45\times10^9\, w^2, \quad \text{.....} \quad (6)$$

where w is fracture width in centimeters.

Fracture width is a function of fracture permeability and both the parameters are unknown. To obtain those parameters, another equation is needed. We obtained the average permeability of fracture and matrix, k_{avg}, from core flooding experiments using a fractured core and matrix permeability, k_m, using unfractured core. Using the area weightage of permeabilities, we obtained an equation as given below:

$$k_{avg} \times A = k_m \times A_m + k_f \times A_f \quad \text{..... (7)}$$

In this equation A represents total area of the core, A_f represents area of the fracture which is eual to wl, and A_m represents area of the matrix which is equal to $A - wl$. By rearranging the above equation we obtain an expression for calculating fracture permeability, k_f as given below:

$$k_f = \frac{k_{avg} A - k_m (A - wl)}{wl} \quad \text{..... (8)}$$

Now, we have two equations and two unknowns. So, combining Eqs.6 and 8, we can solve the fracture permeability and fracture width.

$$8.45 \times 10^9 w^3 l - k_{avg} A + k_m (A - wl) = 0 \quad \text{..... (9)}$$

Eqn. 9 is solved by iteration process to obtain fracture aperture w, which is then inserted to Eqn.1 to solve k_f.

It is also important to determine the contribution of flow rate from the matrix (q_m) and fracture (q_f). We determine the contribution from each zone by applying Darcy's equations. The equation for flow rate in the matrix is

$$q_m = \frac{k_m A \Delta p}{\mu L} \quad \text{..... (10)}$$

The flow through a smooth conduit can be expressed by involving the fracture width (w) and the pressure gradient (Δp_{avg}) as

$$q_f = \left(\frac{1}{9.86 \times 10^{-9}} \right) \frac{w^3 l \Delta p_{avg}}{12 \mu L} \quad \text{..... (11)}$$

3.4 Discussion

During the experiments with the fractured core, the pressure drop across the core is lower and the core permeability increases about three times, compared to those obtained using the unfractured core. The effect of varying overburden pressures on the unfractured core is not significant, in contrast with the effect on the fractured core, as shown in Fig. 3.4. At 1,500 psia, the average permeability of the fractured core significantly reduces and even reaches the permeability of the unfractured core. An increase in the pressure drop causes large changes in the average permeability of the fractured core, as depicted in Fig. 3.7. We can clearly see that permeability of fractured core is high initially and when the pressure drop increases, the permeability of fractured core almost reduces to matrix permeability value.

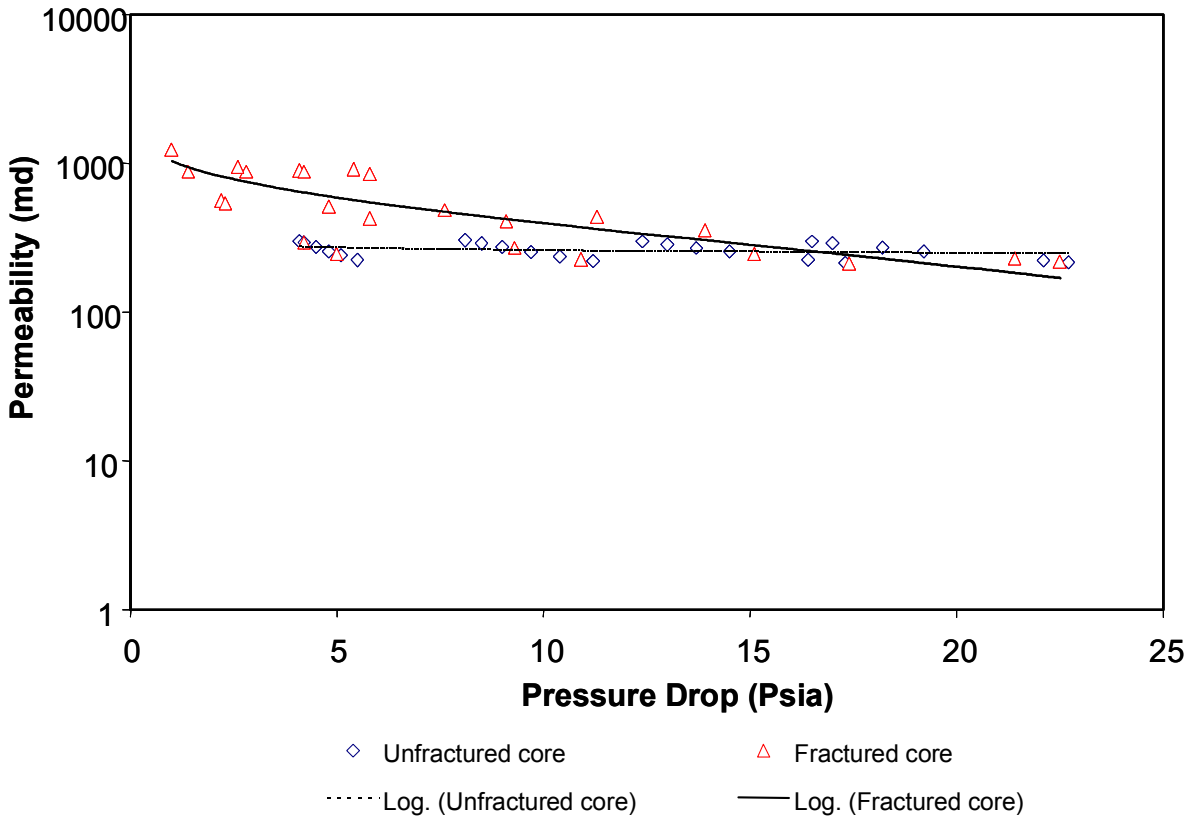

Fig. 3.7 – Relationship between pressure drop and permeability.

The fracture aperture and the fracture permeability are usually considered to remain the same during the producing life of the reservoir, regardless of the degree of depletion. Our experimental results show that the fracture aperture and fracture permeability have significant pressure-dependent changes, in response to applying variable injection rates and overburden pressures.

Fig. 3.8 shows the effect of several injection rates on matrix permeability. Initially an overburden pressure of 500 psi was applied; the matrix permeability was close to 300 md, for all injection rates. When the overburden pressure was increased, the decrease in permeability was observed. The results agreed with that observed by Fatt and Davis[1]. The matrix permeability was close to 200 md at an overburden pressure of 1500 psi. During the constant injection rates of 5 to 20 cm^3/min, the average matrix permeability decreases by about 24% at the overburden pressure of 1,500 psia, from its original value at 500 psia.

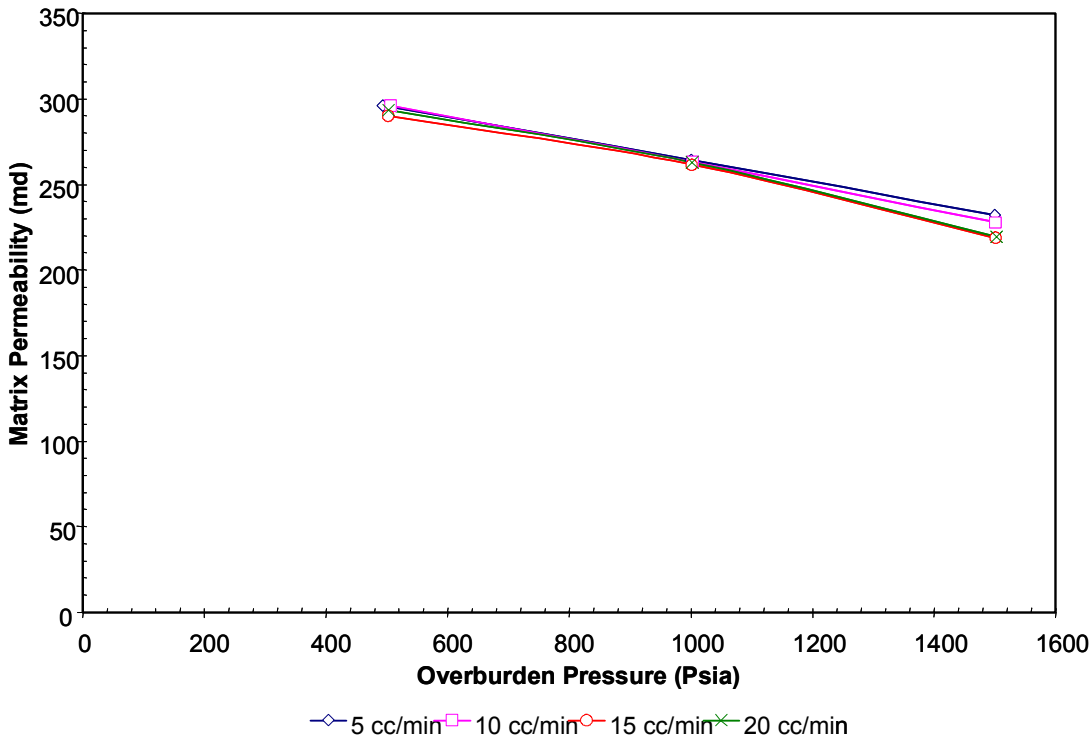

Fig. 3.8 – Effect of injection rates on matrix permeability at variable overburden pressures.

Fig. 3.9 shows the effect of several injection rates on fracture aperture under variable overburden pressures. The effect of several injection rates on the matrix permeability is not significant, in contrast with the effect on the fracture aperture. The average fracture aperture decreases about 71% from its original value. We can see the effect of hysteresis on fracture aperture for various injection rates. The term hysteresis means retardation of recovery from elastic deformation after stress is removed. Initially an injection rate of 5 cm^3/min was used and the overburden pressure was increased from 500 psi to 1500 psi. For the next injection rate of 10 cm^3/min, the core is then brought back to original pressure of 500 psi, during which the core experiences hysteresis. This is clear from the reduction of fracture aperture for an increase of injection rate from 5 cm^3/min to 10 cm^3/min at 500 psi. This is due to the fact that fracture surface deformation occurred when the pressure was increased and when the pressure is reduced the fracture surface roughness changes than it was before. However the effect of hysteresis is less for subsequent injection rates as the fracture roughness was not much susceptible after the initial change.

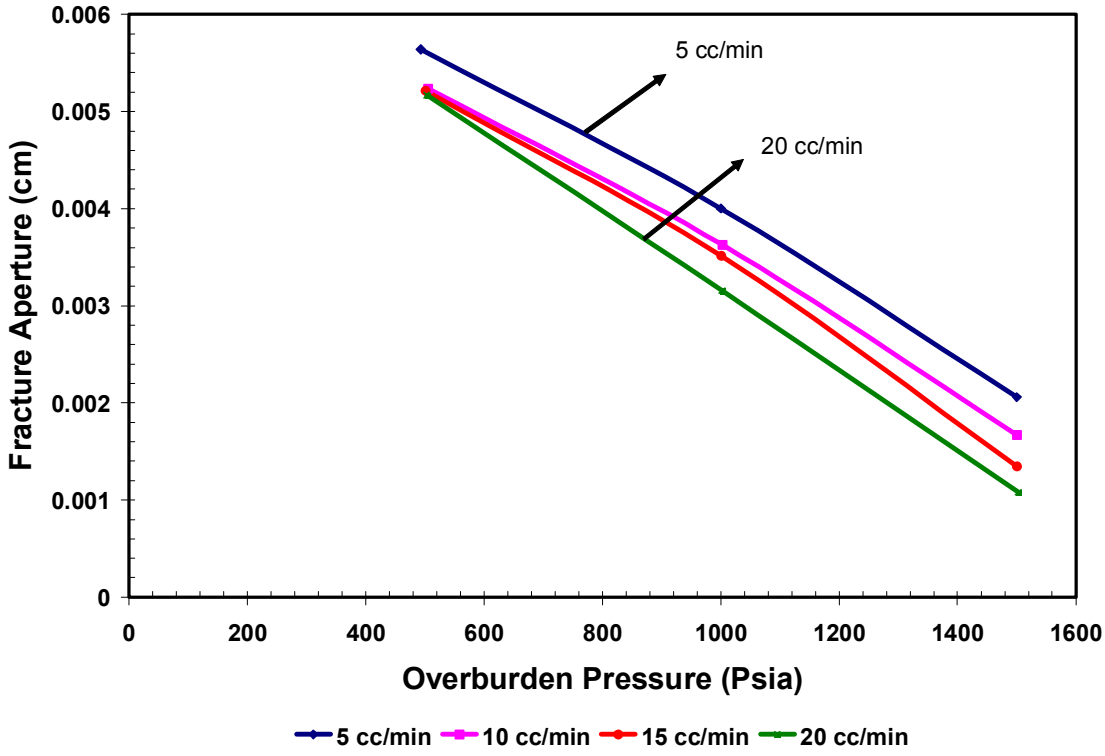

Fig. 3.9 – Effect of injection rates on fracture aperture at variable overburden pressures.

Fig. 3.10 shows the effect of several injection rates on fracture permeability, under variable overburden pressures. The fracture permeability is very high as compared to matrix permeability. The effect of several injections on the matrix permeability is not significant, in contrast with the effect on the fracture permeability. During the constant injection rates of 5 to 20 cm^3/min, the average fracture permeability decreases by about 91% at the overburden pressure of 1,500 psia, from its original value at 500 psia. The trend of fracture permeability with overburden pressure is same for all the injection rates. Since fracture permeability is proportional to square of fracture aperture, it follows similar trend to that of fracture aperture decrease due to increase in overburden pressure. We can also observe the hysteresis effect on the plot of fracture permeability.

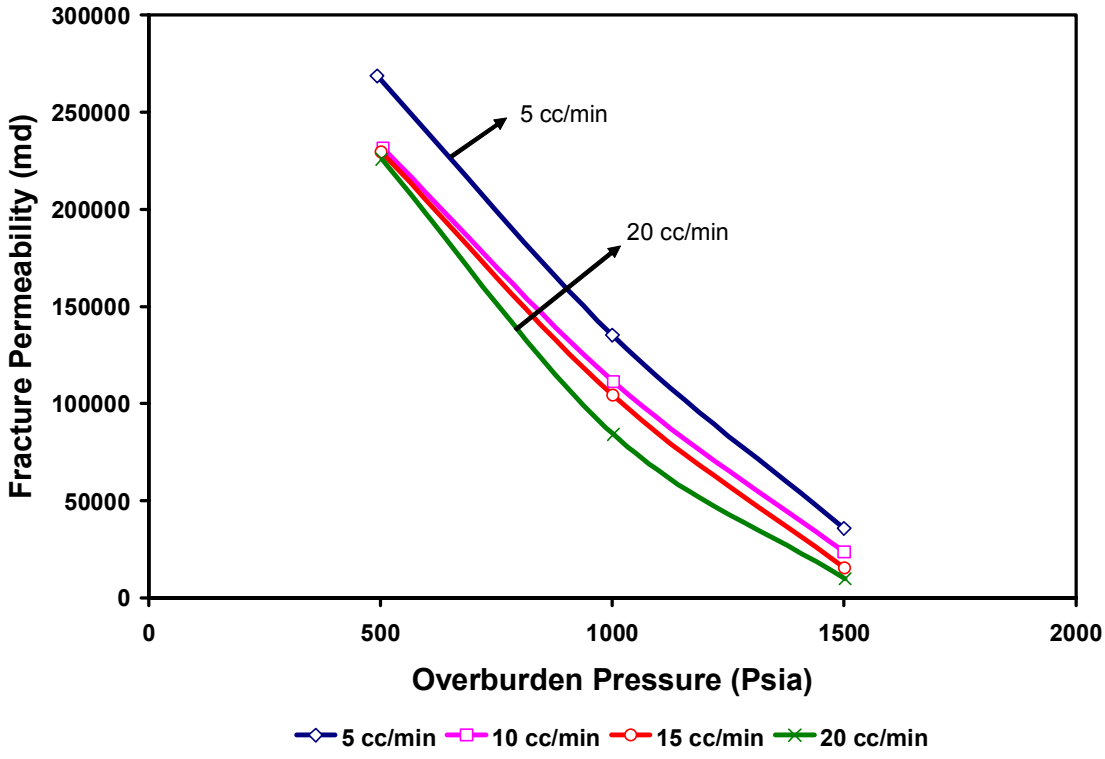

Fig. 3.10 – Effect of injection rates on fracture permeability at variable overburden pressure.

The results also indicate that the influence of high stress on axial direction by introducing high injection rates would give high permeability reduction as also previous reported by Gray *et al.*[2]. The fracture width is a function of fracture permeability and hence the fracture permeability has a similar trend as fracture width, under different overburden pressures. The fracture permeability ranges from about 200 to 700 darcy at 500 psia and reduces to about 9 to 36 darcy at 1,500 psia.

A very different behavior of the curve is observed for the first injection rate than the other injection rates. After the first injection rate at 500 psia, the fracture apertures at injection rates of 10, 15, and 20 cm^3/min have similar values. Meanwhile, after increasing the overburden pressure, the effect of injection rates on the fracture aperture is more obvious. As overburden pressure increases, the higher injection rates have more reduction in the fracture aperture, which is different from the common thought. The reason behind this phenomenon is that the core is surrounded by constant high confining pressure, which does not allow the core to expand as shown in Fig. 3.11.

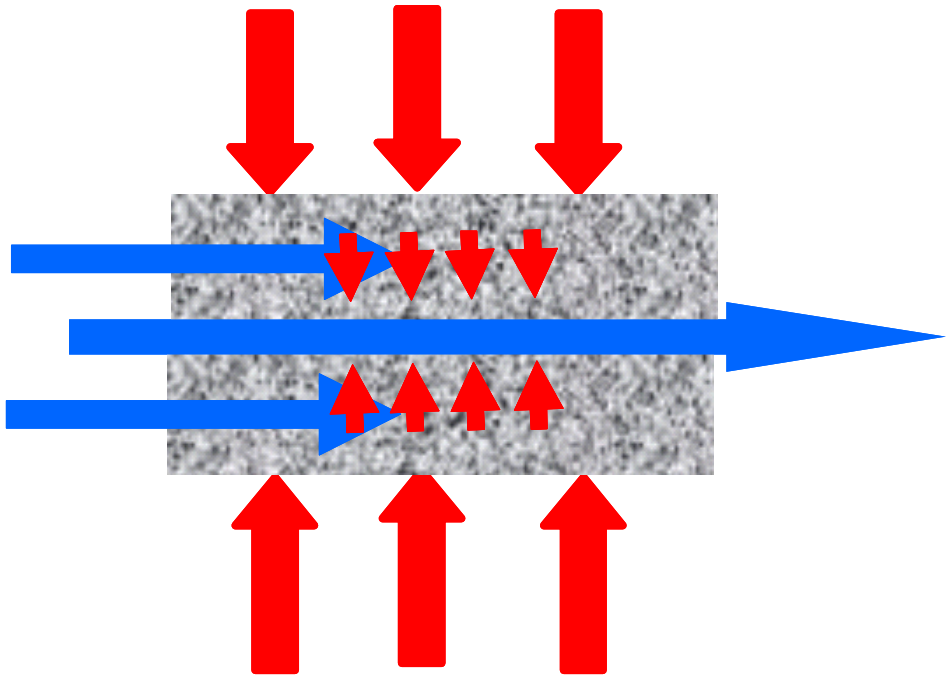

Fig. 3.11 – Picture showing the decrease of fracture aperture upon increasing the injection rate.

Fig. 3.12 shows the trend of fracture flow rate with the change in overburden pressure. The fracture flow rate decreases with the increase in overburden pressure. At 500 psi overburden pressure and at 5 cm^3/min injection rate, the fracture flow rate is around 4 cm^3/min. This means around 80% of the flow is through the fractures due to high permeability. The amount of flow, at different injection rates through the fracture drops dramatically and they almost flow at the same rate at confining pressure of 1,500 psi (about 1 cm^3/min), as shown in Fig. 3.12. This means that the water mostly flows through the matrix, diverting from the fracture path. At higher injection rates, the pressure drop becomes higher through the matrix and increases the tendency to squeeze the fracture aperture. Hence, the fracture aperture becomes smaller at higher injection rates. Even though the fracture permeability is still very high (10 to 40 darcy), the volumetric rate of fracture becomes limited. Most of the water flows through the matrix rock of less permeability (200 md) and the volumetric rate is higher. Hence this causes the flow to pass through the matrix resulting in lower fracture flow rate at higher overburden pressures.

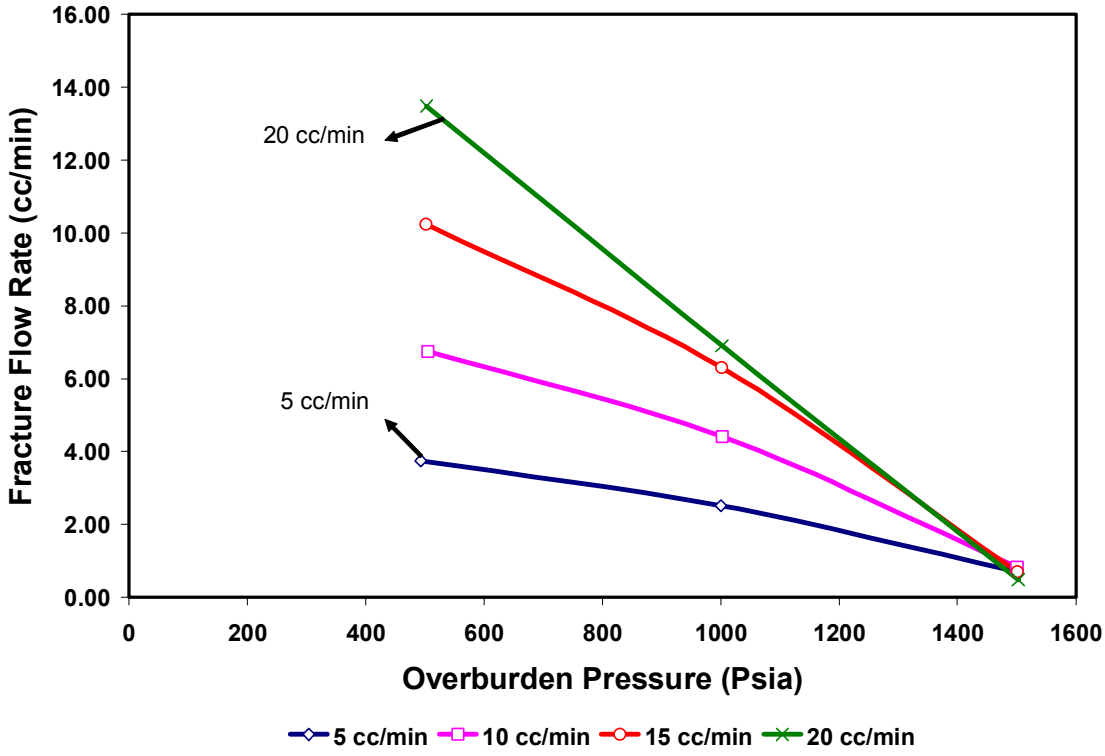

Fig. 3.12 – Effect of overburden pressures on fracture flow rates.

The reduction of the fracture permeability clearly has significant effects on reservoir productivity. We determine the reduction of fluid flow through the fracture caused by the reduction in the fracture permeability. It is also important to quantify the flow through the matrix and the fracture, at different overburden pressures. By applying Eqs. 10 and 11, we quantified the contribution of fluid flow from the matrix and the fracture as shown in Figs. 3.12 and 3.13, at variable overburden pressures.

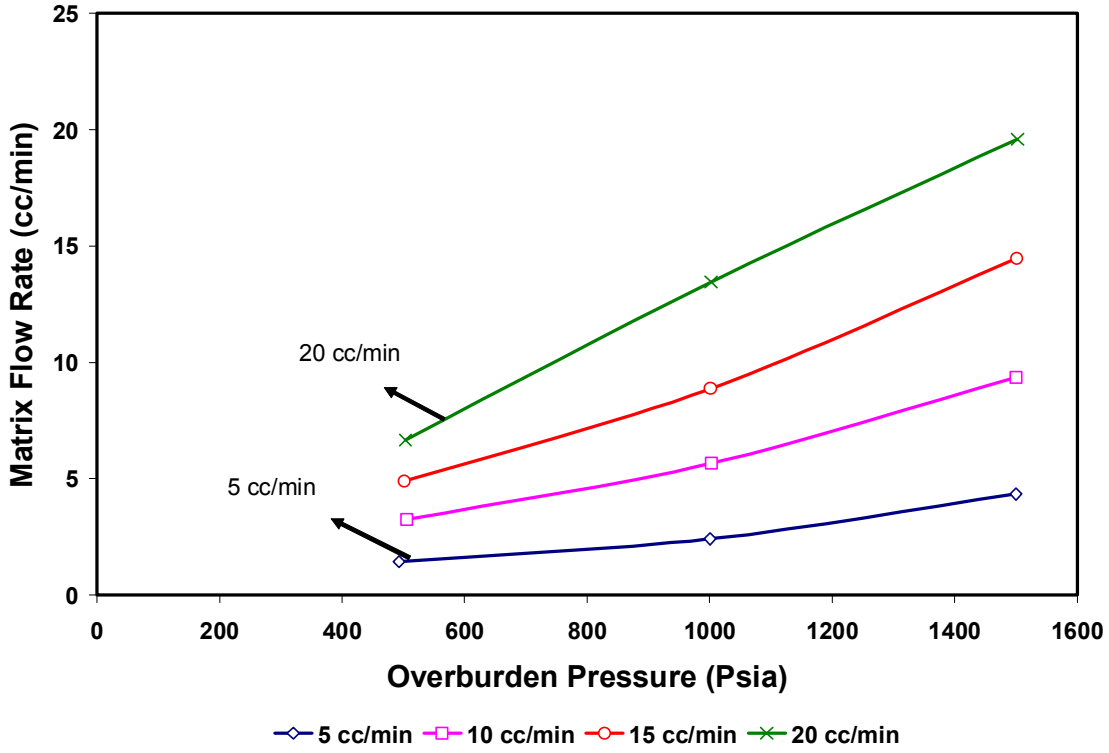

Fig. 3.13 – Effect of overburden pressures on matrix flow rates.

At 500 psia, the flow is preferably in high permeability zone. At this time, the percentage range of fluid flow through the fracture, at injection range of 5 to 20 cm^3/min, is 72% to 68%. Meanwhile, after increasing the overburden pressure, the fluid flow through the fracture decreases. At 1,500 psi, the percentage range of fluid flow through the fracture at different injection rates is only 14% to 2%. At this time, most of the injected water diverts through the matrix because of the significant reduction of the permeability in the fracture.

3.5 Artificially fractured core simulation

A numerical model utilizing commercial simulator (CMG™) was used to study the fluid flow through fracture at different overburden pressures. The laboratory process in which the water was injected through the fracture was duplicated in this modeling effort. The rectangular grid block was applied to overcome the difficulty of modeling a cylindrical core shape [47].

A 31x31 grid blocks were used in the x and z directions with 1 grid block in the y direction. The fracture layer is located only in the 16th layer and the rest are matrix layers. The permeability in fracture layer was calculated based on two parallel plates without fracture roughness. All the layers were injected with constant water injection of 5 cm^3/min. At the opposite end, two production points were located in the matrix and fracture layers to quantify the amount of water produced at those two points.

In the experimental process, the core is saturated with the water. Once water injection was started with constant rate, water was produced simultaneously. Then the water that was produced from both matrix and fracture layers at the end point was recorded. In the simulation, however, the initial water saturation condition is assumed zero to visualize the movement of water through single fracture. The water saturation change in the matrix and fracture during transient state can be observed as illustrated in Fig. 3.14. We can clearly see that water advances faster through fracture than through matrix due to high fracture permeability compared to matrix permeability. The time to breakthrough was observed to be 0.62 min. This simulation run was performed for an overburden pressure of 500 psi.

A few minutes after the injection was started, the flow rate was still in the transient condition and then reached a steady state condition at later time as shown in Fig. 3.15. At steady state condition, the amount of water produced from matrix and fracture was recorded. Similar simulation runs were performed for different overburden pressures.

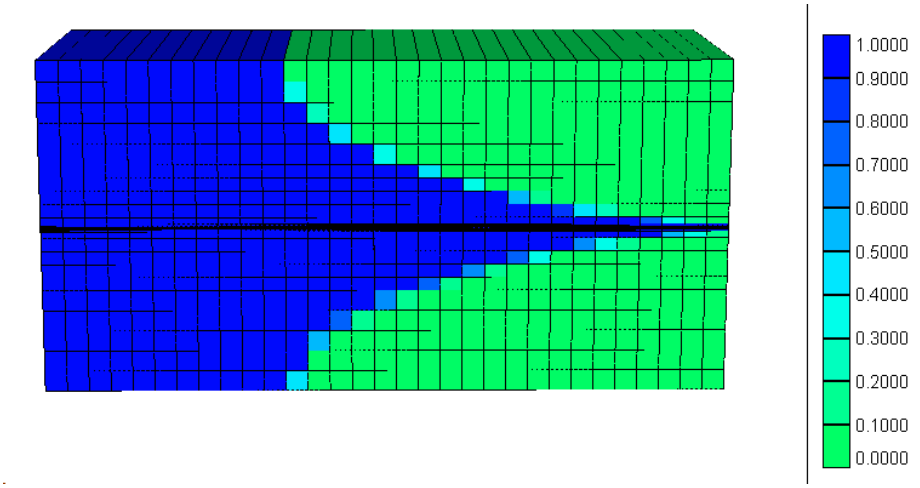

Fig. 3.14 – Water saturation change in matrix and fracture at transient flow condition.

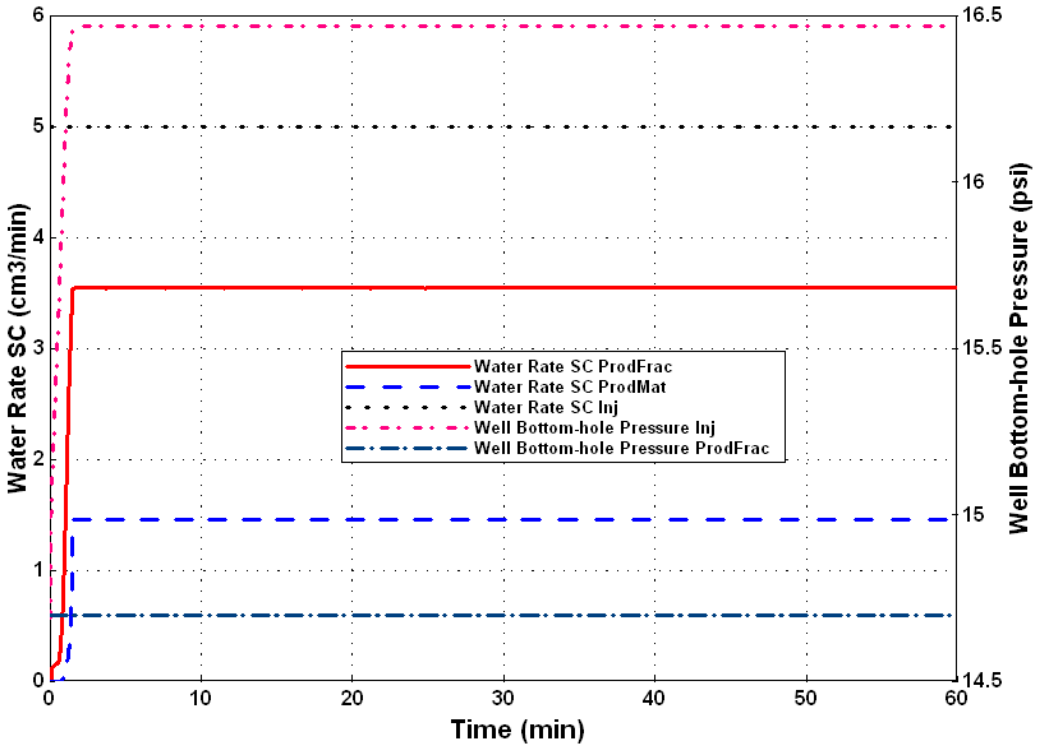

Fig. 3.15 – The simulation results of flow rates and pressure drop injected at 5 cc/min and overburden pressure of 500 psi.

The results for the 5 cc/min injection case was compared with the experimental results as shown in Figs. 3.15 and 3.16. The dotted lines indicate the experimental results and solid lines indicate simulation results. As we can see from Fig. 3.16, the simulated fracture flow rate is slightly higher than the experimental flow rate and the simulated matrix flow rate is slightly lower than the experimental matrix flow rate. Also the simulated pressure difference is higher than what is observed experimentally as shown in Fig. 3.17.

The quality of the match for both flow rate and pressure drop are not quite good due to using a single fracture model, which assumed smooth fracture surface between two parallel plates. Both matrix and fracture permeabilities are calculated from the parallel plate assumption which is not an accurate method of characterizing fractured reservoir. Hence when simulation is performed using the calculated permeabilities, the pressure difference could not be adequately matched due to high fracture permeability obtained from parallel plate assumption. This accounts for more water breakthrough through the fracture than in the matrix. Since the fracture area is small compared to matrix flow, the pressure drop obtained from simulation is more compared to experimental value. If the fracture apertures are distributed then the smaller aperture region will cause barrier for fluid flow through fracture, which will result in more matrix flow than fracture flow. Since the area of matrix is much higher compared to fracture and matrix permeability is more for Berea core, the pressure drop will be low (refer Chapter V). The roughness factor might be incorporated in the simulation model which will reduce fracture flow rate. The experimental results through fractured core were matched by Alfred[10], using stochastically distributed fracture apertures and introducing friction factor for the fractured flow.

Even though the quality of the match for both flow rate and pressure drop are not quite good due to using a single fracture model, but the simulation results follow the trend of the laboratory results. If the confining pressures increase further, then the results of simulation might not match with experimental results because the parallel plate approach deviates from the normal results (Witherspoon *et al.*[23]). The simulation work aid in understanding the drawback of parallel plate approach and also highlights the importance of introducing roughness in simulation model.

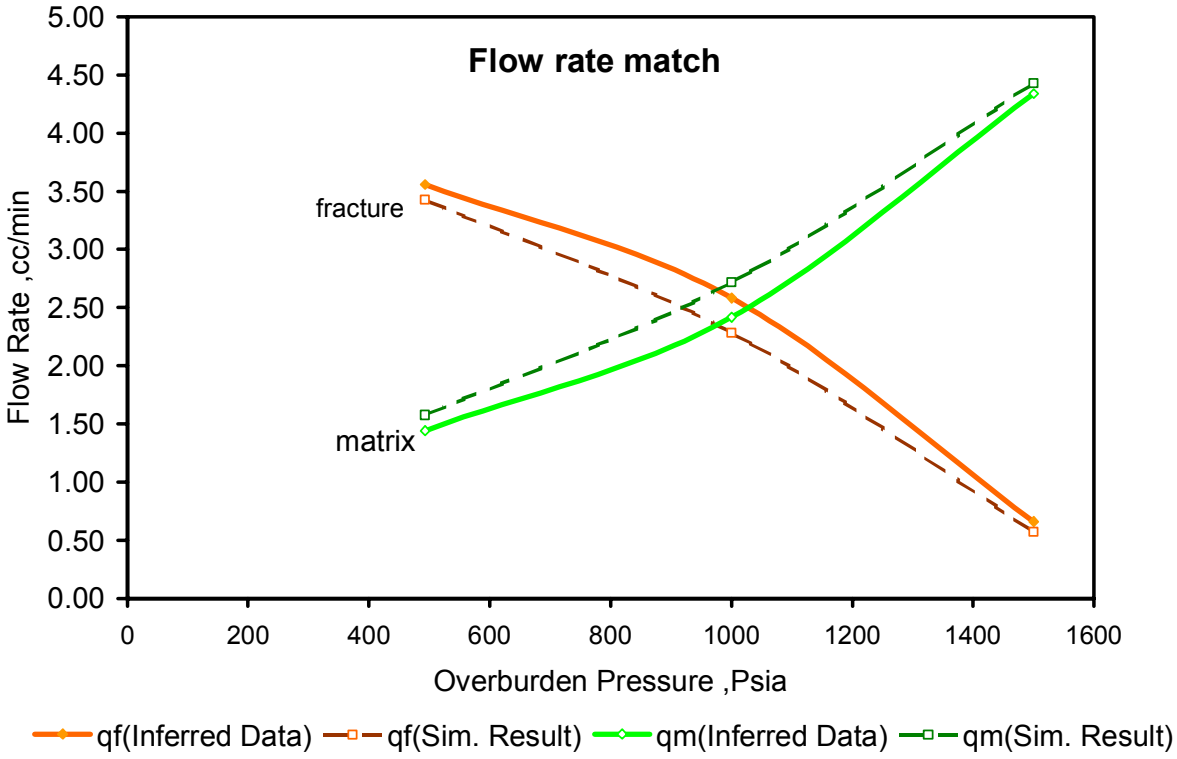

Fig. 3.16 – The average flow rate comparison between laboratory and simulation results at 5 cc/min and each different overburden pressure.

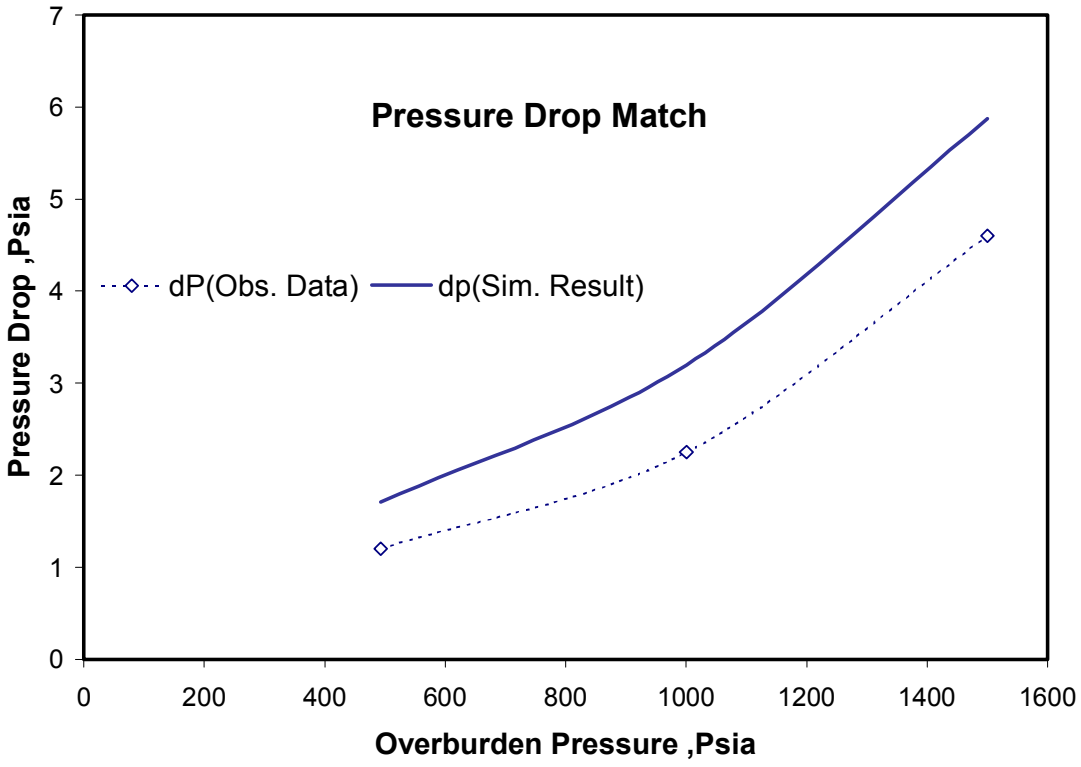

Fig. 3.17 – The average pressure drop comparison between laboratory and simulation results at 5 cc/min and each different overburden pressure.

CHAPTER IV

INVESTIGATING THE CHANGES IN MATRIX AND FRACTURE PROPERTIES AND FLUID FLOW UNDER DIFFERENT STRESS-STATE CONDITIONS

4.1 Hydrostatic stress experiments

Hydrostatic stress state is the condition in which both axial and overburden pressures are equal. In this study, the permeability changes at different hydrostatic pressure conditions are investigated. Thus, overburden and axial pressures generated from hydraulic jack were applied to cylindrical core (Fig. 4.1).

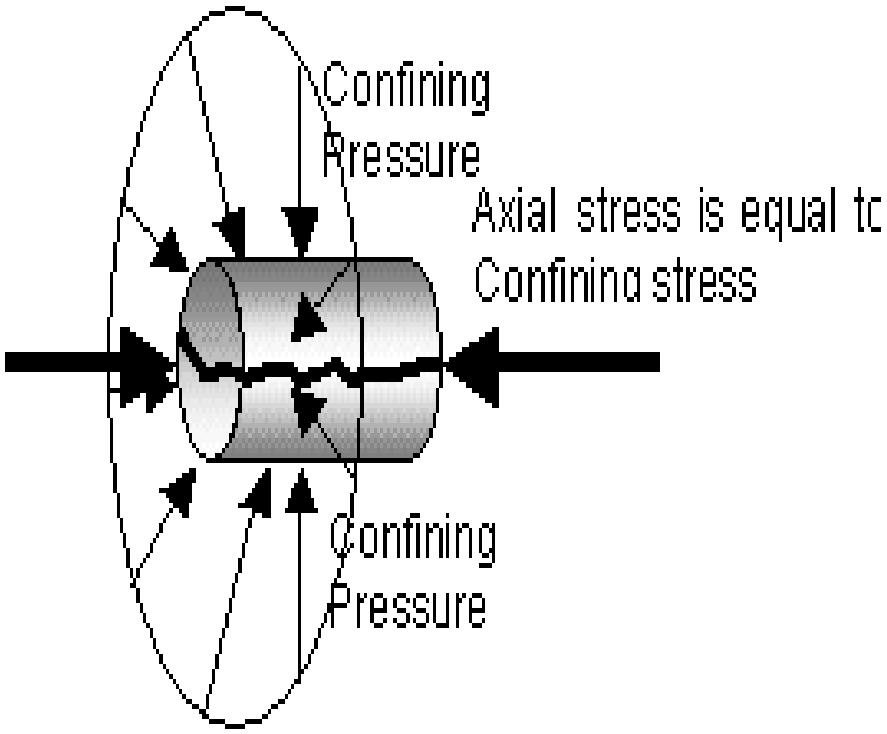

Fig 4.1 – Hydrostatic stress condition

4.1.1 Experimental description

The core sample is subjected to both overburden pressure and axial stress. The axial stress is equal to the overburden pressure for the hydrostatic experiment. Permeability is evaluated at various confining pressures and at various injection rates. The cores are then fractured subsequently and the effective permeability due to fractures is evaluated at various confining pressures and injection rates. The parameters are plotted against overburden pressure to study the effect of confining stress.

4.1.2 Berea cores

Berea sandstone was used in this study. Berea sandstone was selected because it is widely used as a standard porous rock for the experimental work in the petroleum industry. The cylindrical core sample was cut from 0.5 ft^3 blocks of Berea sandstone. The diameter of the sample is 3.6 cm. The length of the core is 4.88 cm. The dimensions are the average values of 3 to 4 measurements using a vernier caliper. The bulk volume of the sample is 49.68 cm^3.

4.1.3 Brine composition

Synthetic brine was used in the experiments. It was prepared by dissolving Nacl and $CaCl_2.2H_2O$ in distilled water. The brine compositions are shown in Table 4.1.

Table 4.1- Synthetic brine composition.

Salts Content	Concentrations (mg/L)
Nacl	122,699
$CaCl_2.2H_2O$	7,497
Total Dissolved Solids	130,196

4.1.4 Pore volume and porosity

The porosity is calculated by the saturation method. The saturation method of determining porosity consists of saturating a clean dry sample with a fluid of known density and determining the pore volume from the gain in the weight of the sample. For this experiment, the core is saturated with brine. The pore volume is calculated from the following expression

$$PV = \frac{W_{wet} - W_{dry}}{\rho_b} \quad \text{..... (12)}$$

where W_{dry} is the weight of the dry core, W_{wet} is the weight of the core after saturating with brine and ρ_b is the density of the brine. The pore volume was calculated to be 11.71 cm^3. The calculated porosity is 23.58%.

4.1.5 Experimental procedures

4.1.5.1 Core saturation

Dry core samples were weighed on a balance. The core sample was then saturated with deaerated brine using a vacuum pump for at least 12 hours. After saturating the core samples with brine, a period of 3 days was allowed for the brine to achieve ionic equilibrium with the rock.

4.1.5.2 Core flooding

The saturated core is inserted in the Hassler-Type core holder. Overburden pressure is applied in the radial direction and the axial tension is applied along the axis of the Berea core, perpendicular to the overburden pressure. An initial overburden pressure of 500 psi is applied. This is followed by core flooding with the brine solution at flow rates of 5, 10, 15 and 20cm^3/min. The pressure drop across the core is recorded in the transducer. The experiments are repeated for overburden pressures of 1000 psi and 1500 psi and the corresponding pressure drops are recorded. Subsequently, the core is fractured along the axis and the experiment is repeated as before, for the fractured core. The experiment can be performed for the two-phase flows as shown in the figure (Fig. 4.2). However, the focus is on the single-phase flow.

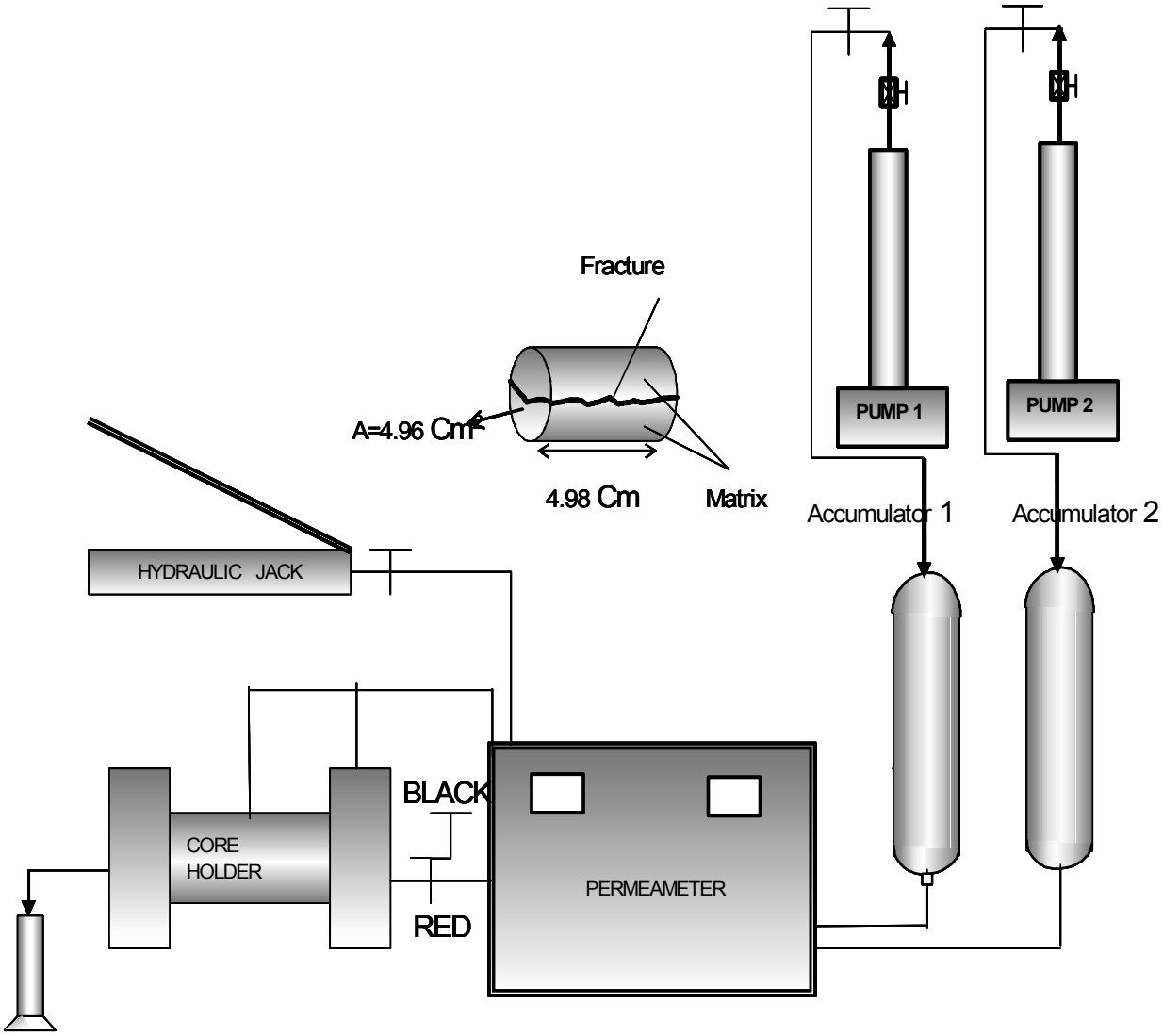

Fig. 4.2 - Hydrostatic loading apparatus

4.1.6 Discussion of experimental results

4.1.6.1 Effect of stress on permeability

Permeability of the rock decreases with the increase in the applied stress. Fig. 4.3 shows the effect of overburden pressure on permeability of both the unfractured and the fractured core. The permeability is reduced in both the cases with the increase in the stress level; however the decrease in permeability of the unfractured core is very less compared to the fractured core. The equations for calculating permeability are given in Chapter III.

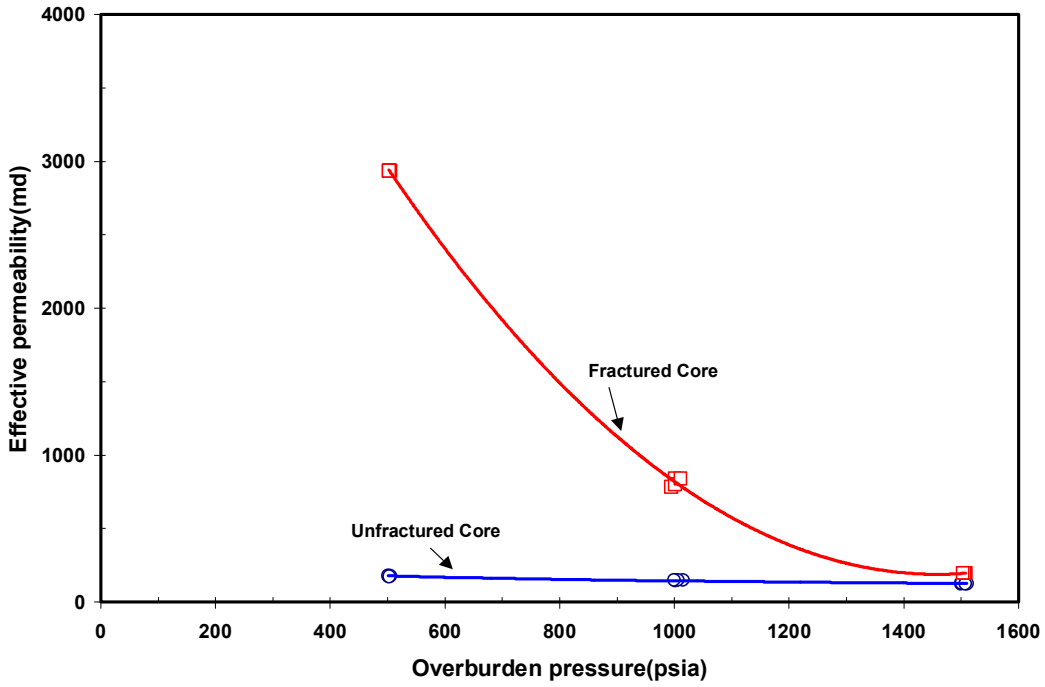

Fig. 4.3 – Permeability reduction due to hydrostatic stress.

The resistance to fluid flow in fractures is less compared to the matrix. The fluid, therefore, tends to take the preferential path of the fractures rather than flowing through the matrix. Because of this reason, the effective permeability of the fractured core is higher than the matrix permeability. The increase in the hydrostatic stress tends to close the fractures and increase the resistance to fluid flow. Hence the effective permeability of the fractured core reduces greatly with the increase in the hydrostatic stress. The effective permeability of the fractured core will be close to the matrix permeability at higher

hydrostatic stress, but still there will be some effect of fractures. This is because the fractures are not completely healed even at a higher stress. Hence there will be a residual effect of fractures on the effective permeability of the core as is evident from Fig. 4.3.

Fig. 4.4 shows the normalized permeability of both the unfractured and fractured core against overburden pressure at a flow rate of 5 cm^3/min. Reference pressure is fixed at 500 psi for the normalized permeability plot from which the values are calculated. This plot clearly shows the deviations of permeability with respect to reference pressure. For unfractured core, the decrease is around 30%, while for fractured core, the decrease is more than 90%.

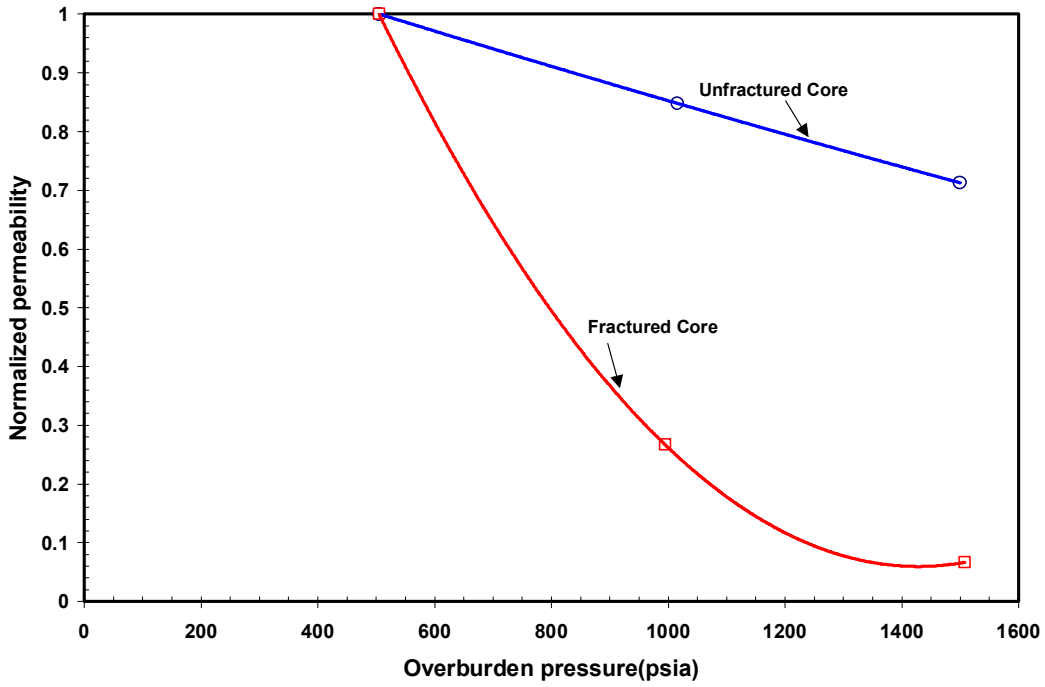

Fig. 4.4 – Normalization permeability reduction due to hydrostatic stress at injection 5 cm^3/min.

4.1.6.2 Effect of stress on fracture aperture

The fracture aperture is the width between the fracture surfaces. The fracture aperture is not uniform along the fractures and depends on the roughness of the fracture surfaces. If the fracture surface roughness is high, there will be more variations in the aperture. The aperture will be maximum at some points and minimum at other points. Hence the fracture permeability depends upon the fracture aperture distributions and the conductivity of the fractures. Since the fracture aperture is not uniform, it is very difficult to quantify fracture aperture at all points of the fracture path experimentally. Hence the assumption of parallel plate is used for calculating the mean fracture aperture. The formula for calculating the fracture aperture using the above assumption is presented in the earlier chapter (refer Chapter III). The fracture aperture also depends upon the physical properties of the core and also depends on the size of the core sample. The matrix permeability and the effective fracture permeability greatly influence the calculation of the mean fracture aperture. Fig. 4.5 shows the plot of fracture aperture against overburden pressure.

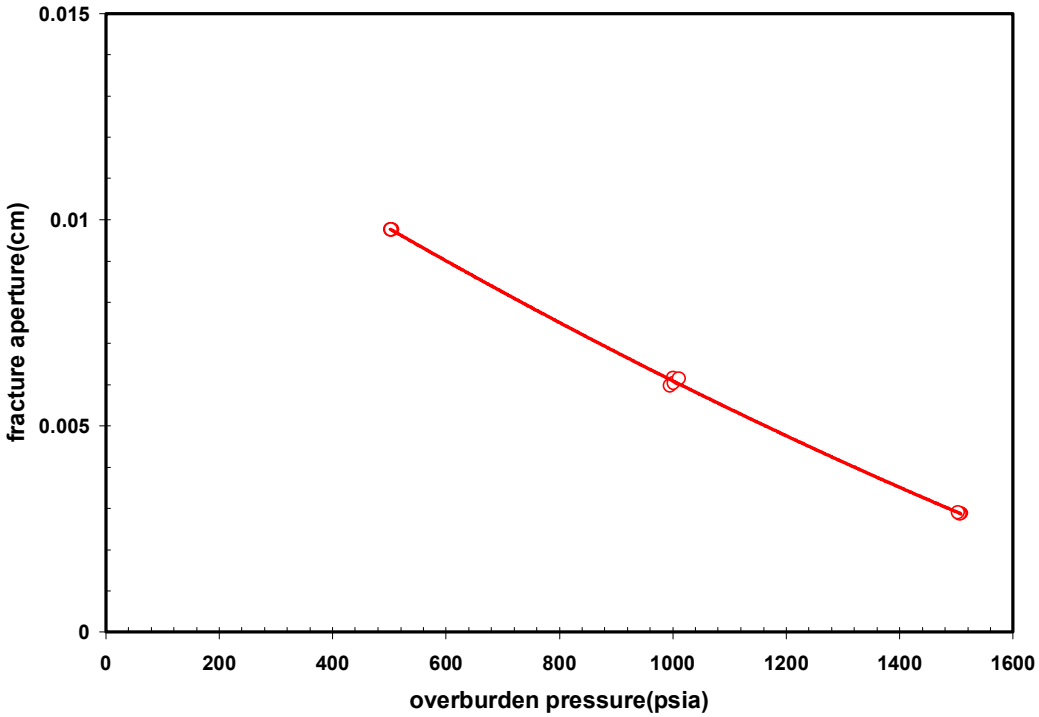

Fig. 4.5 – Fracture aperture reduction due to hydrostatic stress for various injection rates.

The fracture aperture is calculated for different hydrostatic stress and flow rates. If the hydrostatic stress increases then the effective fracture permeability and fracture aperture decrease significantly. The fracture aperture is more dependent on the effective fracture permeability than on matrix permeability since the variations of the matrix permeability with increase in hydrostatic stress are less compared to the effective fracture permeability. The fracture aperture is almost insensitive to the increase in the injection rate.

4.1.6.3 Effect of stress on fracture permeability

The fracture permeability determination is based on the fracture aperture. The fracture permeability is defined as the conductivity of the fractures to the fluid flow in the fractured core. Fig. 4.6 shows the variations of fracture permeability with the increase in the hydrostatic stress.

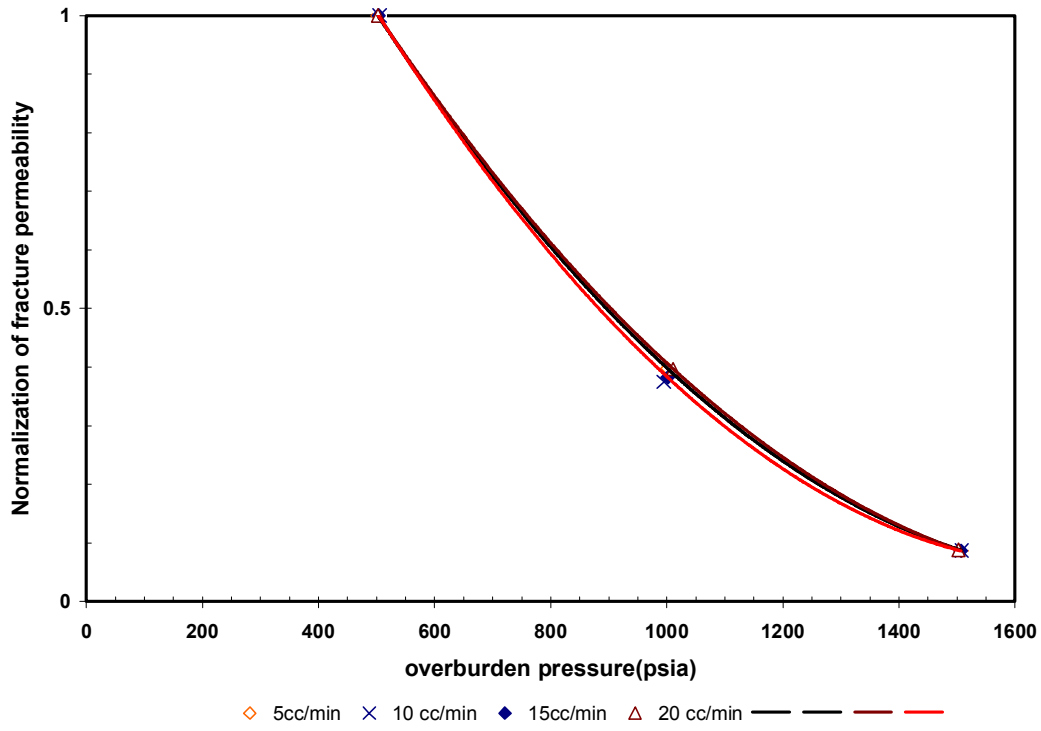

Fig. 4.6 – Fracture permeability reduction due to hydrostatic stress at different injection rate.

The effective permeability due to fractures is the combination of both fracture permeability and matrix permeability. The fracture permeability is calculated assuming the flow of fluid between the parallel plates (refer Chapter III). The fracture permeability is proportional to the square of the fracture aperture by combining the viscous and the Darcy equation for flow. Usually the fracture permeability is very high compared to the matrix permeability; and hence, the fluid tends to flow through the fracture with relative ease compared to the matrix. However, the fracture permeability decreases significantly with the increase in the hydrostatic stress.

4.1.6.4 Effect of stress on fracture and matrix flow rates

The fracture flow rate depends on the fracture permeability and the fracture aperture. The fluid flow in fracture and the matrix depends on the injection rate. The fluid will rush in the fractures since the fracture permeability is high compared to the matrix. But the volumetric rate of the fracture region is small compared to the matrix block, hence, some of the fluid diverts to matrix block. The flow rate through the fracture depends on the fracture permeability and fracture aperture. If the hydrostatic stress increases, the fracture permeability and aperture decrease, this also decreases the volumetric rate of the fracture region. Therefore at high hydrostatic stress, the fluid flow is not dominant in the fracture anymore although some amount of the flow still occurs due to the non-healing nature of the fractures as presented in Figs. 4.7 and 4.8.

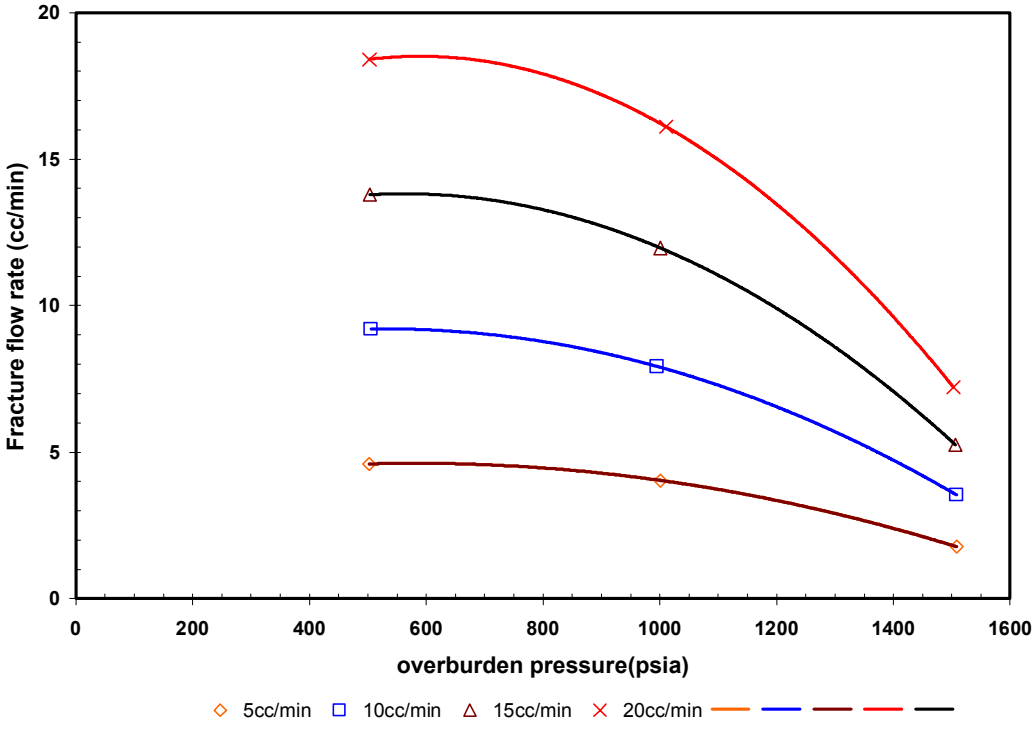

Fig. 4.7 – Effect of hydrostatic stress on fracture flow rate at different injection rates.

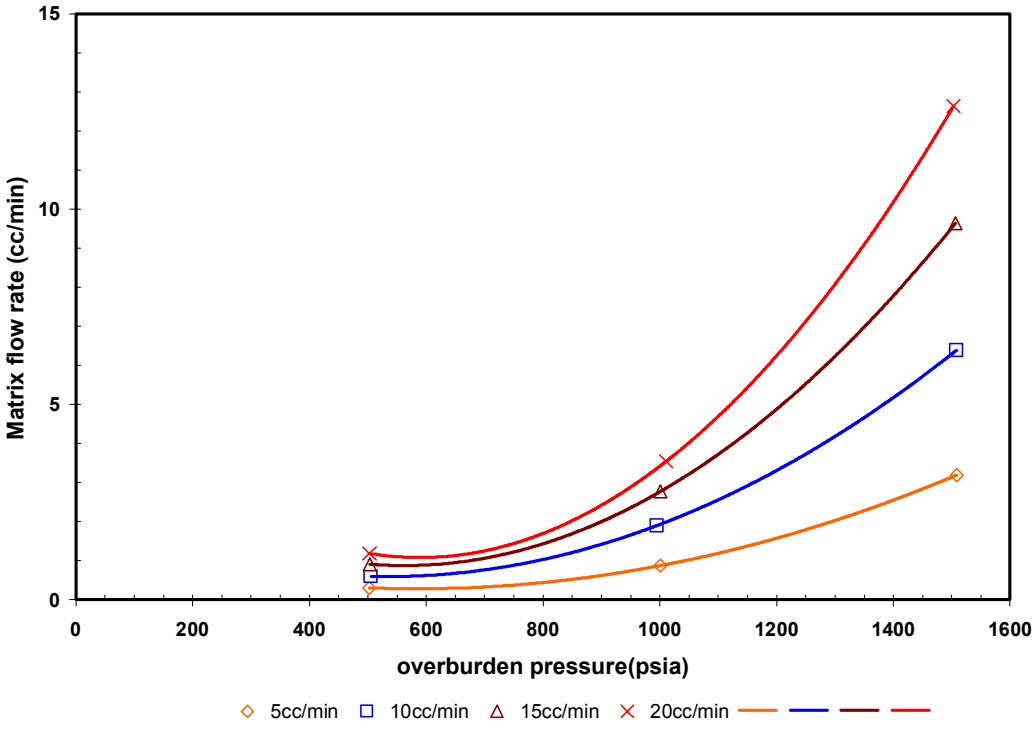

Fig. 4.8 – Effect of hydrostatic stress on matrix flow rate at different injection rates.

4.2 Triaxial stress experiments

Triaxial stress state is the condition in which axial stresses are lesser than overburden pressure. In this study, the permeability changes at different triaxial pressure conditions are investigated. Thus, overburden and axial pressures generated from hydraulic jacks were applied to cylindrical core (Fig. 4.9). In this experiment, axial stresses are kept equal to one-third of overburden pressure.

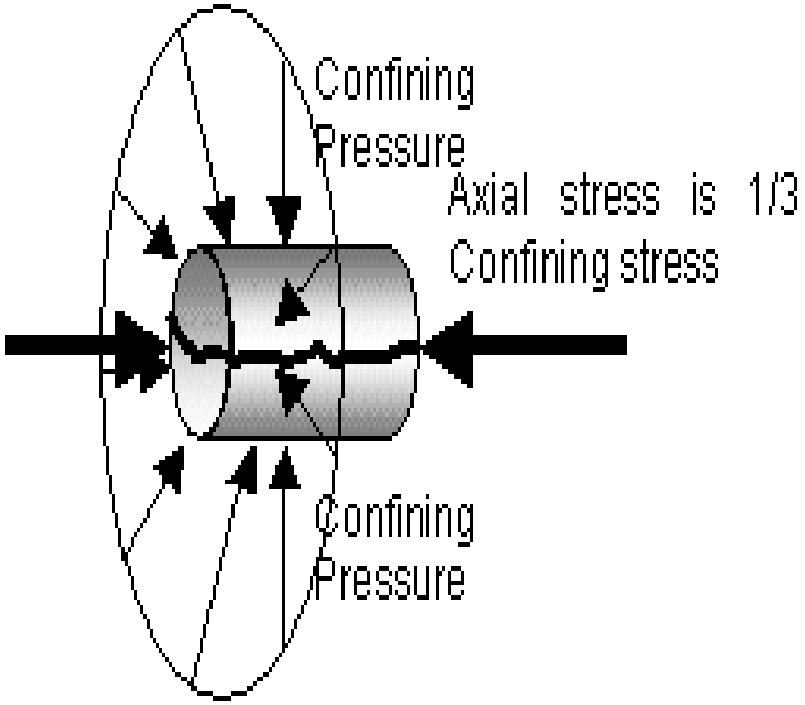

Fig 4.9 – Triaxial stress condition.

4.2.1 Experimental description

The core sample is subjected to both overburden pressure and axial stress. The axial stress is kept at one-third of the overburden pressure for the triaxial experiment. Matrix permeability is evaluated at various confining pressures and at various injection rates. The cores are then fractured subsequently and the effective permeability due to fractures is evaluated at various confining pressures and injection rates. The parameters are plotted against overburden pressure to study the effect of confining stress.

4.2.2 Berea cores

Berea sandstone was used in this study. The diameter of the sample is 3.59664 cm and the length is 5.047 cm. The dimensions are the average values of 3 to 4 measurements using a vernier caliper. The bulk volume of the sample is 53.23 cm^3. The pore volume and porosity are calculated as discussed before under hydrostatic loading. The pore volume is calculated as 12.55 cm^3 and porosity is calculated as 23.58%. The core saturation was carried out as explained before under hydrostatic loading.

4.2.3 Core flooding

The saturated core sample is inserted in the Hassler-Type core holder. Overburden pressure is applied in the radial direction and axial tension is applied along the axis of the core, perpendicular to the overburden pressure. An initial overburden pressure of 500 psi is applied. This is followed by core flooding with the brine solution at flow rates of 5, 10, 15 and 20 cm^3/min. The pressure drop across the core is recorded in the transducer. The experiments are repeated for overburden pressures of 1000 psi and 1500 psi and the corresponding pressure drops are recorded. Subsequently, the core is fractured along the axis and the experiment is repeated as before for the fractured core. The experiment can be performed for the two-phase flows as shown in the Fig. 4.10. However, the focus for these experiments is on the single-phase flow.

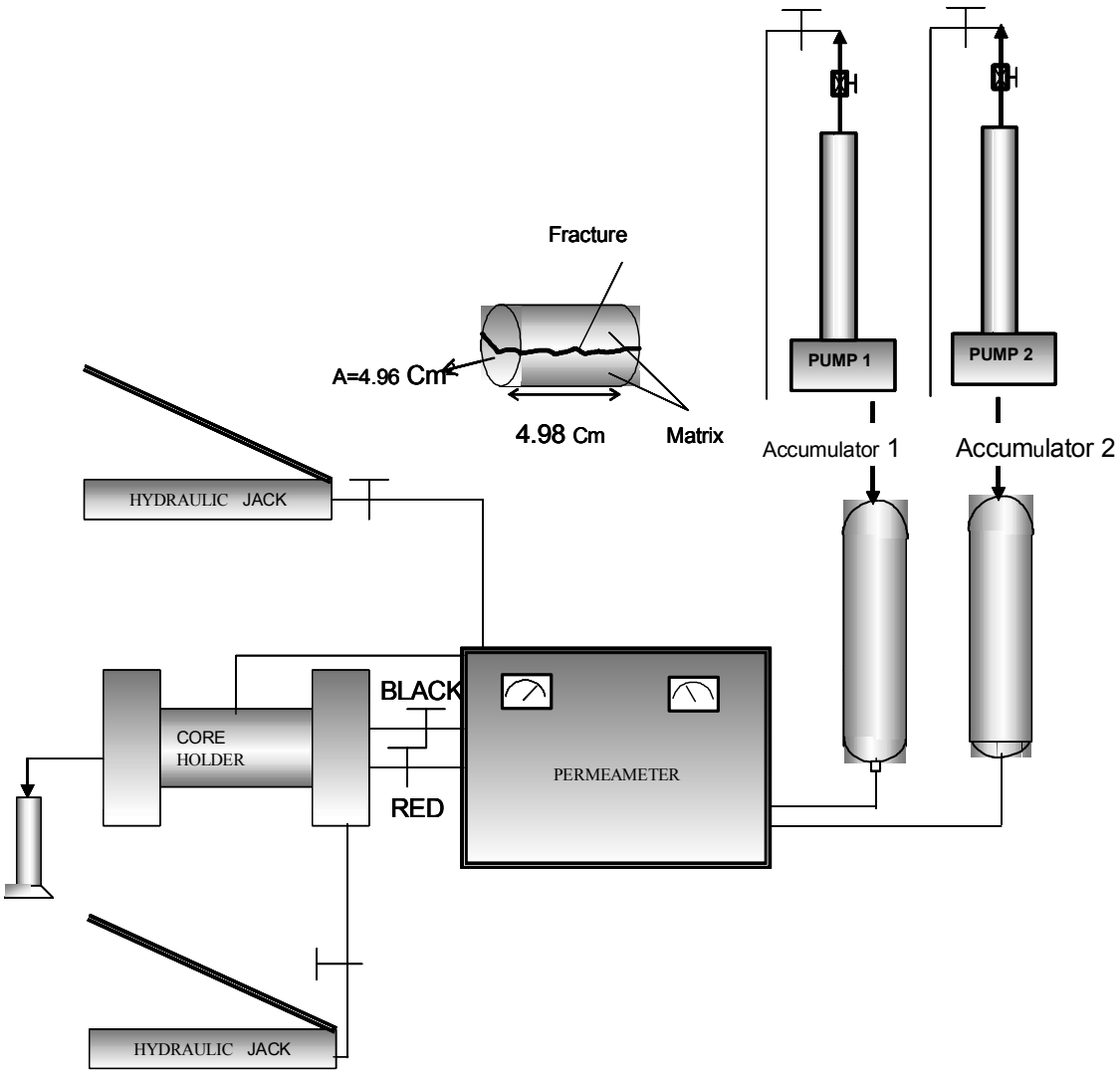

Fig. 4.10 - Triaxial stress experiment apparatus.

4.2.4 Discussion of experimental results

4.2.4.1 Effect of stress on permeability

Permeability of the rock decreases with the increase in the applied stress. Fig. 4.11 shows the effect of overburden pressure on permeability of both the unfractured and the fractured core. The permeability is reduced in both cases by an increase in stress level; however, the decrease in permeability of the unfractured core is much less compared to the fractured core.

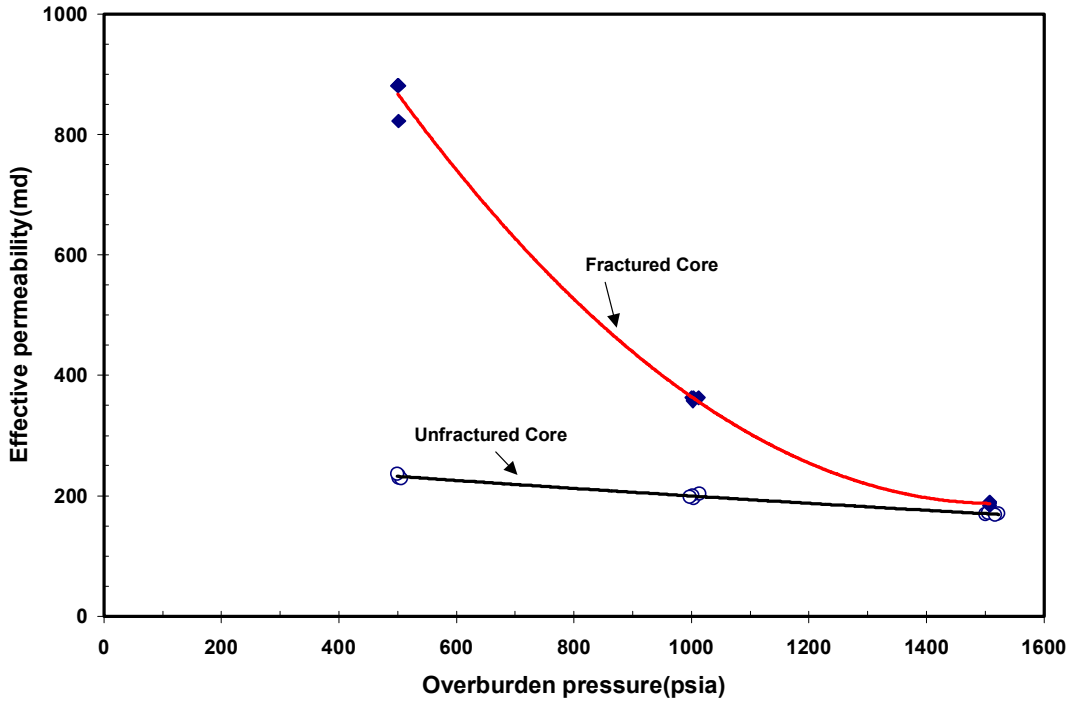

Fig. 4.11 – Permeability reduction due to triaxial stress.

The increase in the triaxial stress tends to close the fractures and increase the resistance to fluid flow. Hence the effective permeability of the fractured core decreases significantly with the increase in triaxial stress. At 1500 psia, the effective permeability of the fractured core converges to matrix permeability due to the closing of fracture aperture. Fig. 4.12 shows that the matrix permeability decreases about 20% from its initial permeability compare to 80% permeability reduction of fractured core at the same triaxial stress.

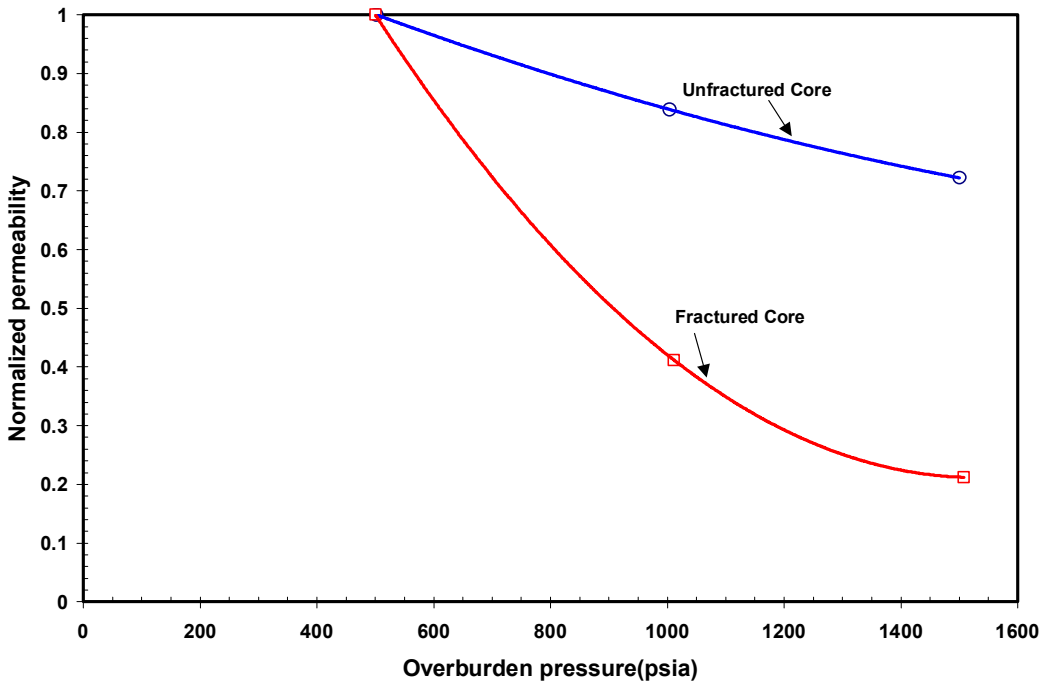

Fig. 4.12 – Normalization permeability reduction due to triaxial stress.

4.2.4.2 Effect of stress on fracture aperture

The fracture aperture is calculated for different triaxial stress and flow rates. If the triaxial stress increases then the effective fracture permeability and fracture aperture decrease significantly, this is a similar response to previously applied stresses (uniaxial and hydrostatic stresses). Again it shows that the fracture aperture is almost insensitive to the increase in the injection rate. Fig. 4.13 shows the plot of fracture aperture against overburden pressure.

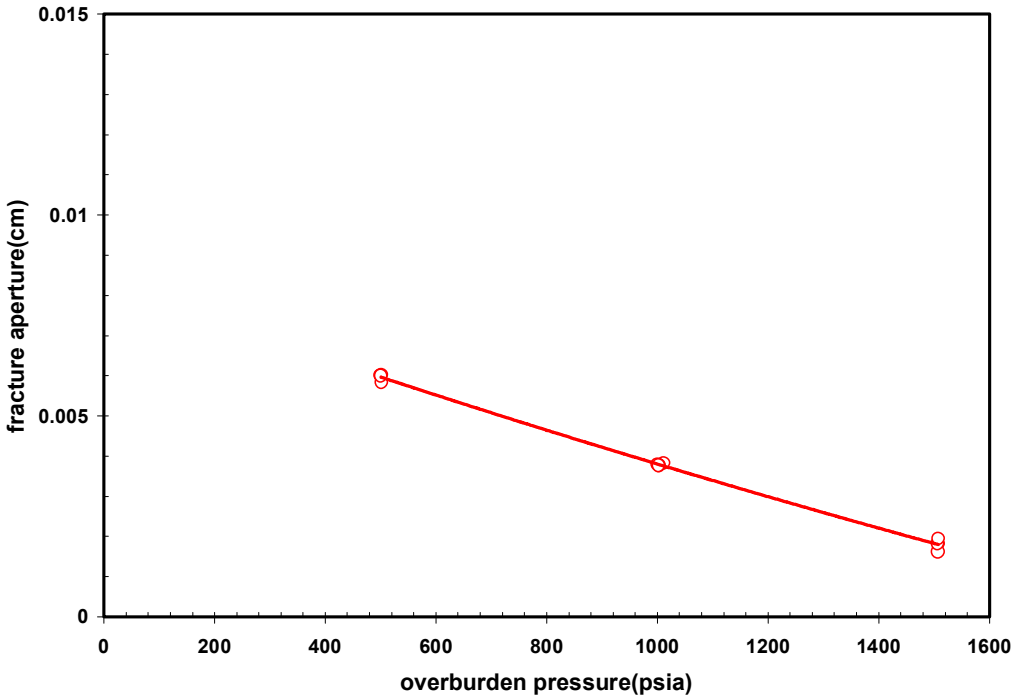

Fig. 4.13 – Fracture aperture reduction due to triaxial stress.

4.2.4.3 Effect of stress on fracture permeability

The fracture permeability determination is based on the fracture aperture. However, the fracture permeability decreases greatly with the increase in the triaxial stress. Fig. 4.14 shows the variations of fracture permeability with the increase in triaxial stress.

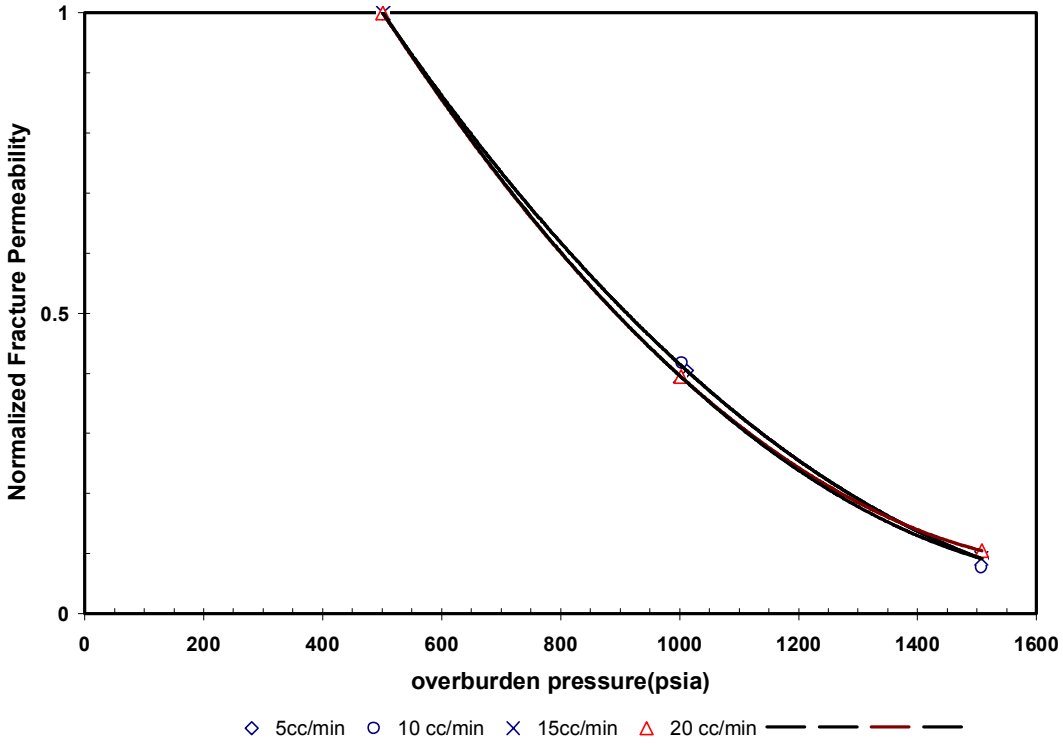

Fig. 4.14 – Normalized fracture permeability reduction due to triaxial stress.

4.2.4.4 Effect of stress on fracture flow rate

The fracture flow rate depends on the fracture permeability and the fracture aperture. The rate of flow through the fracture depends on the fracture permeability and fracture aperture. If the triaxial stress increases, the fracture region becomes small and the flow of the fluid is not dominant in the fracture, although some amount of the flow occurs due to the non-healing nature of the fractures. Hence, the fracture flow rate decreases with increase in the triaxial stress. Fig. 4.15 shows the plot of fracture flow rate against overburden pressure at various flow rates.

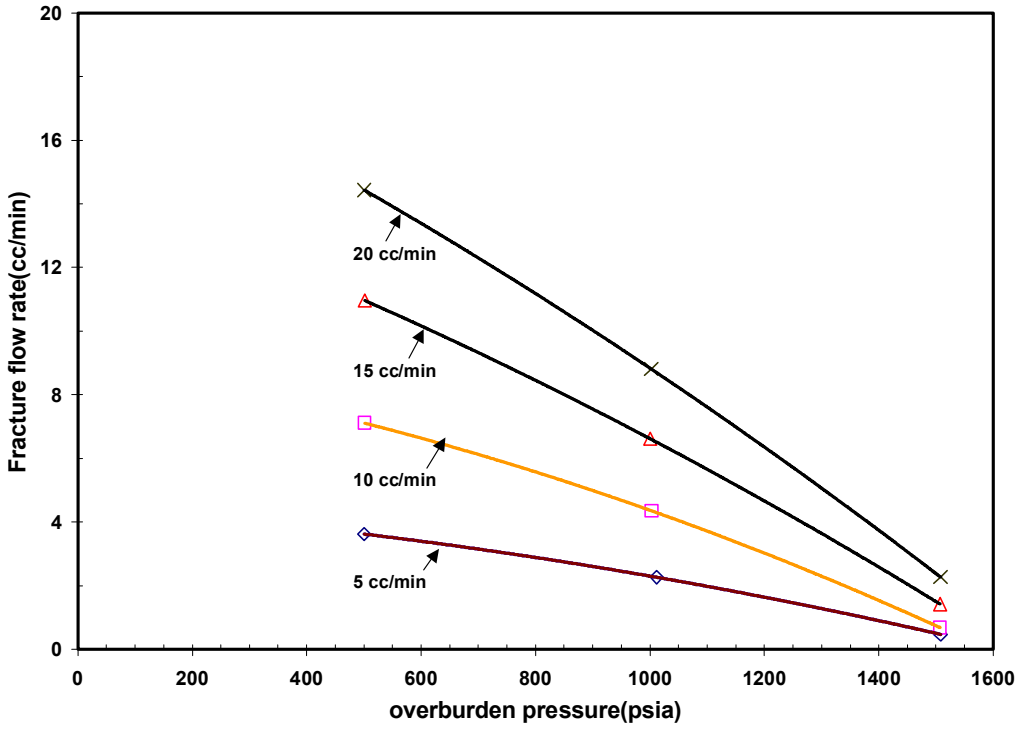

Fig. 4.15 – Effect of triaxial stress on fracture flow rate.

4.2.4.5 Effect of stress on matrix flow rate

The matrix flow rate depends on the matrix permeability and the fracture aperture. The presence of a fracture reduces the flow through the matrix because the resistance is least in the fracture. However the increase of triaxial stress closes the fracture aperture and hence the matrix flow rate dominates. Fig. 4.16 shows the plot between matrix flow rate and the overburden pressure at various injection rates.

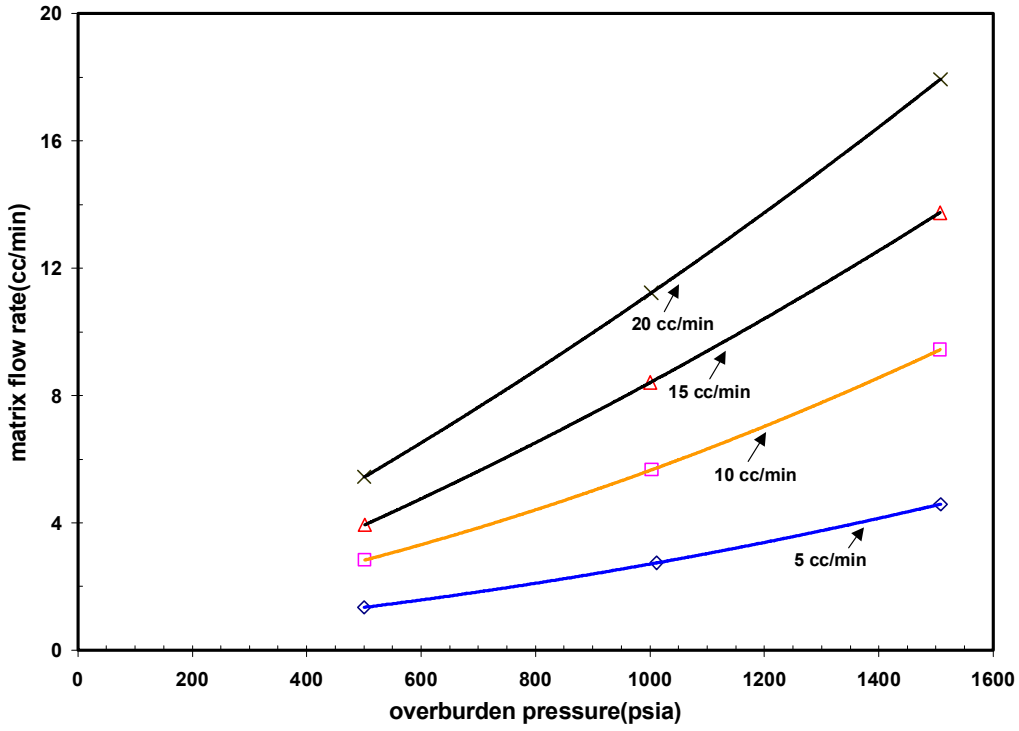

Fig. 4.16 – Effect of triaxial stress on matrix flow rate at different injection rates.

4.3 Comparison of uniaxial, triaxial and hydrostatic results

It has been proven in many literatures that the stress state in the reservoir is best described by true triaxial stress condition (Al-Harthy *et al.*[48], Holt[16]). Hence the purpose of this study is to verify whether uniaxial and hydrostatic stress condition can also represent the reservoir conditions. Hence a comparison of different stress conditions with respect to triaxial stress condition should be performed to verify that the stress conditions can adequately represent the reservoir conditions. The results of uniaxial stress condition are given in Chapter III. The results of hydrostatic and triaxial stress conditions are given in the previous sections. Fig. 4.17 shows the difference of all the stress conditions. Axial stresses are not considered in the uniaxial condition. Axial stresses are equal to overburden pressure in case of hydrostatic condition. In case of triaxial condition, the axial stresses are different and are lesser than the overburden pressure.

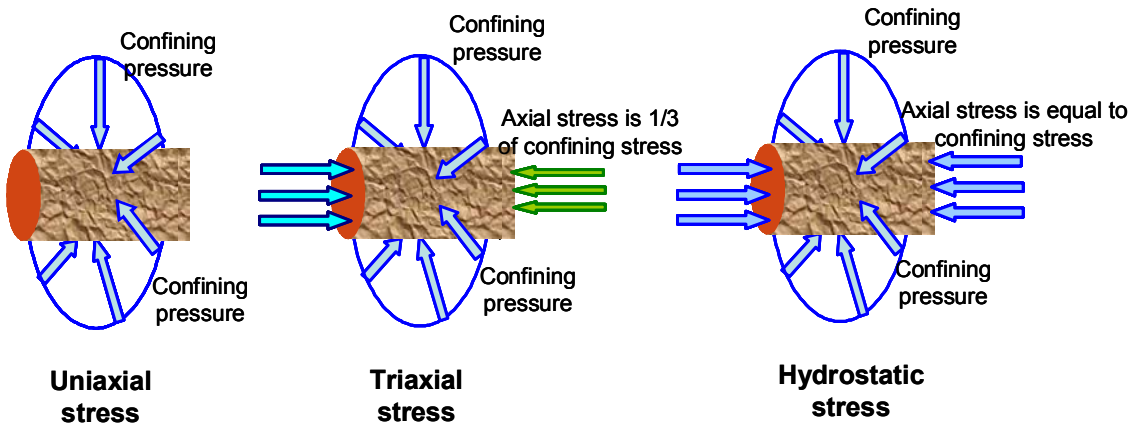

Fig. 4.17 - Illustration of uniaxial, triaxial and hydrostatic stresses.

4.3.1 Effect of stress on permeability of an unfractured core

As mentioned earlier that permeability of the core reduces with the increase in the applied stress. Three types of applied stress used in our experiments are uniaxial, triaxial and hydrostatic stresses. The difference between those stresses is illustrated in Fig. 15. The uniaxial stress has uniform stress around the body of the core (confining stress), but no axial stress applied in the axis of the core. The triaxial stress has the confining stress and also has an axial stress applied along the axis of the core. The axial stress is kept one-third of the confining stress. The hydrostatic stress has uniform confining and axial stresses. Fig. 16 shows clearly that hydrostatic stress has the highest impact on permeability reduction followed by triaxial and uniaxial stresses. The permeabilities are normalized and plotted against overburden pressure for the comparison of the results.

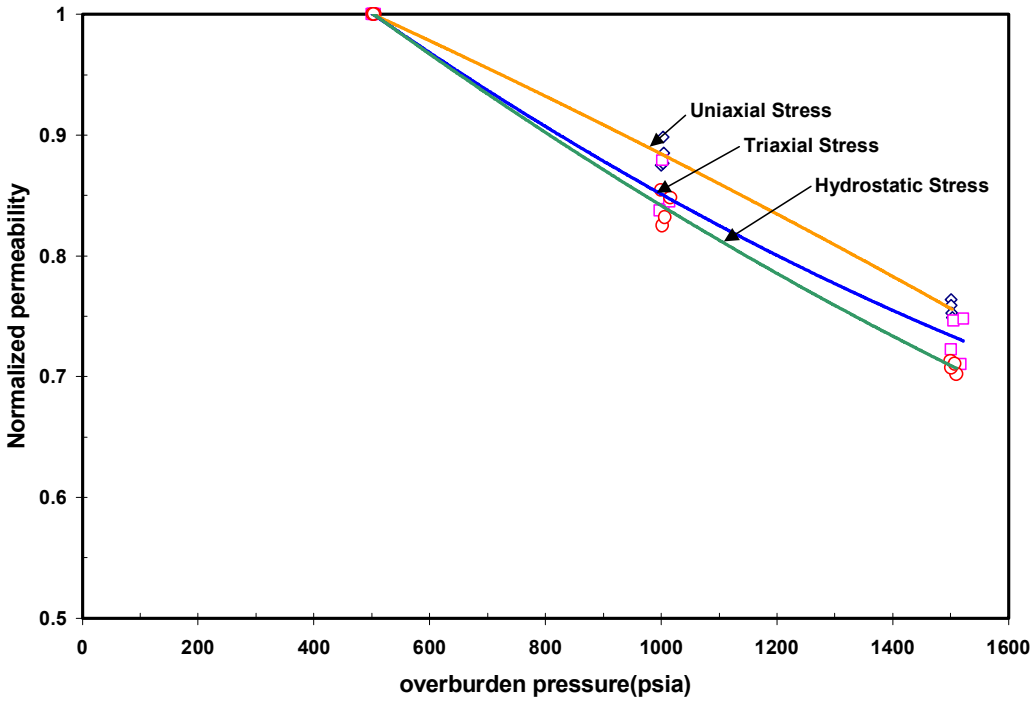

Fig. 4.18 – Comparison of matrix permeability reduction due to different applied stresses.

4.3.2 Effect of stress on permeability of fractured core

The permeability of the fractured core decreases with the increase in the applied stress. As discussed in the previous section, the reduction in permeability is more in case of hydrostatic stress since the applied stress is more than that of triaxial condition. Fig. 4.19 is the plot between the normalized effective permeability due to fracture against overburden pressure. As we can clearly see, hydrostatic stress condition grossly underestimates permeability of fractured core and hence might not be useful to represent reservoir conditions. The reduction in the effective permeability due to fracture is more than the reduction in the matrix permeability in the unfractured core. The residual effects of the fracture at higher pressure are due to the fact that the fracture does not heal completely even at higher stress.

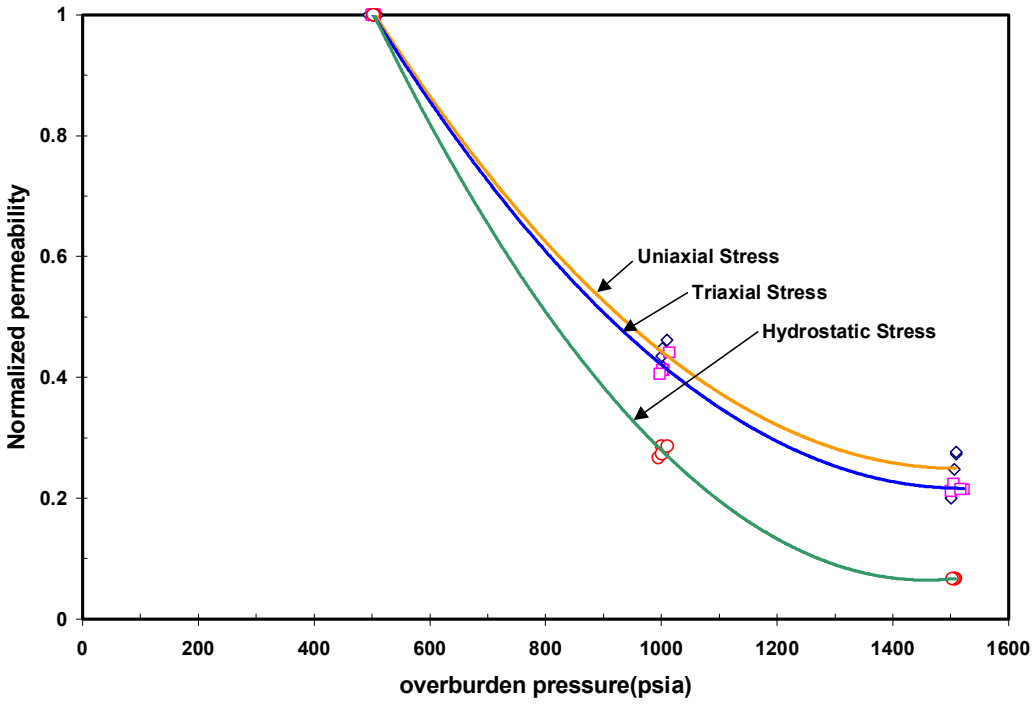

Fig. 4.19 – Comparison of effective permeability reduction due to different applied stresses.

4.3.3 Effect of stress on fracture aperture

The fracture aperture greatly depends on the applied stress. The fracture aperture variation depends on the fracturing technique. In the laboratory, the cores are fractured using a hydraulic cutter. The fracture aperture depends on the load applied on the core while cutting. The usual trend is that the fracture aperture decreases significantly with the increase in the applied stress. Fig. 4.20 is the plot between fracture aperture and the overburden pressure for a flow rate of 5 cm^3/min. There is not much difference between the hydrostatic and triaxial stress conditions.

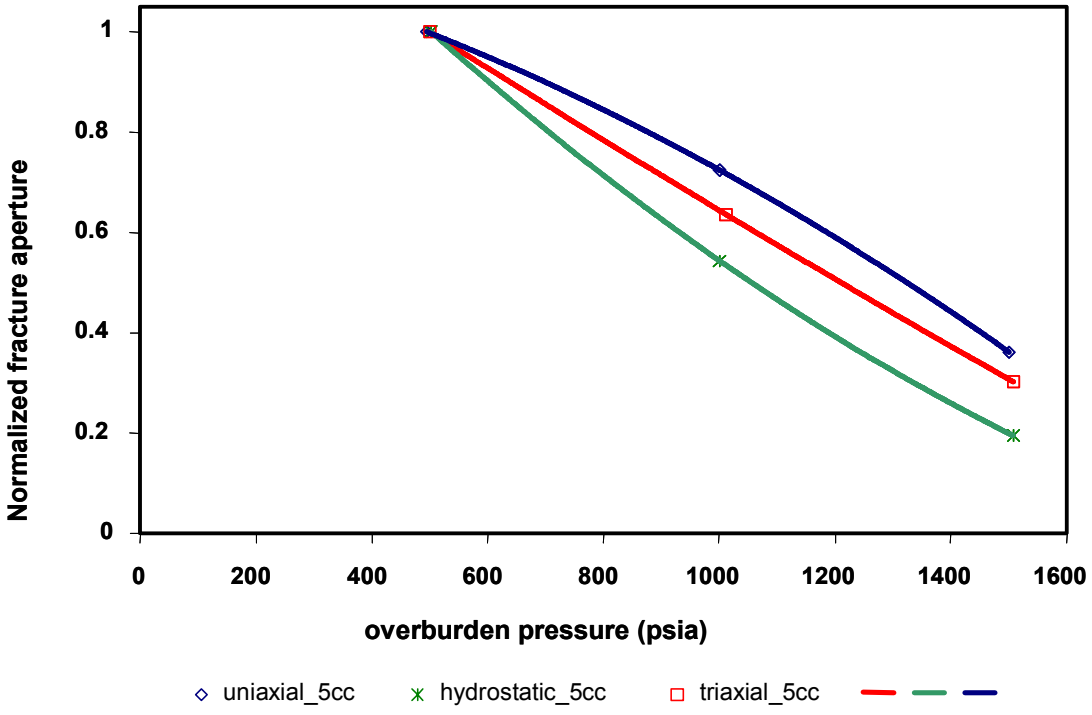

Fig. 4.20 – Comparison of fracture aperture reduction due to different applied stresses at injection rate of 5 cm^3/min.

4.4.4 Effect of stress on fracture permeability

The fracture permeability depends on the fracture aperture. The fracture permeability decreases greatly with the increase in the applied stress since the fracture aperture decreases significantly. Fig. 4.21 is the plot between the overburden pressure and the fracture permeability. The difference between triaxial stress condition and uniaxial condition is less compared to the difference between triaxial condition and hydrostatic condition.

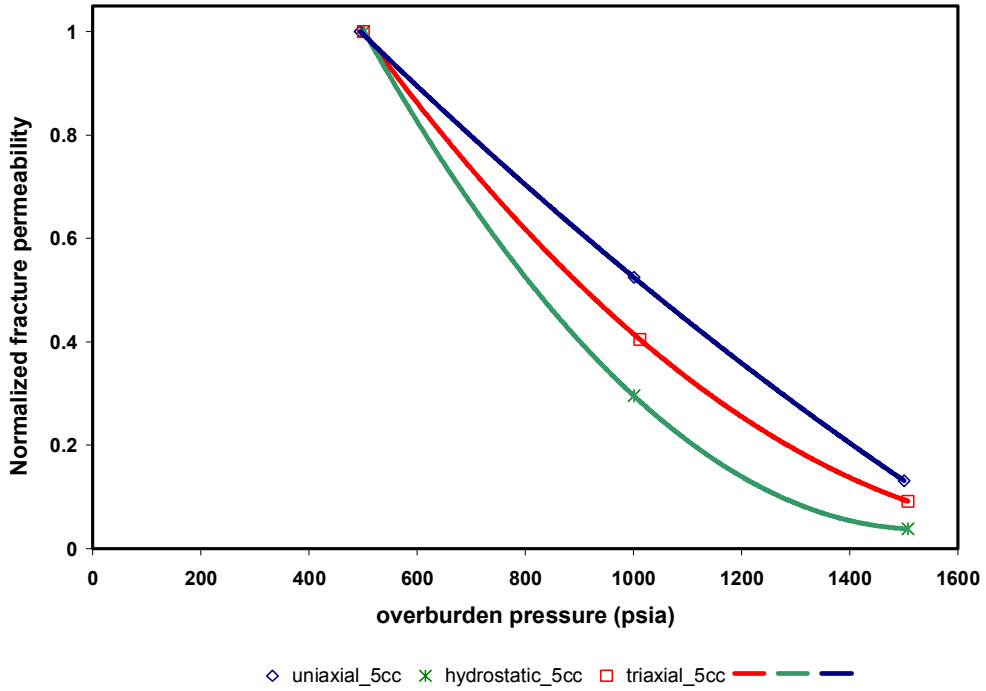

Fig. 4.21 – Comparison of fracture permeability reduction due to different applied stresses at injection rate of 5 cm^3/min.

CHAPTER V

CALIBRATION AND DISTRIBUTION OF FRACTURE APERTURE USING X-RAY CT SCANNER

5. 1. X-ray tomography

5.1.1 Introduction

X-ray computer tomography (X-ray CT) is a method in the area of non-destructive testing (NDT). It was developed during the seventies for medical purposes and was subsequently introduced for industrial applications in the latter part of the eighties. It is an imaging technique, similar to X-ray radiography, the only difference being the way X-ray radiation penetrates an object. Figs. 5.1 and 5.2 show the basic difference between X-ray radiography and X-ray CT. A CT image generates a slice through the object in a true geometrical manner whereas X-ray radiography image projects a three-dimensional picture into two-dimension. Thus the CT image shows maps of the amount of radiation that is taken away (attenuated) in the form of linear attenuation coefficient, μ, from a beam of X-ray at each point (voxel -3D value) of the object. The value of μ depends on the density and the atomic composition of the matter in which X-ray propagates. In contrast, the X-ray radiographic image pixel values are proportional to the radiation attenuated along the line from the X-ray source to the detector element (film in Fig. 5.1 but a digital detector in Fig. 5.2). Radiography is faster as compared to CT scanning, but it is inferior when it comes to revealing interior details of the imaged object.

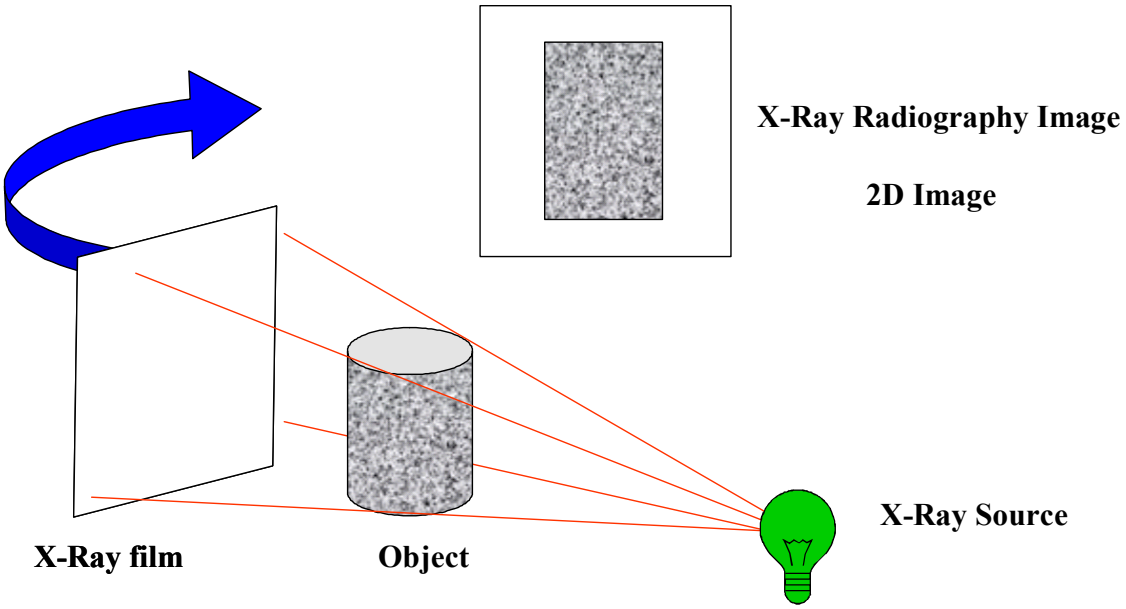

Fig. 5.1 Conceptual representation of X-ray radiography

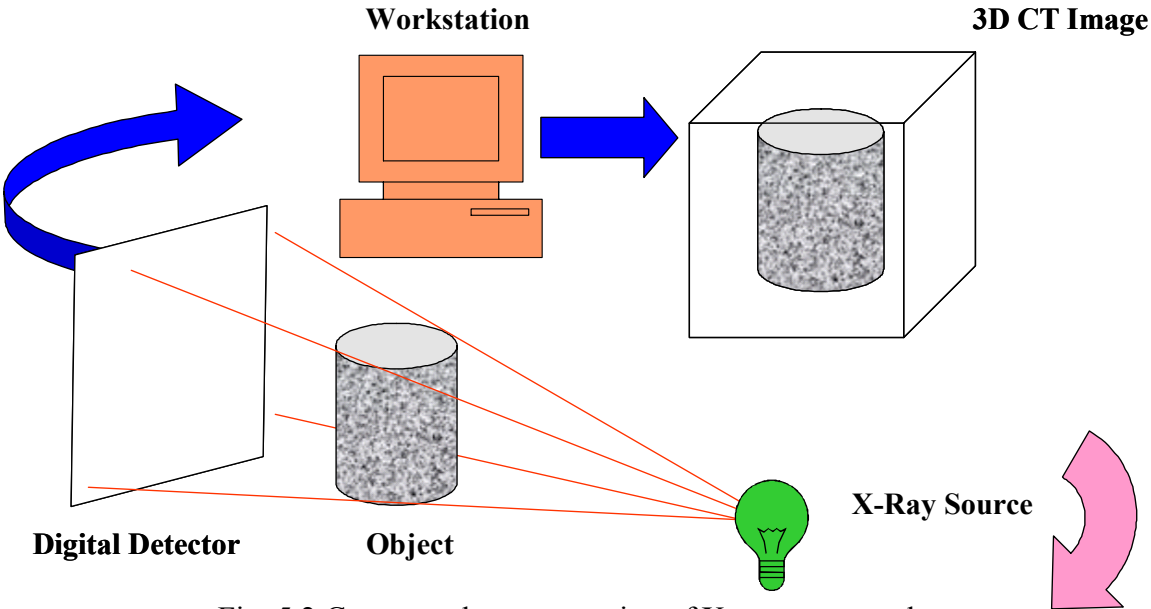

Fig. 5.2 Conceptual representation of X-ray tomography

In our experiments we are taking CT images of cores and rock objects, which give the projection of internal structures. It sometimes becomes necessary that over-laying grains obscure certain important details, which need study. By using slice-imaging techniques (tomography), we can selectively have a layer by layer structural detail of the given core sample. With computerized tomography, we can see sequence images of thin consecutive slices of the cores or rock object in three dimensions. Unlike conventional, classical tomography, computerized tomography does not suffer from interference from structures in the object outside the slice being imaged. This is done by irradiating only thin slices of the object with a fan-shaped beam. Also, the CT images (tomograms) of the object's structure can give more selective information within the object than conventional planar projection radiographs. Compared to planar radiography, CT images have superior contrast resolution, i.e., they are capable of distinguishing very small differences in attenuation (contrasts), but have inferior spatial resolution. The maximum spatial resolution of X-ray scan is 0.5 mm, which implies that the smallest details in the image that can be resolved, must be separated at least 0.5 mm. This drawback in X-ray CT has lead to the refinement in X-ray microtomography. In X-ray microtomography, a spatial resolution of 2 micron (2 thousandths of a millimeter) and below can be achieved.

X-ray CT scanners used nowadays are either third- generation or fourth-generation. Fig. 5.3(a) shows a third-generation CT scanner. The X-ray tube and the receptor array are located on opposite sides of the object and both rotate around the object during data acquisition. Fig. 5.3(b) is a fourth-generation CT scanner. Here, only the X-ray tube rotates around the object; the receptor array, which is situated in the outside of the scanning frame, remains stationary. The receptors are made from solid-state material and can be as many as 4000. CT scanners are also available in which the X-ray tube circles the object while the table moves continuously, so that the X-ray tube moves in a spiral orbit around the object. These are called spiral CT scanners. Department of Petroleum Engineering, Texas A&M University, now has a fourth generation spiral CT scanner.

5.1.2 Principles of operation

In order to generate a CT image two steps are necessary. Firstly we should have physical measurements of the attenuation of X-rays along the core in different directions, and secondly we have to make mathematical calculations of the linear attenuation coefficients, μ, all over the slice.

A fan-shaped beam, wide enough to pass on both sides of the core or rock object, is used. The image receptor is an array of several hundred small separate receptors. Readings from the receptors are fed into a computer, which after numerous calculations produces a tomogram of the object, i.e., a map of linear attenuation coefficients, μ. The data acquisition time is a few seconds and a 512 pixel x 512 pixel image matrix. Typically medical CT scanners today use a fan-beam, ones which are having about 700 receptors (3rd generation) or 4000 receptors (4th generation), complete data acquisition in approximately 1-2 seconds and a few seconds to reconstruct the 512x512 image matrix with 12 or 16 bits depth.

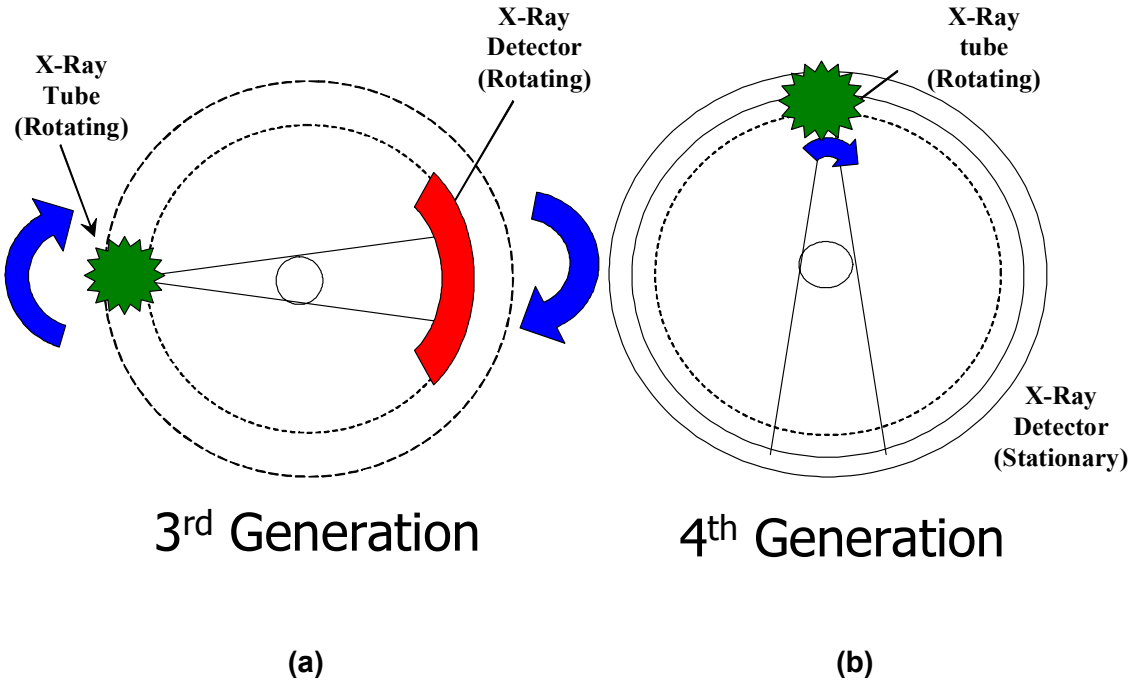

Fig. 5.3 Conceptual representation of 3rd generation and 4th generation X-ray CT scanner.

X-ray CT is one of the forms of digital radiology. When X-rays interact with matter, there are three primary interaction modes: photoelectric, Compton and coherent. When the photoelectric effect occurs, a photon from the incident beam disappears, and an electron is ejected from the inner shell of an atom. As shown in Fig. 5.4(a) an incident photon loses all its energy on entering an atom, being absorbed in the process. The atom responds, by ejecting an inner shell electron, which becomes a photoelectron (Fig. 5.4(b)). The atom reaches an excited state and an electron from a higher energy level fills the vacancy and emits a characteristic X-ray photon Fig. 5.4(c).

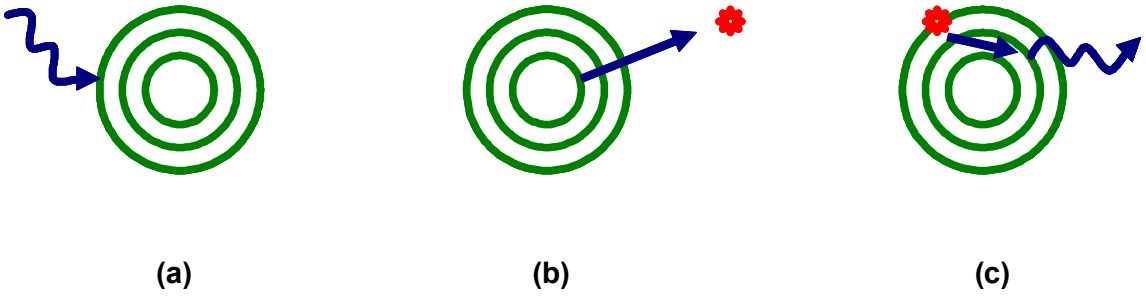

Fig. 5.4 Photoelectric effect.

In Compton scattering, Fig. 5.5, a photon from the incident beam collides with an electron, loses some of its energy and is deflected from its original direction.

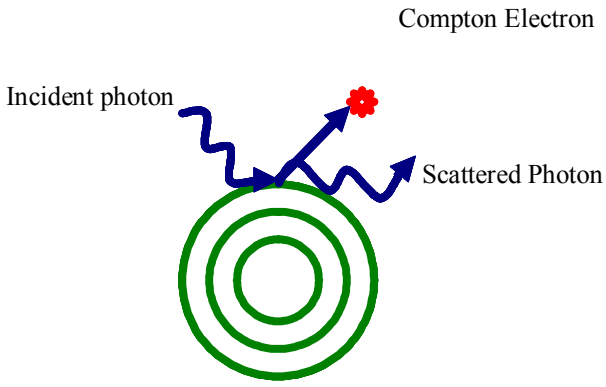

Fig. 5.5 Compton effect.

In coherent (or Rayleigh) scattering, Fig. 5.6, an incident photon is scattered by bound atomic electrons without losing energy and the atom is neither ionized nor excited. Thus, when a narrow beam of monoenergetic photons passes through a medium of thickness x, the beam will be attenuated and scattered because of the three above cited effects. The receptors measure the X-rays passing through a slice of the object in different positions. This forms one projection of the object. Its reading gives us a measure of the attenuation in the object along the path of a particular ray.

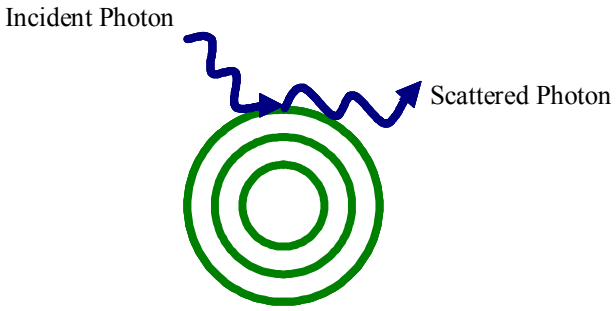

Fig. 5.6 Rayleigh scattering.

For a homogeneous object, the receptor reading, as stated by *Huang*, is given by:

$$I = I_0 e^{-\mu x} \quad \text{..... (13)}$$

where,

I_0 is the receptor reading without the object,

μ the linear attenuation coefficient for the object,

x is the object thickness along the path of that ray, and

e the base of the natural logarithm (e = 2.718).

For an inhomogeneous object such as a core or a rock, the product μx is a sum over all the different grains/crystal types, i, $\Sigma\mu_i x_i$. After the readings from one of the receptors have been stored in the computer, the tube is rotated to another angle and a new projection profile measured. This procedure, called reconstruction, is applied to data from sets of projection profiles through all volume elements (voxels) and for all rotation angles (projections), in a slice of the object. An average linear attenuation coefficient, μ, for each voxel is calculated. Each value of μ is assigned a grey scale value on the display-monitor and is presented in a square picture element (pixel) of the image.

5.1.3 Reconstruction algorithms

The computer reconstructs an image, a matrix of μ-values for all voxels in a slice perpendicular to the rotation axis. The procedure to reconstruct the image is made with the help of reconstruction algorithm. The objective of this algorithm is to find the μ-values in each voxel based on all the measured data in the projection profiles. A filtering procedure helps in removing the smearing-out of the detail.

5.1.4 Display of CT numbers, N_{CT}

In the digital display computer monitor, the measured μ - values is distributed over a grey scale with the lowest values of μ black and the highest white. A CT number, N_{CT} , is defined as:

$$N_{CT} = \mu \frac{\mu - \mu_w}{\mu_w} \qquad \text{..... (14)}$$

where,

μ is the average linear attenuation coefficient for the material in a given voxel

μ_w that for water, and

N_{CT} is given in the dimensionless unit, *Hounsfield number*.

The CT number scale has two fixed values independent of photon energy. For vacuum, air or body gas,

$$N_{CT} = -1000$$

and for water,

$$N_{CT} = 0.$$

The common method used for calculating porosity from CT images is:

$$\phi = \frac{N_{CT100\%Sat} - N_{CTDry}}{N_{CTWater} - N_{CTAir}} \quad \text{..... (15)}$$

For water displacing air in the core, then saturation is given by:

$$S_w = \frac{N_{CTMat} - N_{CTDry}}{N_{CT100\%Sat} - N_{CTDry}} \quad \text{..... (16)}$$

For oil-water phase, the saturation is calculated with the help of the following relation:

$$S_w = \frac{N_{CTMat} - N_{CT100\%Sat}}{\phi\left(N_{CTOil} - N_{CTWater}\right)} \quad \text{..... (17)}$$

where, $N_{CT100\%Sat}$ is the CT number of 100% saturated voxel,

N_{CTDry} is the CT number of dry voxel,

$N_{CTWater}$ is the CT number of Water = 0.0,

N_{CTAir} is the number of Air = -1000.0,

N_{CTMat} is the CT number of the matrix,

N_{CTOil} is the CT number of Oil.

5.1.5 Image display

In order to give contrast to the object, we give a narrow interval of the CT numbers, called the window, to the entire grey scale on the display-monitor. The entire range of CT numbers is displayed on this grey scale, called the 'window width' and the average attenuation value is the 'window level'. Changes in window width, as shown in Fig. 5.7 alter the contrast and changes in window level help in selecting the structures in the image, displayed on the grey scale. As the window width is made narrower, the structure is assisted with higher contrast. Structures that are on the lower and higher sides of the window width (low and high CT numbers) are either completely black or white. As the window width is made even narrower, the contrast of the structures displayed increases. Combinations of these techniques enable small differences in attenuations at various points in the object and its composition to be visualized.

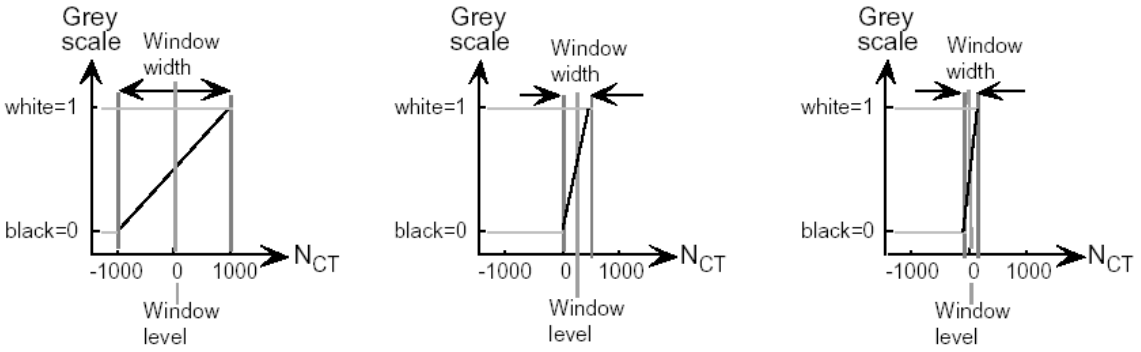

Fig. 5.7 Effect of window width and window level after *Huang*.

5.1.6 Artefacts

Computerized tomography is based on physical measurements followed by mathematical computations. These computations are based on idealized assumptions that do not entirely correspond to physical reality. This creates artefacts or errors in the measurement and reconstruction of the μ - values. Artefacts in the image are patterns that do not correspond to the object's structure. Beam hardening artifacts, as for example, are found when a spectrum of photon energies is used and is the most common form of artefact.

5.1.7 Porosity determination

Porosity distribution in the core is determined using CT-analysis method using simple correlations presented by Qadeer[49]. Each CT image is in the matrix form, in which each element, a voxel, represents a volume of 0.5 x 0.5 x 2.0 mm^3. As previously defined in eqn. 14, CT numbers are taken along the entire cross section of the core. For a dry unfractured core, for average CT numbers, we have the following relation:

$$N_{CTdry} = (1-\phi)N_{CTmatrix} + \phi N_{CTAir} \quad \text{..... (18)}$$

The dry core is then flooded with brine. The resulting CT image can be represented by the following relationship:

$$N_{CT100\%Brine} = (1-\phi)N_{CTmatrix} + \phi N_{CTBrine} \quad \text{..... (19)}$$

Subtracting eqn. (18) from eqn. (17), we have:

$$N_{CT100\%Brine} - N_{CTdry} = \phi(N_{CTBrine} - N_{CTAir}) \quad \text{..... (20)}$$

Rearranging, we derive the relation to determine the porosity of the core as:

$$\phi = \frac{N_{CT100\%Brine} - N_{CTDry}}{N_{CTBrine} - N_{CTAir}} \quad \text{..... (21)}$$

5.1.8 Saturation determination

We apply the same concept in determining the saturation of the core. If there is a mixture of two fluids in the core which is scanned, then:

$$N_{CTmixture} = (1-\phi)N_{CTmatrix} + \phi S_{FluidA} N_{CTFluidA} + \phi(1-S_{FluidA})N_{CTFluidB} \quad \text{..... (22)}$$

Rearranging,

$$N_{CTmixture} = (1-\phi)N_{CTmatrix} + \phi S_{FluidA}(N_{CTFluidA} - N_{CTFluidB}) + \phi N_{CTFluidB} \quad \text{..... (23)}$$

Subtracting eqn. 18 from eqn. 23, we have:

$$N_{CTdry} - N_{CTmixture} = \phi N_{CTAir} - \phi S_{FluidA}\left(N_{CTFluidA} - N_{CTFluidB}\right) - \phi N_{CTFluidB} \quad \ldots\ldots \quad (24)$$

Rearranging,

$$S_{FliudA} = \frac{N_{CTdry} - N_{CTmixture} + \phi(N_{CTFluidB} - N_{CTAir})}{\phi\left(N_{CTFluidA} - N_{CTFluidB}\right)} \quad \ldots\ldots\ldots\ldots\ldots\ldots\ldots\ldots\ldots\ldots \quad (25)$$

From eqn. 21, for fluid B we have:

$$\phi = \frac{N_{CTMat} - N_{CTDry}}{N_{CTFluidB} - N_{CTAir}} \quad \ldots\ldots\ldots\ldots\ldots\ldots\ldots\ldots\ldots\ldots\ldots\ldots\ldots\ldots\ldots\ldots\ldots\ldots\ldots\ldots\ldots\ldots \quad (26)$$

Substituting this in eqn. 25, we have eqn. 17 as given previously.

5.1.9 Experimental equipment

The aluminum core holder can handle 1 inch cores. Aluminum was selected because it absorbs the least amount of X-rays. It is proposed that 1inch x 12 inches cores be used. The layout of the core holder is shown in Fig. 5.8 and Fig. 5.9.

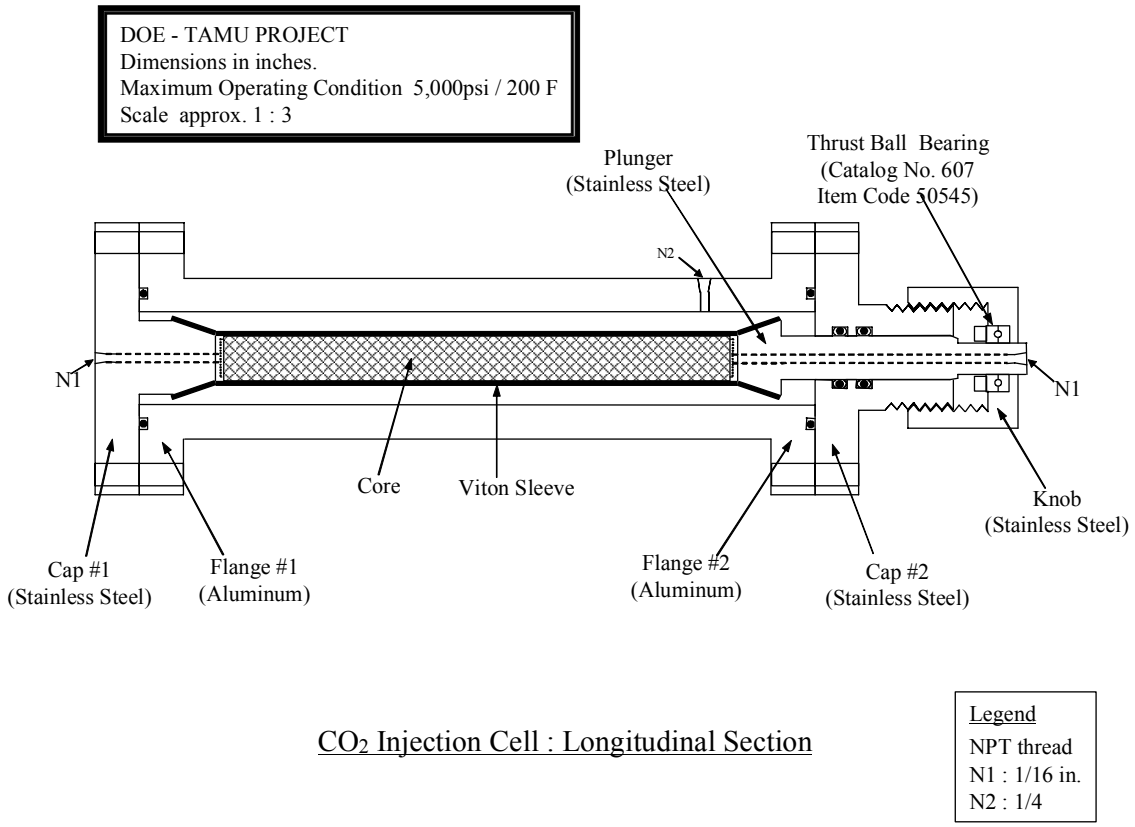

CO_2 Injection Cell : Longitudinal Section

Fig. 5.8 – Design of aluminum core holder used for X-ray CT scanning.

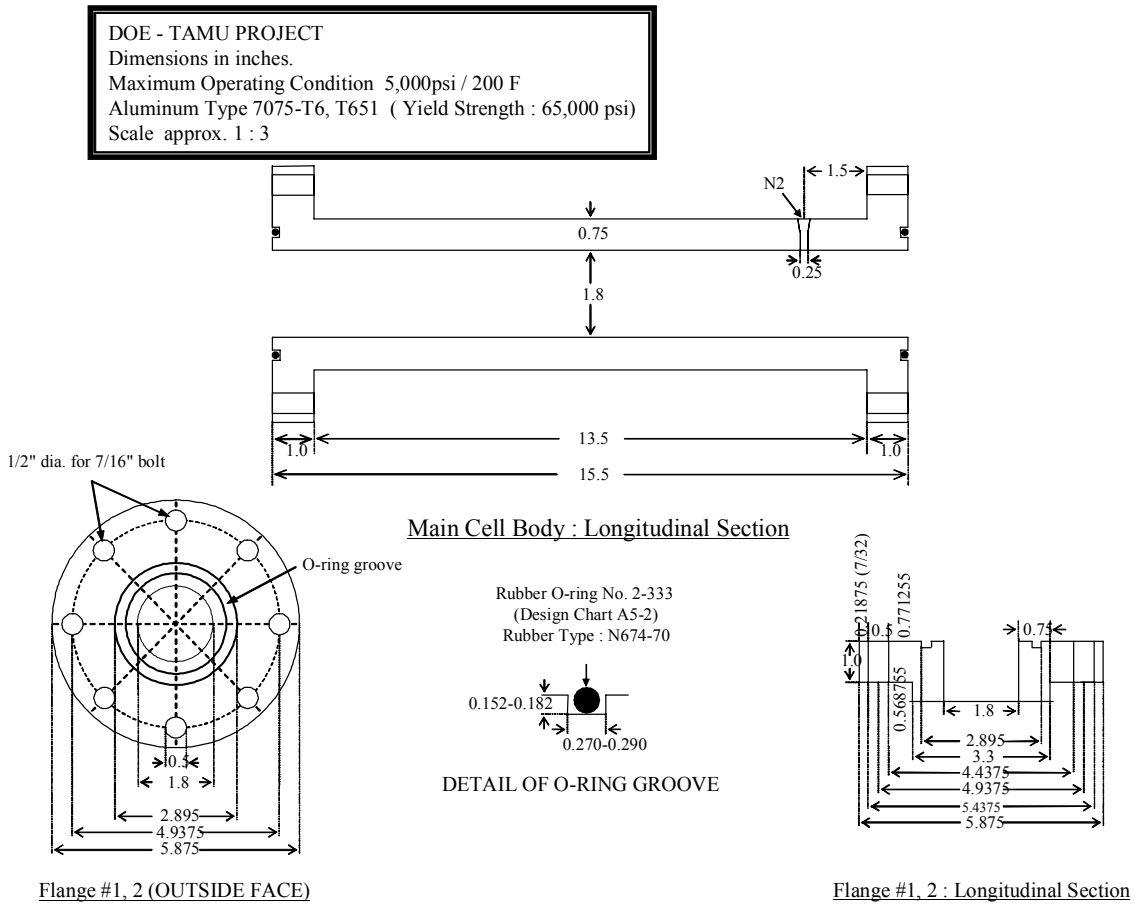

Fig. 5.9 – Cross-section of the core holder.

5.2. Fracture aperture calibration

5.2.1 Experimental procedure

A Picker 4th generation CT scanner was used for imaging the core samples. The power, voltage and algorithm requirements were chosen typical of a sandstone sample. The experimental setup consists of two halves of the same rock sample (Berea Core), feeler gauges and core holding equipment. The two halves were polished thoroughly to reduce surface roughness as much as possible. Smoother surfaces ensure that there is a proper match between the halves and hence smaller fractures can be measured. The feeler gauges were then placed between the two flat surfaces to create a fracture of known size (Fig. 5.10). Feeler gauges of size 38 µm, 51 µm, 64 µm, 76 µm, 102 µm, 127 µm, 152 µm, 178 µm, 508 µm, 813 µm were used in the calibration experiment.

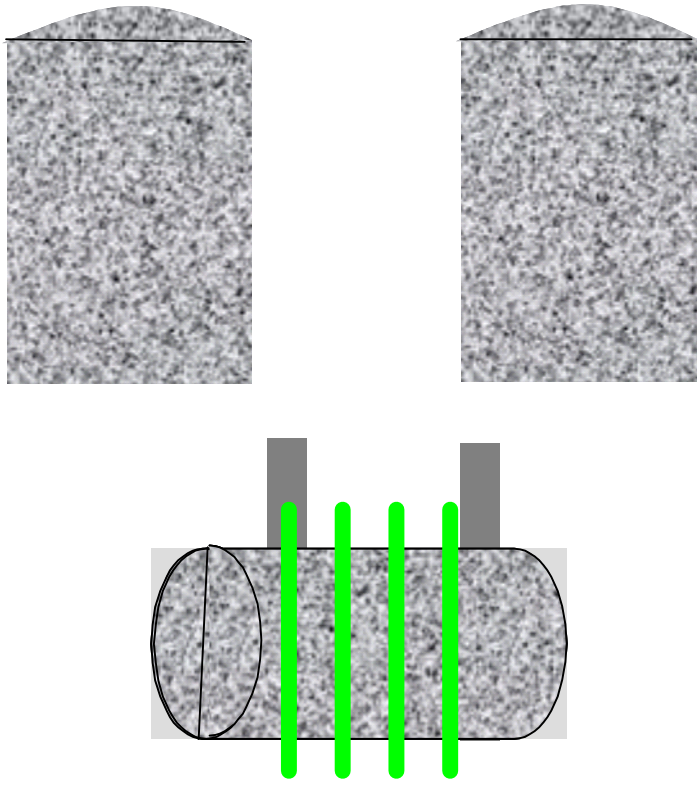

Fig. 5.10 – Experimental procedure showing feeler gauges and scan locations.

The sample with the fracture was inserted into a sleeve to avoid artifact effects and held in the core holder. A pressure of 500 psi was applied using a hydraulic jack. Multiple scans were then taken along the length of the core, perpendicular to the longitudinal axis. Fig. 5.11 shows a typical set of scans for the Berea sample with 38 mm fracture size.

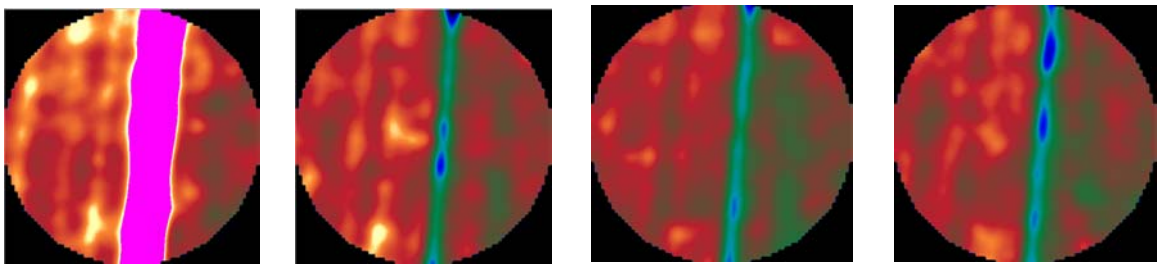

Fig. 5.11 – Scans taken along the length of the core with 38 µm feeler gauge.

The variations in color in the scans are due to different densities in the sample, with the relatively high density steel feeler gauge set to bright pink color, denser rock material set to a bright orange color and the lower densities set to green, blue and black in decreasing order of densities. First scan in Fig. 5.11 is taken through the steel feeler gauge which has higher density than the core material, hence appears lighter in the middle of the core. Two feeler gauges were used on either ends and scans were taken starting from one feeler gauge till the start of the next feeler gauge, with intervals of 5 mm. The actual size of the feeler gauge is much less than it appears in the scan due to artefact effect. The next three scans show a fracture aperture of 38 µm along the length of the core.

Fig. 5.12 shows the CT number variation along the section given. The CT number of the core ranges from 1470 to 1550. The CT number variation for the core material is due to heterogeneity of the rock, however the difference is not appreciable since Berea is not a highly heterogeneous rock. There is a dip in CT numbers in the middle which indicates the location of the fracture region. The CT number in the fracture is close to 1410. This clearly distinguishes fracture from the matrix. Although we can clearly identify the fracture and can measure CT number, this does not give the fracture aperture. So the dip is corresponded to 38 µm fracture aperture. The dip is not abrupt, rather a

smooth transition from matrix to fracture. This effect is due to dispersion of CT numbers, which is caused by finite beam width and oversampling.

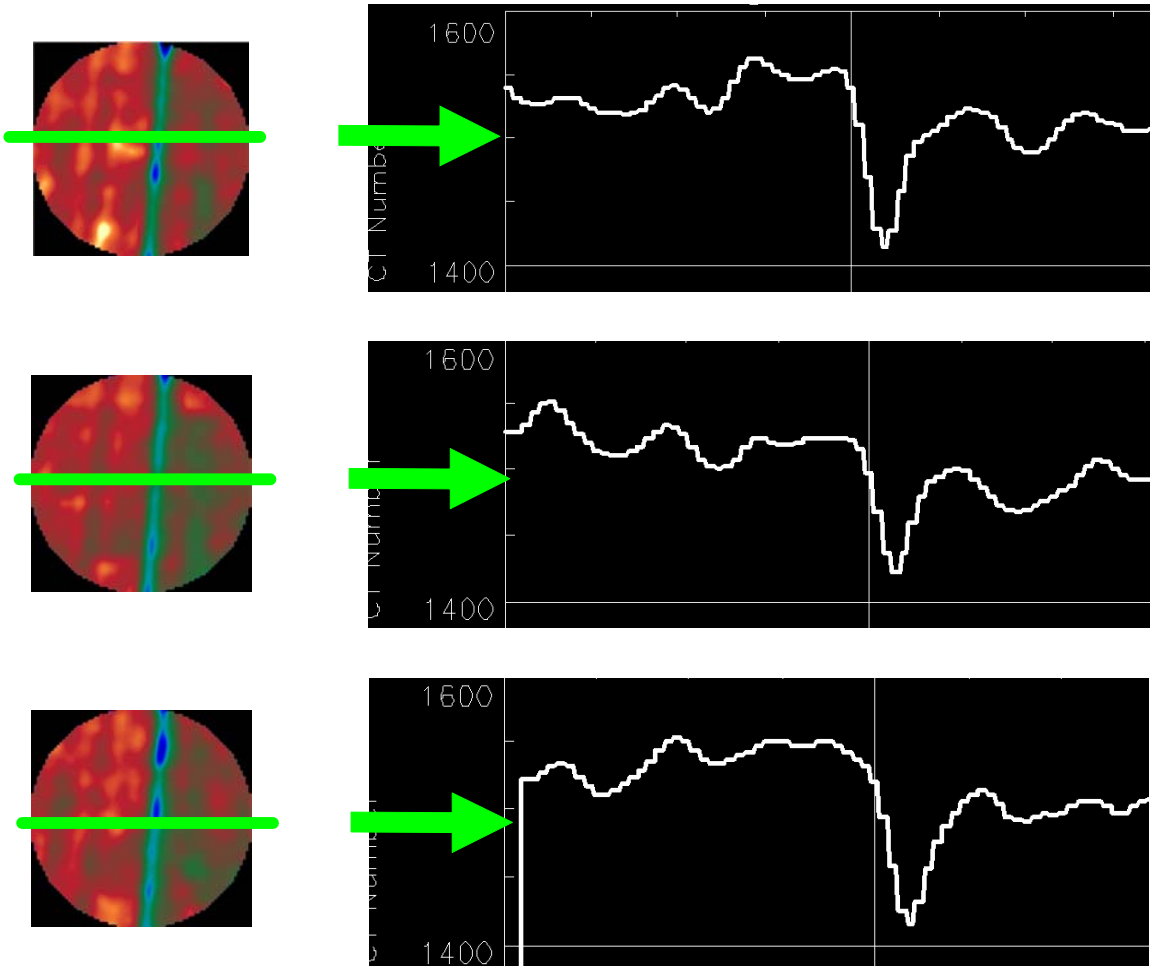

Fig. 5.12 – CT number variation along the section.

Fig. 5.13 shows the fracture aperture size of 51 µm, along the length of the core. As the increment in fracture aperture size is small, there is no much appreciable difference between Figs. 5.11 and 5.13.

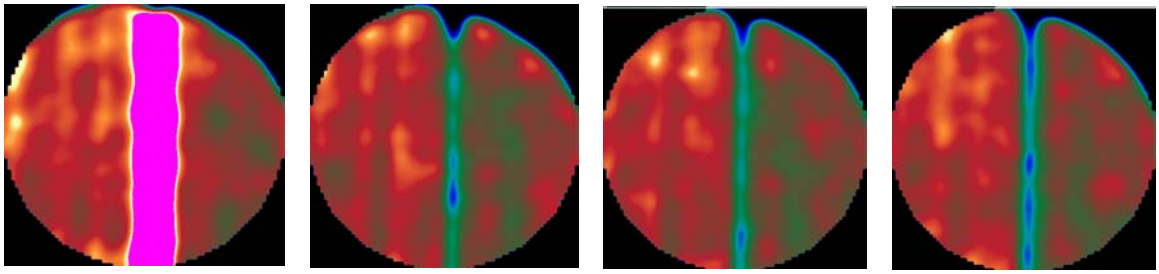

Fig. 5.13 – Scans taken along the length of the core with 51 µm feeler gauge.

Fig. 5.14 shows the CT number variation along the section for 51 µm aperture size. The CT number in the fracture goes below 1400, compared to 1410 in Fig. 5.12 for 38 µm aperture size.

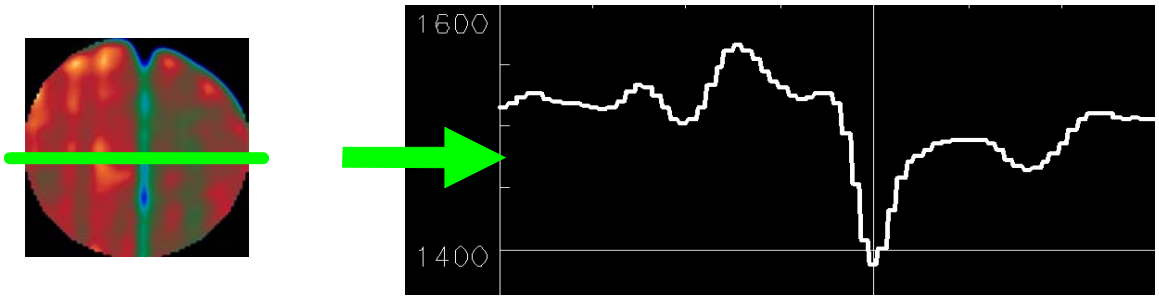

Fig. 5.14 – Variation of CT numbers along the section.

Sample scans for various aperture sizes are shown in Figs. 5.15 to 5.17. They display aperture sizes of 64 µm, 76 µm, and 102 µm. We can clearly see that, as the aperture size increases, the fracture can be clearly seen in the middle of the core, with darker color.

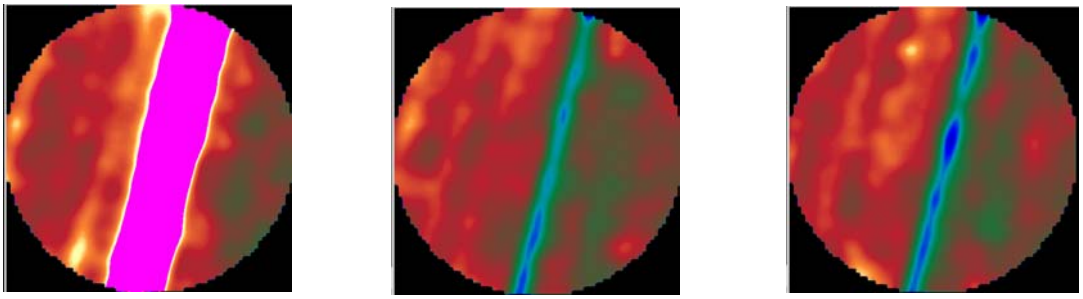

Fig. 5.15 – Scans taken along the length of the core with 64 µm feeler gauge.

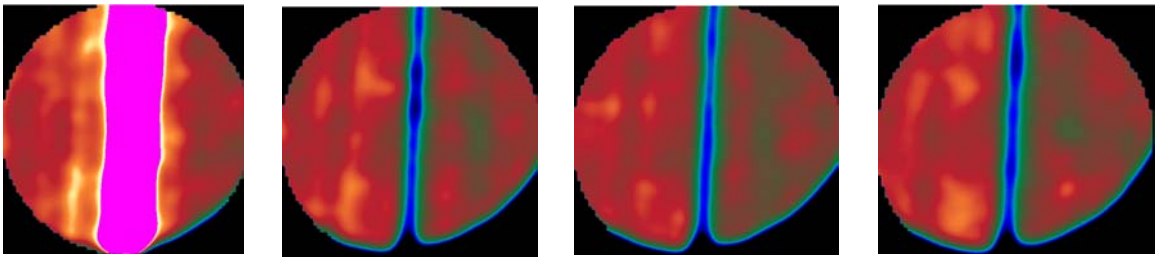

Fig. 5.16 – Scans taken along the length of the core with 76 µm feeler gauge.

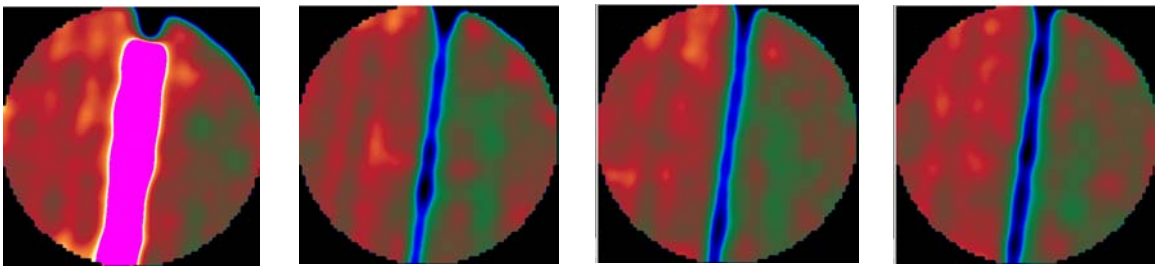

Fig. 5.17 – Scans taken along the length of the core with 102 µm feeler gauge.

5.2.2 Calibration technique

The CT number for a typical Berea sample is about 1600 and that of air is about -1000. As mentioned earlier, the variations in CT numbers are due to the difference in densities. One would normally expect the CT number at the fracture to be the same as that of air. But this does not happen due to the fact that the CT number at the fracture is influenced by the presence of the rock material around it, a condition termed "oversampling". A plot of CT number versus the pixel number was made with the CT numbers obtained from each scan. Using these, an average CT number plot was obtained to account for minor variations in fracture sizes caused by surface roughness. An example of such a plot is shown in Fig. 5.18.

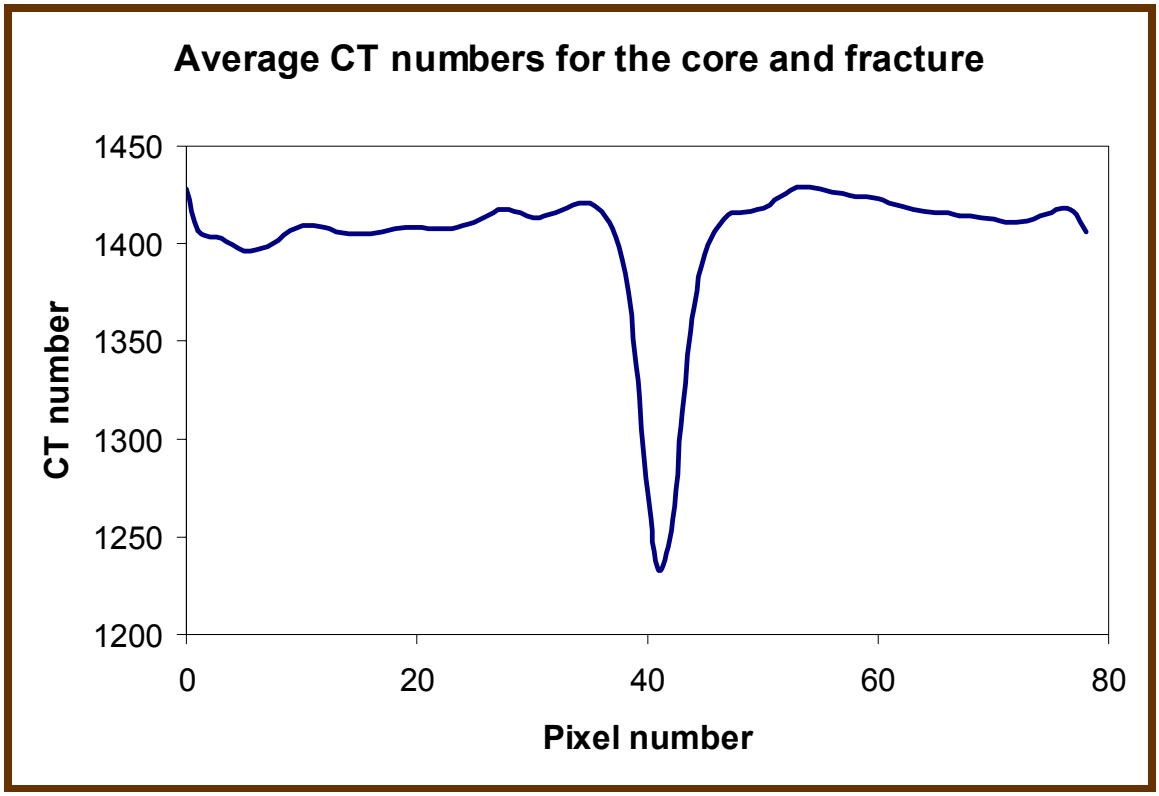

Fig. 5.18 – Average CT number plot.

From the plot, a threshold CT number was identified, which essentially is the minimum rock CT number (Fig. 5.19).

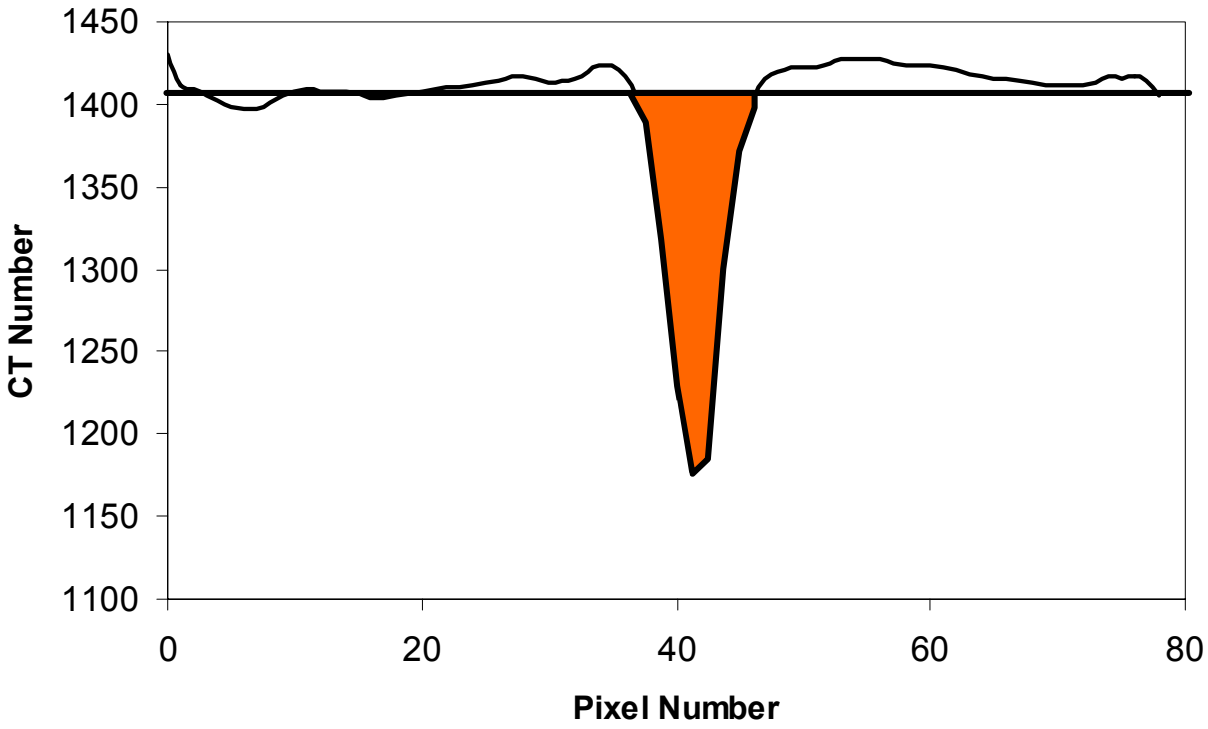

Fig. 5.19 – Plot with shaded area representing fracture.

Fig. 5.20 shows a comparison of the average CT number curves obtained for various fracture sizes. As we can see from the Fig. 5.20, the dip is more for larger aperture sizes. Also the transition region is wide when the aperture size increases.

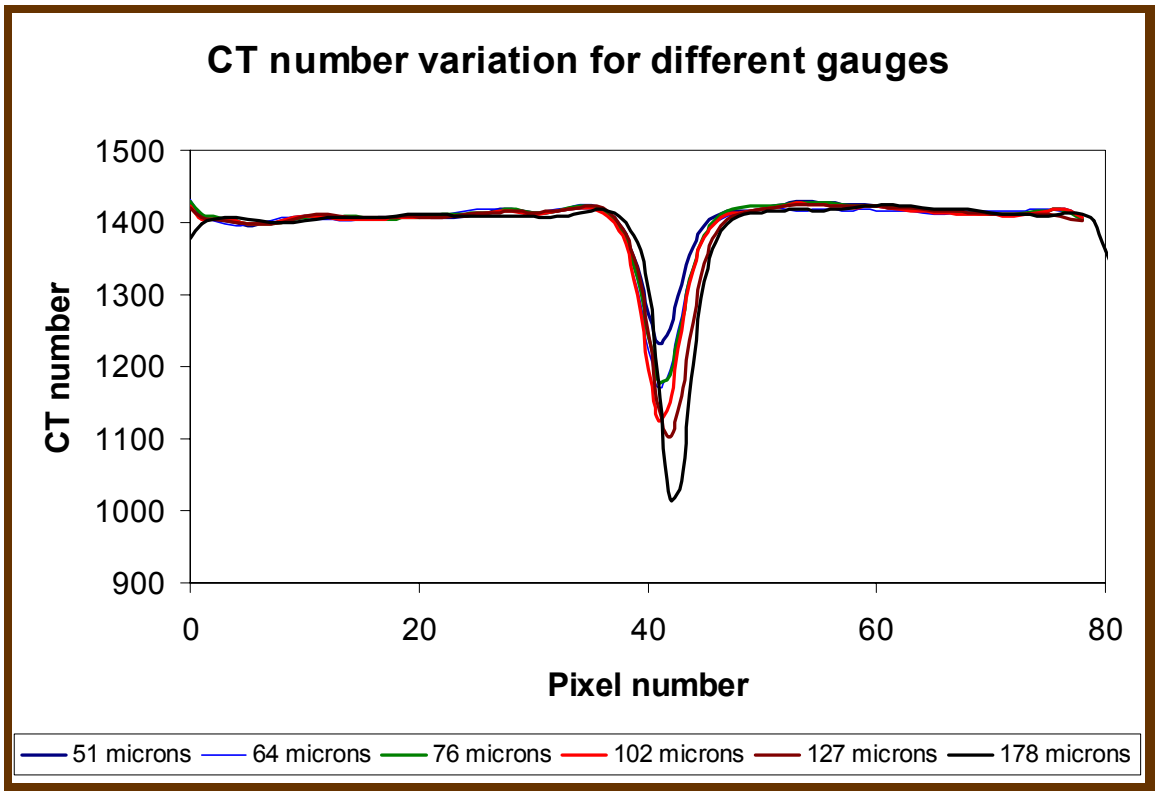

Fig. 5.20 – Comparison of CT number plots for different fracture sizes.

All the CT numbers in the area below the minimum rock CT number are subtracted from the Rock CT number and the differences are used to obtain the integrated CT signal for that fracture size. The integrated CT signals are calculated for each pixel number and are given an index starting from 1 to n as shown in Fig. 5.21. Area of the integrated CT region is calculated from the following formula.

For index equal to 1, $Area_1 = \frac{1}{2} \times IntCT_1$

$$Area_2 = IntCT_1 + \frac{1}{2} \times (IntCT_2 - IntCT_1)$$

.

$$Area_{c+1} = IntCT_{c+1} + \frac{1}{2} \times (IntCT_c - IntCT_{c+1})$$

.

$$Area_n = \frac{1}{2} \times IntCT_n \quad \text{..... (28)}$$

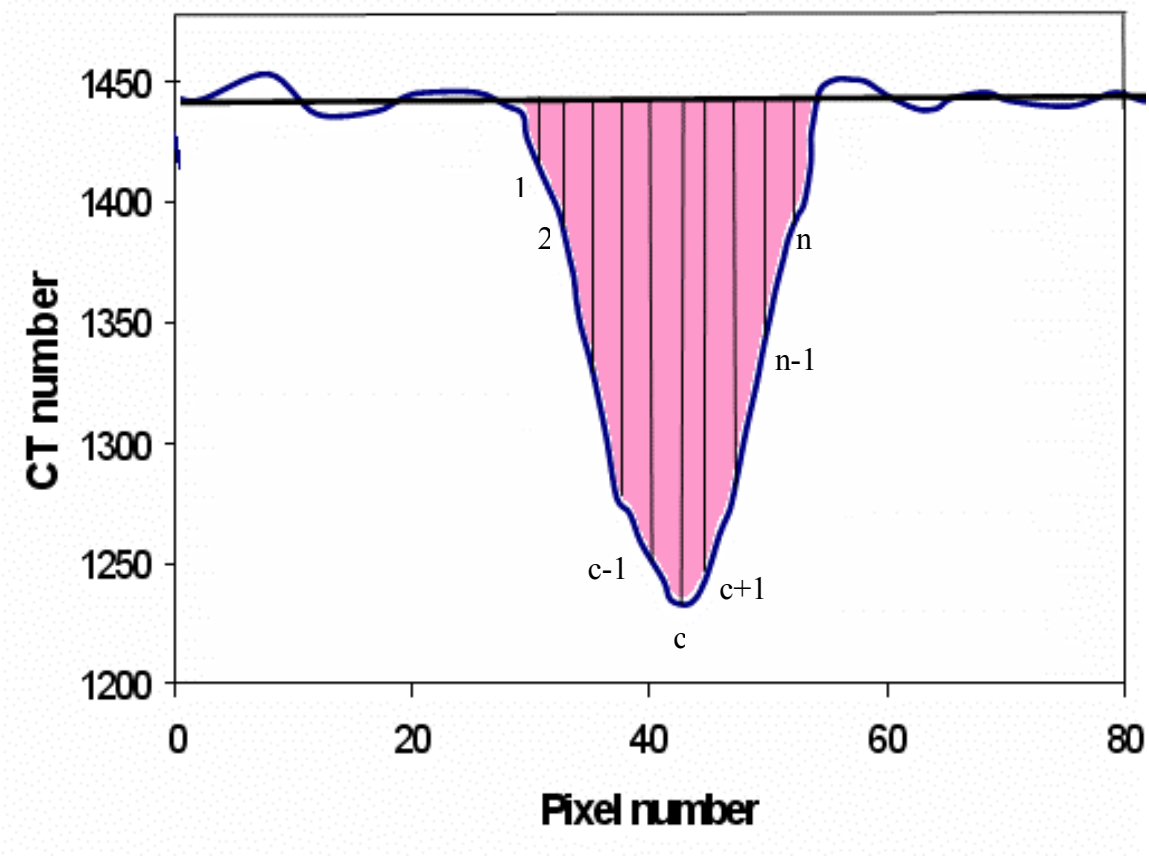

Fig. 5.21 – Integrated area in the fracture region showing index of integrated CT signal.

The plot of integrated CT signal vs. aperture size is the calibration curve for that sample (Fig. 5.22 and Fig. 5.23). There is a linear relationship between the integrated CT signal and fracture aperture as can be seen in Fig. 5.22. The variance of each integrated CT signal is 25. The linear relationship still follows even in the smaller fracture aperture region as can be seen in Fig. 5.23. Given a fractured sample, the CT scanner can be used to obtain the integrated CT signal and the fracture size can be determined using the calibration curve. The equation obtained from calibration curve is $y = 8.7616x + 460.7$, where y is the integrated CT signal and x is the fracture aperture in microns. By rearranging the equation we get, $x = 0.1141y - 52.582$, from which we can calculate fracture aperture, if the integrated CT signal is known.

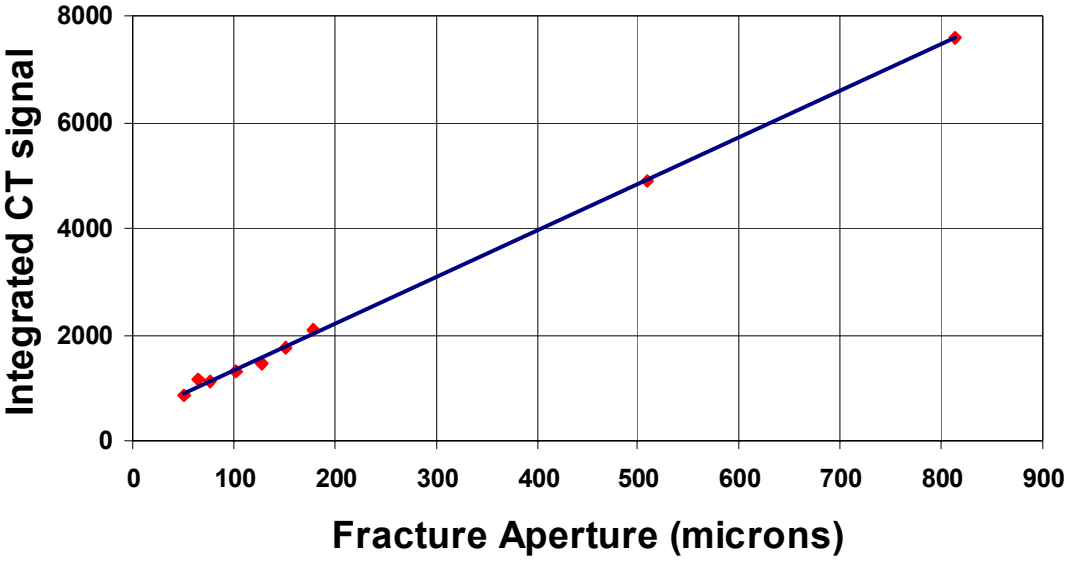

Fig. 5.22 – Calibration curve between integrated CT signal and fracture aperture.

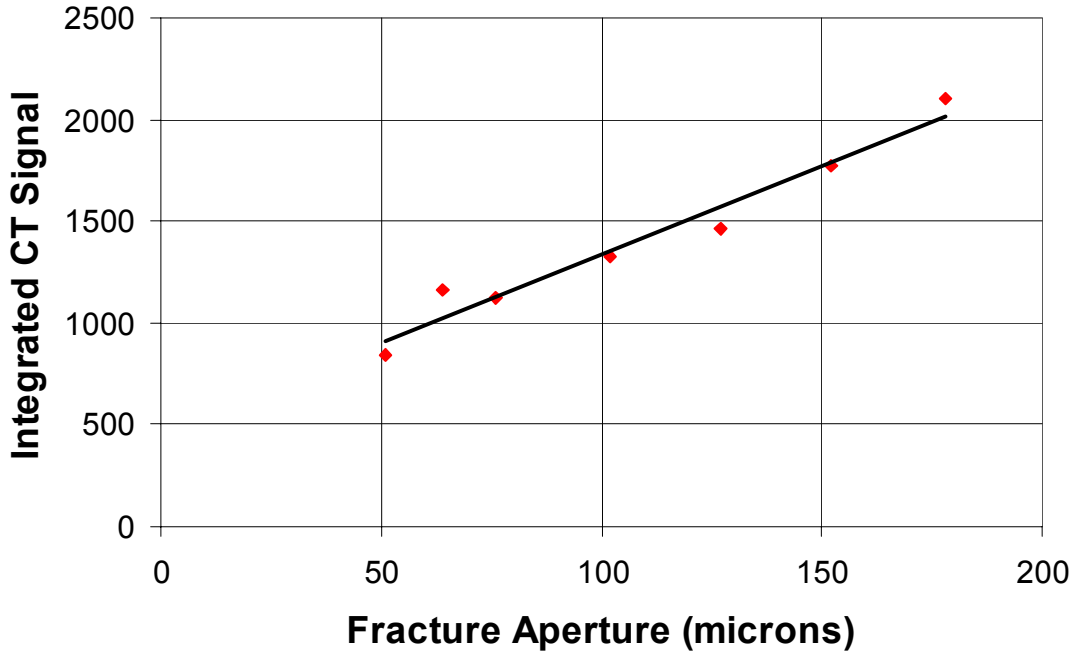

Fig. 5.23 – Calibration curve depicts linear trend at small fracture apertures.

5.3. Fracture aperture distribution

5.3.1 Experimental procedure

For the sake of simplicity, Berea core was used to conduct the experiment. A 1 inch diameter by 2.36 inch length core was used. The core was fractured mechanically in the laboratory using hydraulic cutter as shown in Fig.5.24.

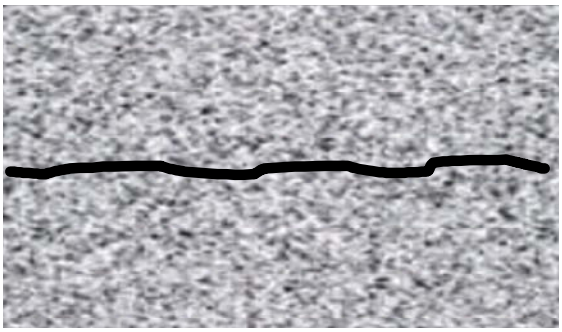

Fig. 5.24 – Berea core with fracture in the central plane.

The fractured core was then imaged in the X-ray CT scanner. Images were taken every 1 mm up to 60 mm along the length of the core. The core was then subjected to overburden pressure of 500 psi and again the scans were taken at the same locations. The same procedure was repeated for various overburden pressures of 1000 psi and 1500 psi.

5.3.2 Image transfer

The images obtained from X-ray CT scanner were transferred to VOXELCALC, a software for reading the X-ray data, to obtain CT number in each pixel. A comparison of the CT number can be made for any row and column across the core as shown in Figs. 5.25 and 5.26. Figs. 5.27 to 5.30 show the images taken with and without overburden pressures.

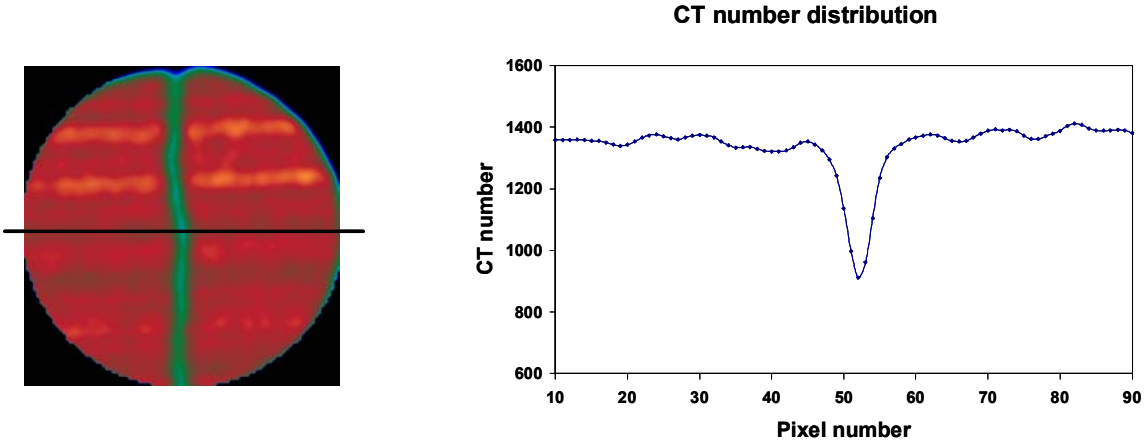

Fig.5.25 –Distribution of CT number along the row showing a dip for the fracture.

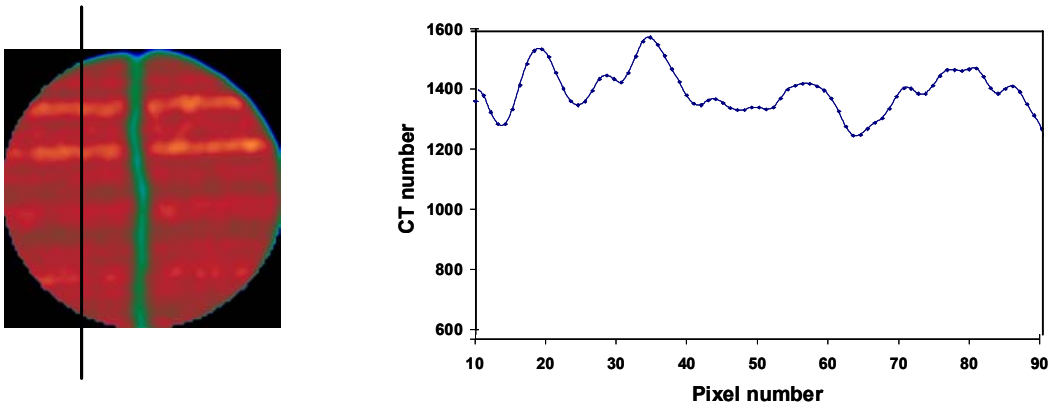

Fig. 5.26 – Distribution of CT number along the column showing the heterogeneity.

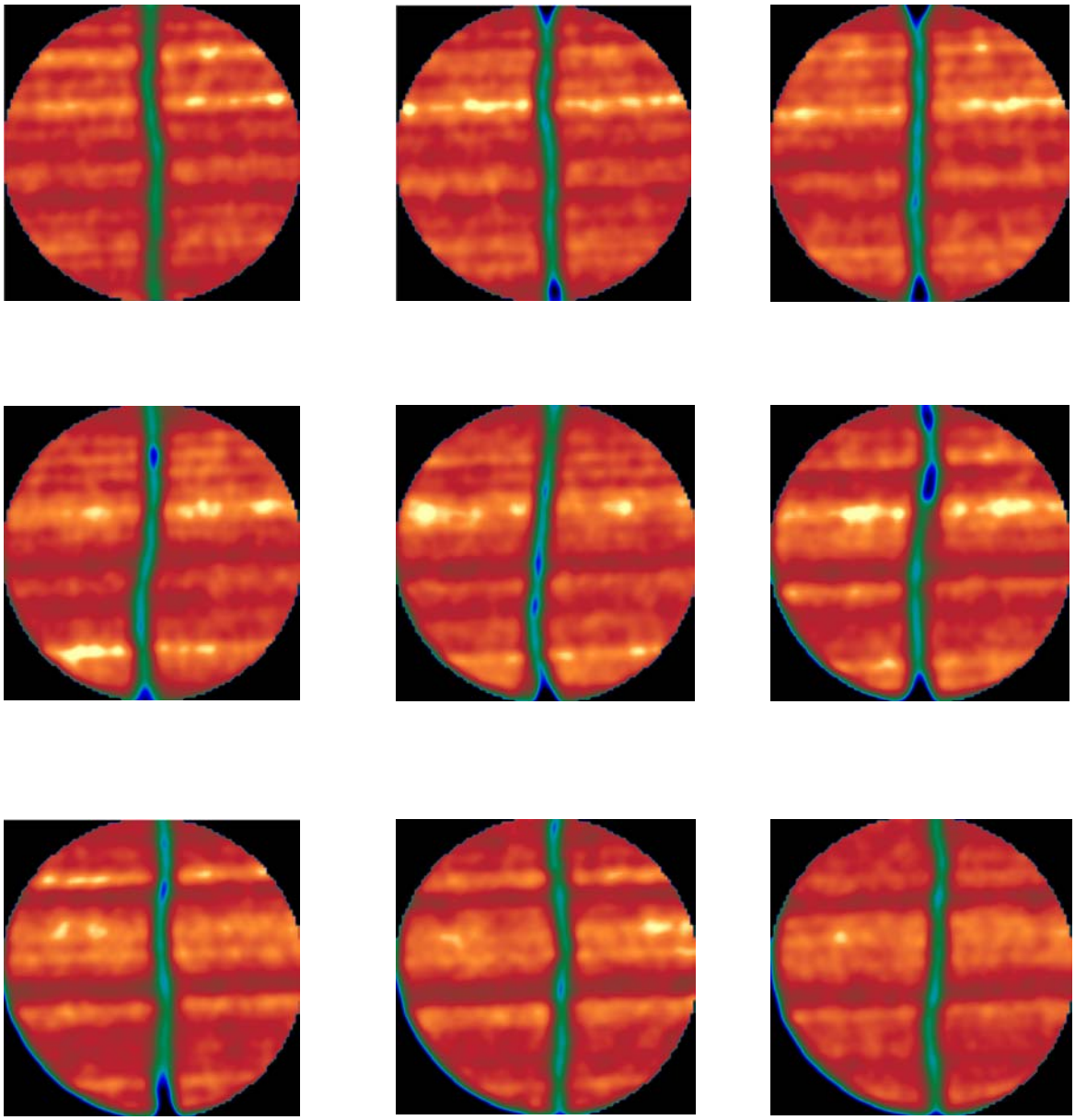

Fig. 5.27 – Sample scans taken along the length of the core without overburden pressure.

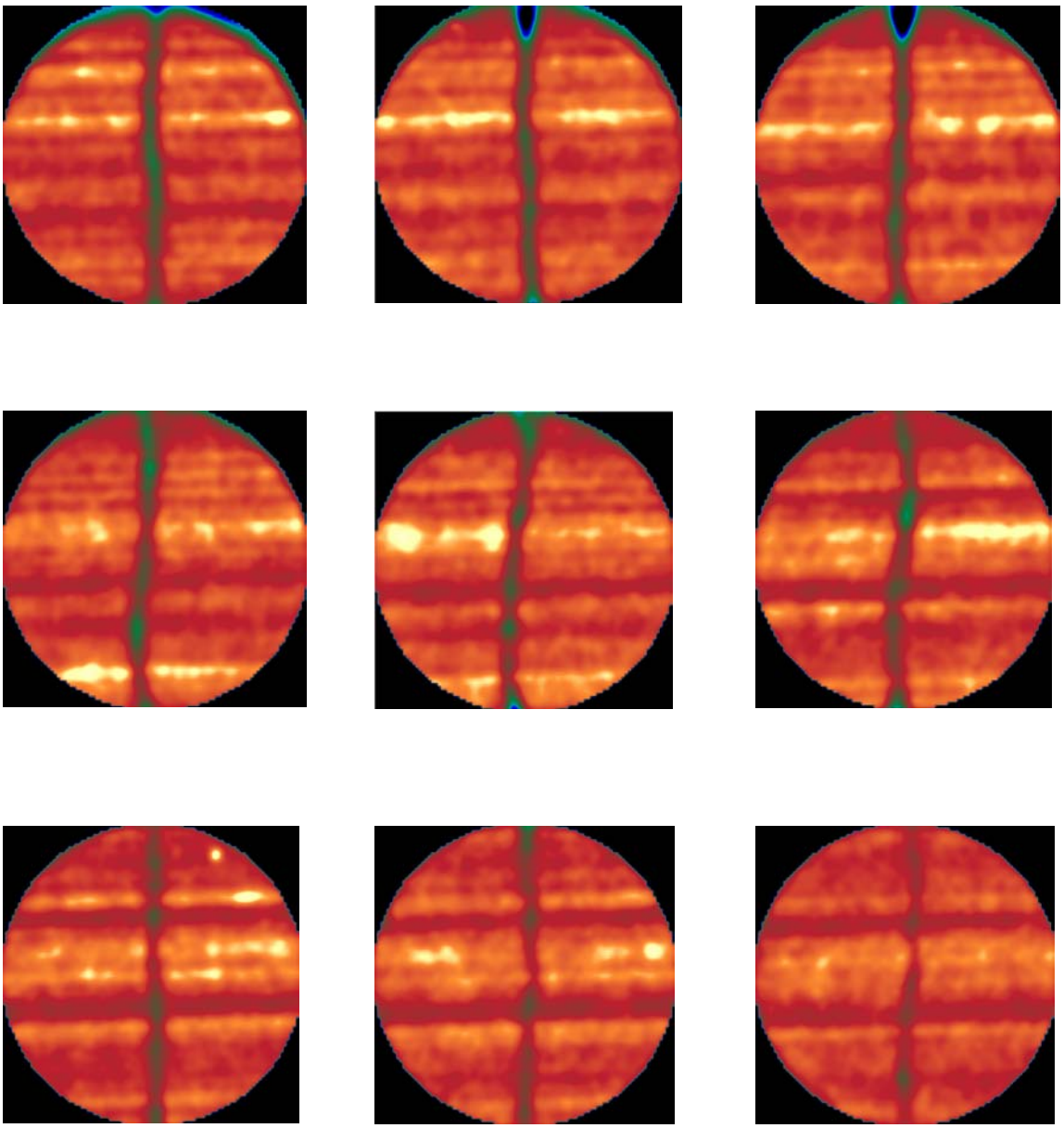

Fig. 5.28 – Sample scans taken along the length of the core with 500 psi overburden pressure.

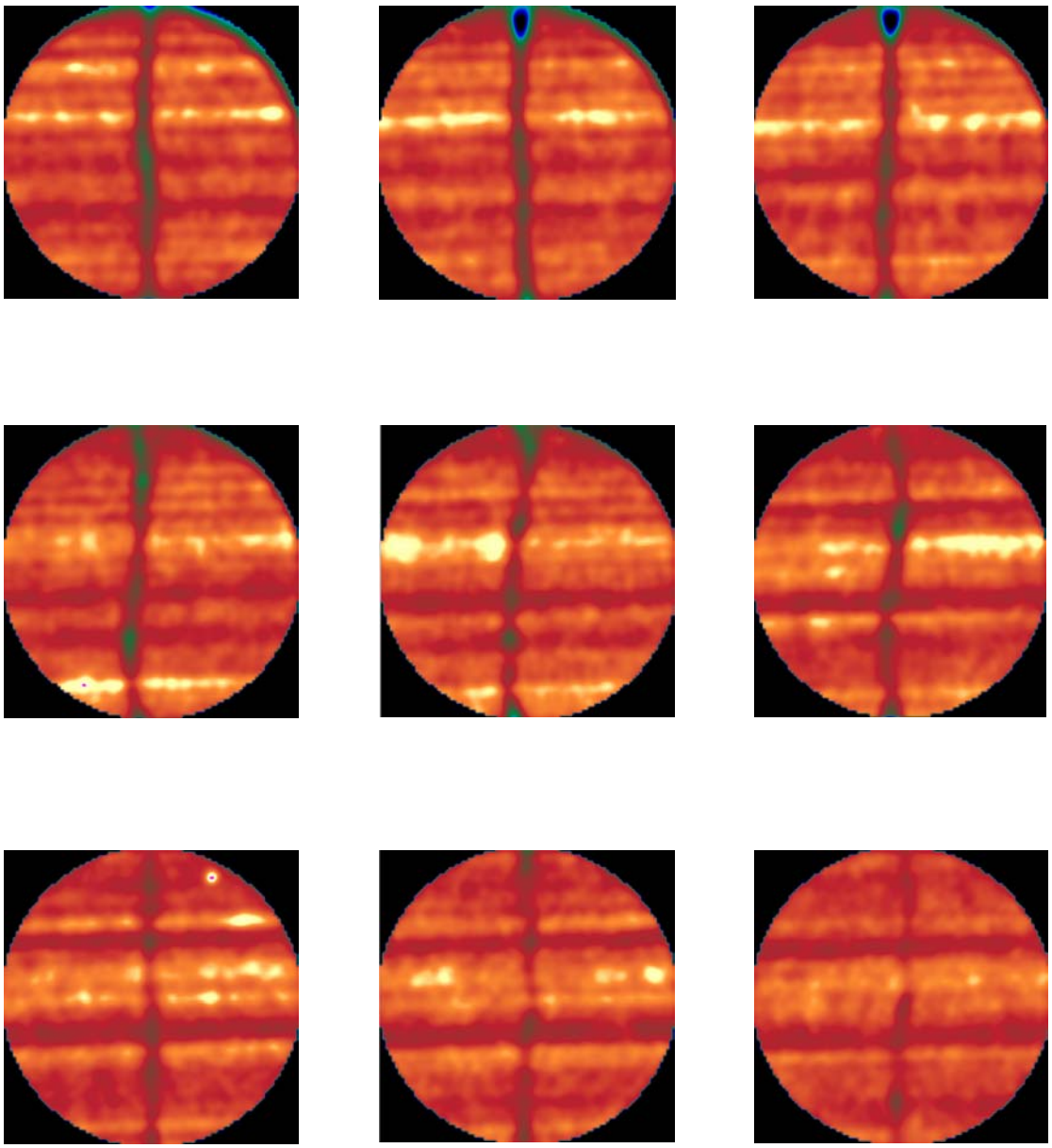

Fig. 5.29 – Sample scans taken along the length of the core with 1000 psi overburden pressure.

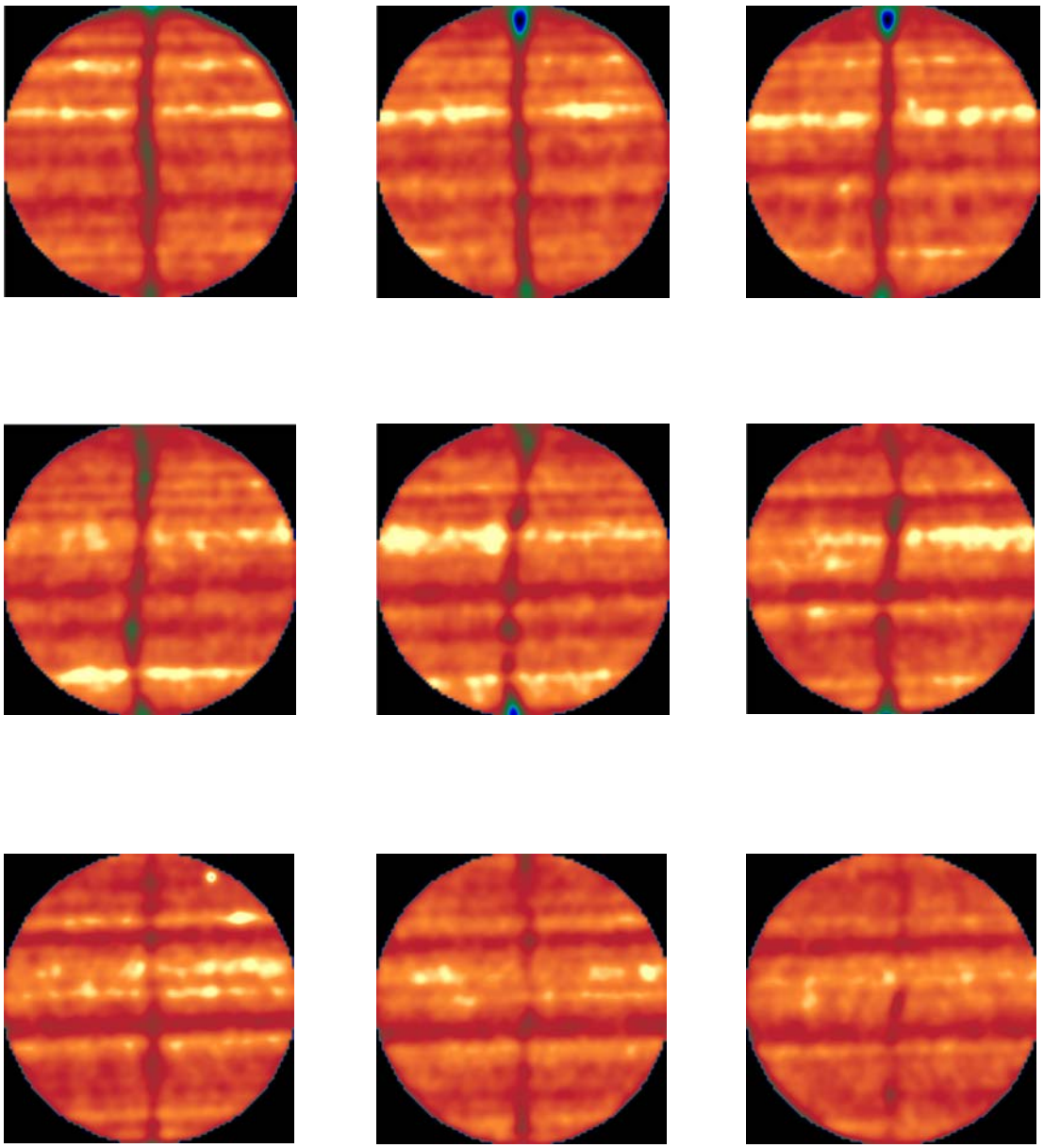

Fig. 5.30 – Sample scans taken along the length of the core with 1500 psi overburden pressure.

5.3.3 Data preparation

About 6000 data points were taken for each overburden condition. The aperture values from the CT data were obtained by the calibration curve as discussed in the previous section.

5.3.4 Data distribution

Mean, variance, and standard deviation were obtained for the dataset. The dataset was then plotted. Table.5.1 shows the range and frequencies of the apertures with and without overburden pressure. The mean, variation and standard deviation for the data are given in Table. 5.2.

Table. 5.1 – Dataset showing range and frequency for various overburden pressure conditions.

No Overburden Pressure		500 Psi Overburden pr.		1000 Psi Overburden		1500 Psi Overburden	
Range	Count	Range	Count	Range	Count	Range	Count
0 - 100	68	0 - 100	1508	0 - 100	2558	0 - 100	2892
100 - 200	353	100 - 200	2393	100 - 200	1999	100 - 200	1890
200 - 300	2139	200 - 300	1287	200 - 300	812	200 - 300	684
300 - 400	2119	300 - 400	368	300 - 400	261	300 - 400	193
400 - 500	832	400 - 500	176	400 - 500	125	400 - 500	109
500 - 600	226	500 - 600	102	500 - 600	85	500 - 600	84
600 - 700	134	600 - 700	79	600 - 700	56	600 - 700	63
700 - 800	85	700 - 800	38	700 - 800	59	700 - 800	36
800 - 900	61	800 - 900	43	800 - 900	54	800 - 900	38
900 - 1000	34	900 - 1000	25	900 - 1000	29	900 - 1000	16
1000 - 1100	27	1000 - 1100	33	1000 - 1100	8	1000 - 1100	4
1100 - 1200	22	1100 - 1200	15	1100 - 1200	1	1100 - 1200	0
1200 - 1300	25	1200 - 1300	4	1200 - 1300	0	1200 - 1300	1
1300 - 1400	19	1300 - 1400	3	1300 - 1400	0	1300 - 1400	0
1400 - 1500	13	1400 - 1500	0	1400 - 1500	0	1400 - 1500	0
1500 - 1600	16	1500 - 1600	0	1500 - 1600	0	1500 - 1600	0
1600 - 1700	7	1600 - 1700	0	1600 - 1700	0	1600 - 1700	0
1700 - 1800	6	1700 - 1800	0	1700 - 1800	0	1700 - 1800	0
1800 - 1900	14	1800 - 1900	0	1800 - 1900	0	1800 - 1900	0
1900 - 2000	5	1900 - 2000	0	1900 - 2000	0	1900 - 2000	0
2000 - 2100	0	2000 - 2100	0	2000 - 2100	0	2000 - 2100	0
2100 - 2200	1	2100 - 2200	0	2100 - 2200	0	2100 - 2200	0

Table. 5.2 – Statistical parameters for different overburden conditions.

	No_overburden	500_overburden	1000_overburden	1500_overburden
Mean	370.5273743	197.9978943	157.4180145	138.6561127
Variance	44847.62887	29781.35105	26372.14946	22599.10453
Std_deviation	211.7725876	172.5727413	162.3950414	150.3299855

Probability distribution was calculated for each condition and is plotted against the fracture apertures as shown in Fig. 5.31 to 5.34. A comparative study was made for different overburden pressures and the result is plotted in Fig. 5.35.

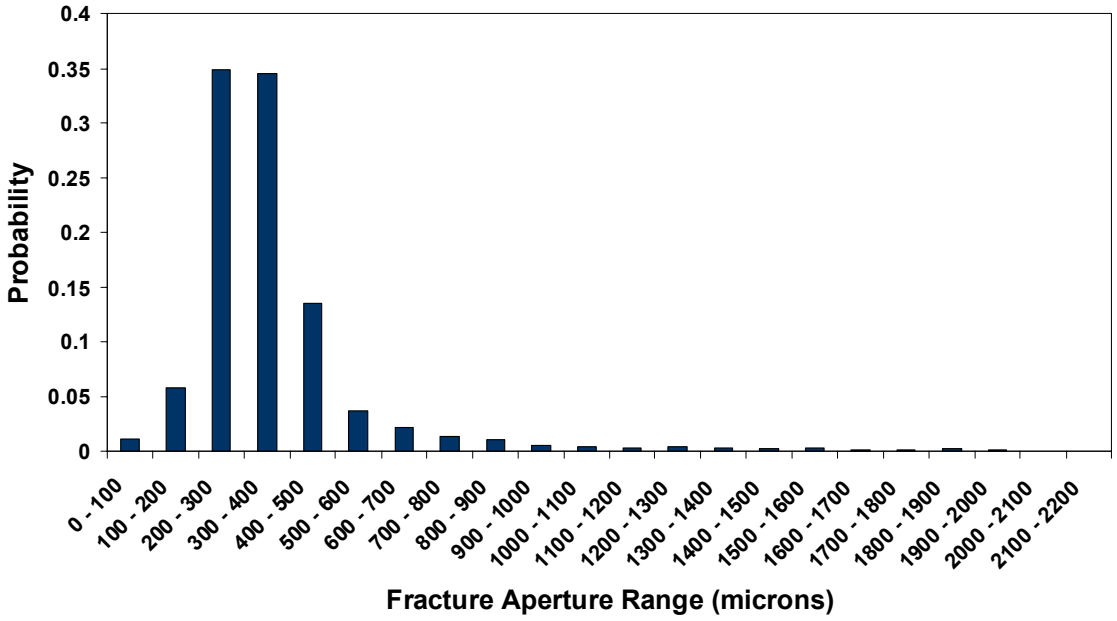

Fig. 5.31 – Probability distribution of fracture apertures without overburden pressure.

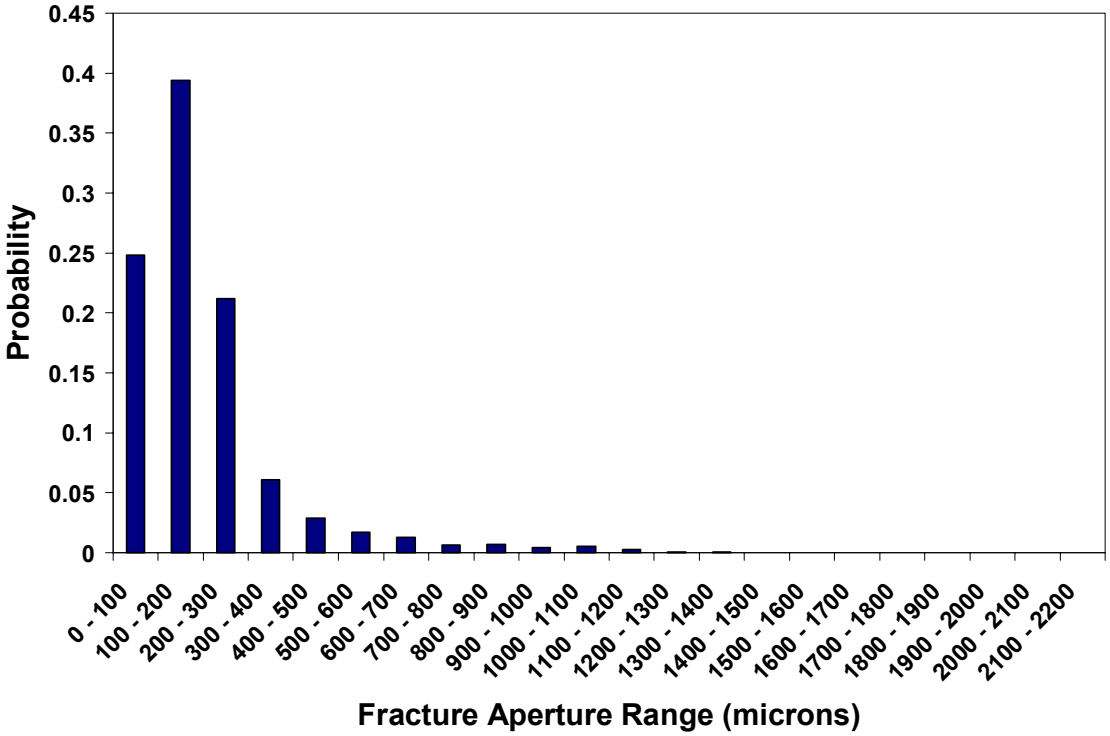

Fig. 5.32 – Probability distribution of fracture apertures at 500 psi overburden pressure.

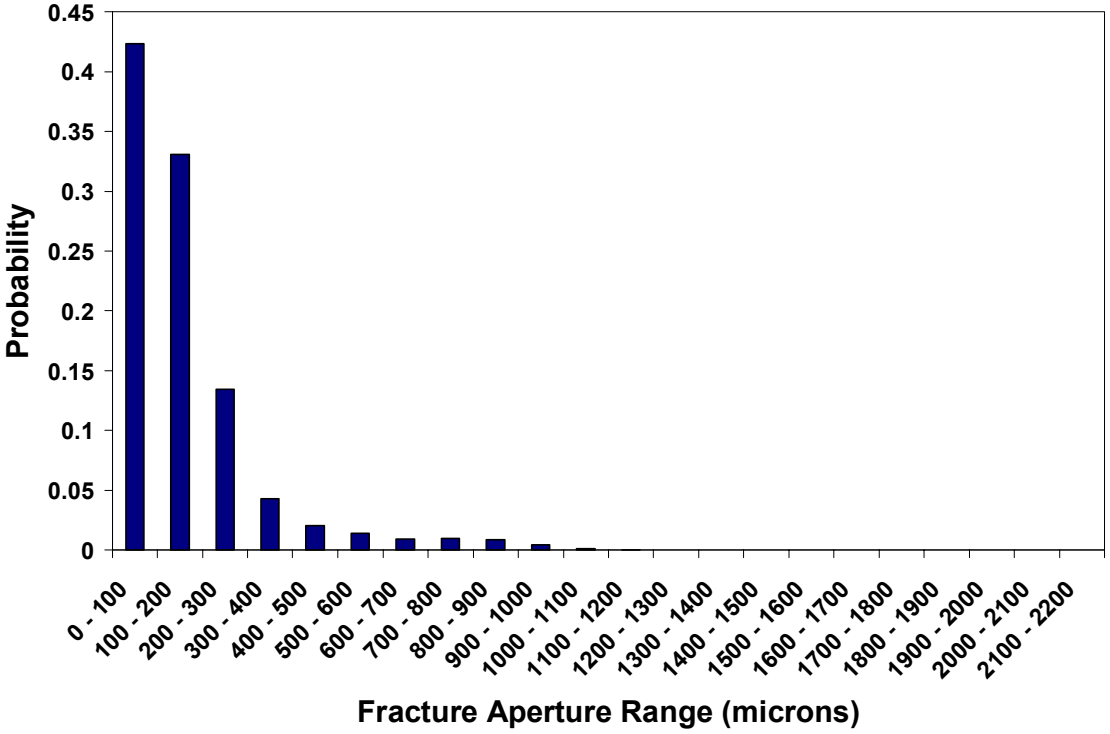

Fig. 5.33 – Probability distribution of fracture apertures at 1000 psi overburden pressure.

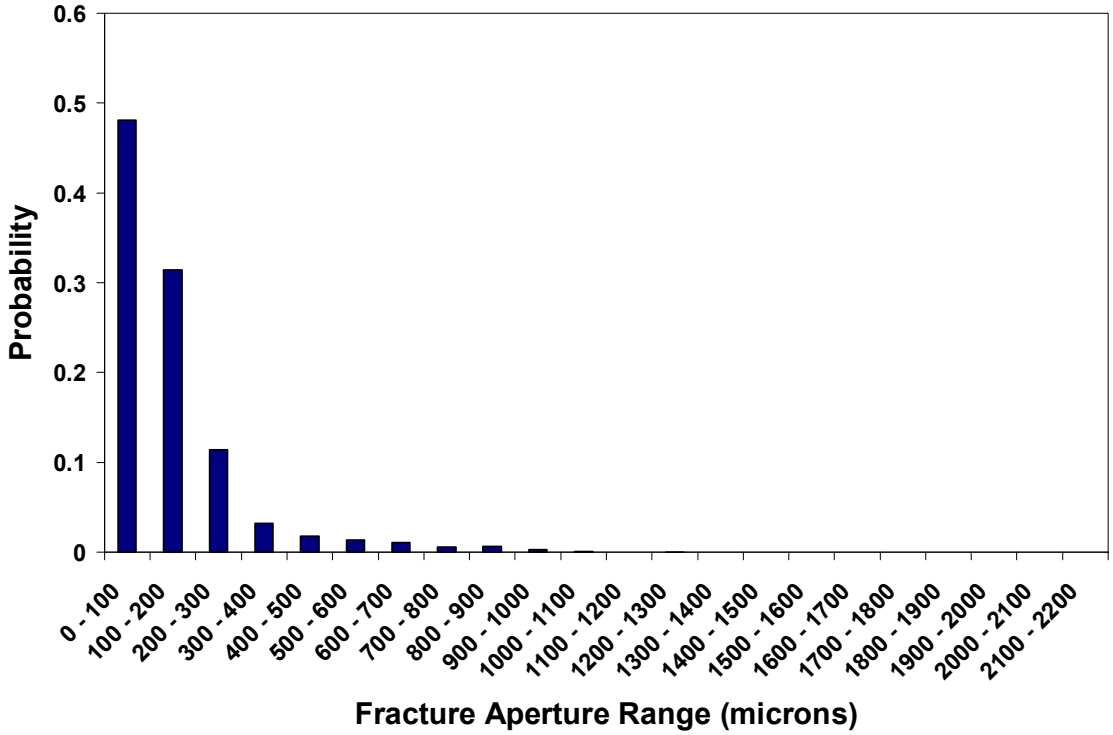

Fig. 5.34 – Probability distribution of fracture apertures at 1500 psi overburden pressure.

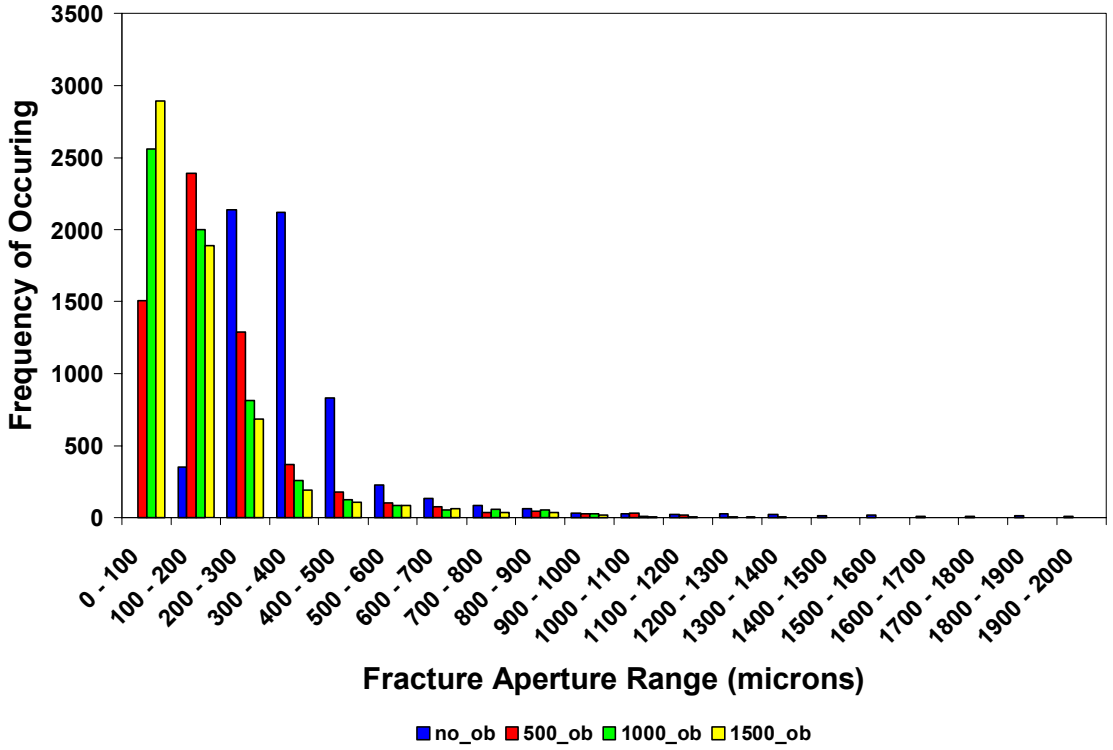

Fig. 5.35 – Comparitive study of fracture aperture distribution under various overburden pressures.

5.3.5 Discussion

The apertures are distributed in the range of 0 to 2200 microns, with probable apertures in the range of 100 to 500 microns as shown in Fig. 5.31. The tail of the aperture distribution is long and the aperture distribution is right skewed which suggests that the distribution might follow either gamma or lognormal distribution as given in the earlier studies (Gentier[44], Tsang and Tsang[12], and Keller[31]). The tail of the apertures controls the fluid flow as fluid will tend to flow through preferred channels of least resistance (Alfred[10]). Permeability measurements will be largely controlled by small apertures, which in this case is in the range of 100 to 500 microns. The flow rate calculated from this measured permeability will be different due to the presence of some big apertures in the range of 1000 to 2000 microns. Such big apertures, if interconnected may result in larger flow rate than what was calculated. The probability of finding an aperture in 100 to 500 microns is 0.887. There is still 12% chance that the big apertures might be interconnected. The observed result is plotted in Fig. 5.31. The calculated fracture aperture values when distributed followed lognormal distribution (Fig. 5.36), with mean aperture value of 370.53 microns and variance of 44847. The most probable aperture value, calculated from lognormal distribution is 326.783 microns. The most probable aperture is lesser than mean aperture value due to the large variance of the aperture values. Higher the variance, the more skewed the distribution becomes. The observed result matches closely with the lognormal distribution as shown in Fig. 5.37.

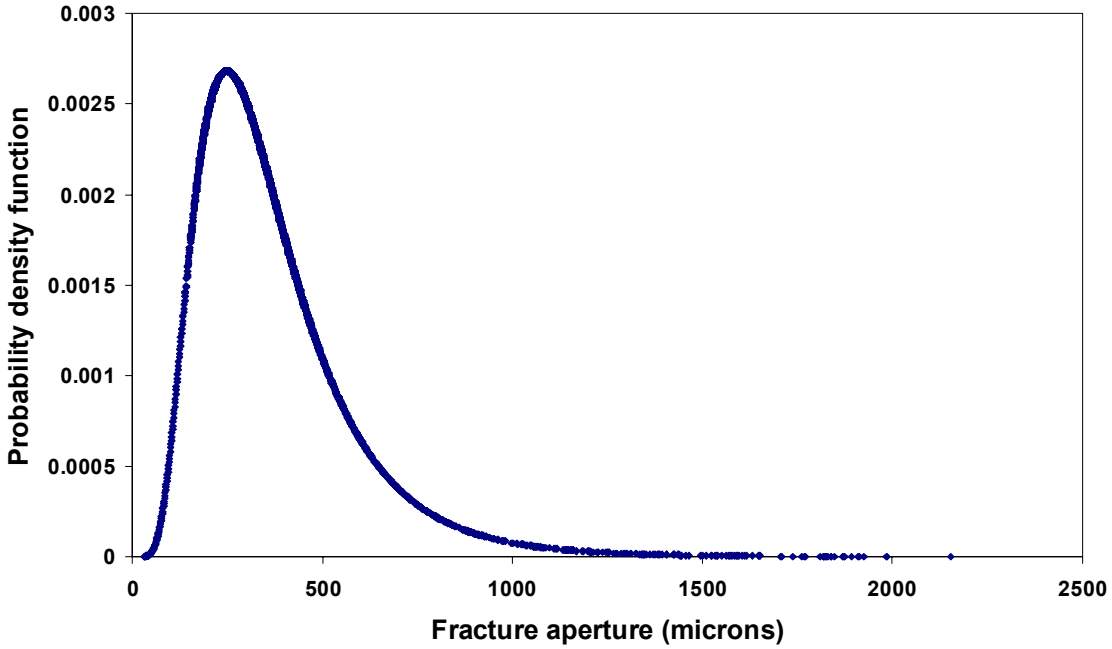

Fig. 5.36 – Lognormal distribution of fracture apertures without overburden pressure.

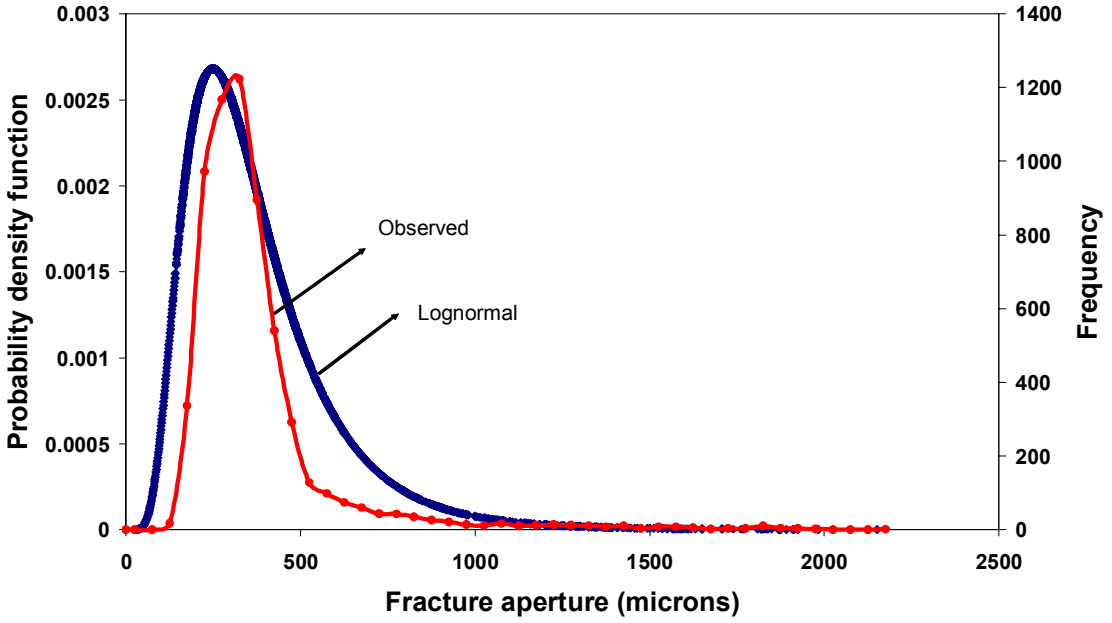

Fig. 5.37 – Comparison of observed and lognormal distribution of fracture apertures without overburden pressure.

Upon increasing the overburden pressure, the mean of the apertures shifts to a lower value (Figs. 5.32 to 5.34), which suggests that the permeability has decreased due to applied overburden pressure. The decrease of the mean apertures is drastic when an initial overburden pressure of 500 psi was applied. The mean of the apertures becomes 197.997 microns from 370.53 microns as shown in Table. 5.2. The fracture surfaces are rough and have many contact points along the path. If the apertures are more, the contact points become weak and tend to breakdown upon applying the stress. The decrease is not significant upon further increase in overburden pressures. The observed results for different overburden pressures are plotted in Figs. 5.32 to 5.34. Lognormal distributions are obtained by using the mean and variance value in the lognormal probability density function using the calculated apertures (Figs. 5.37 to 5.39). Comparison of observed results with lognormal distribution (Figs. 5.40 to 5.42) shows that the difference is very small, which proves that the data follows lognormal distribution for different overburden pressures. A comparison of lognormal distribution was made for fracture apertures at different overburden pressures (Fig. 5.43). Since most of the reservoirs experience overburden pressures, this research will be important to identify some of the uncertainties in fluid flow through fractured reservoirs.

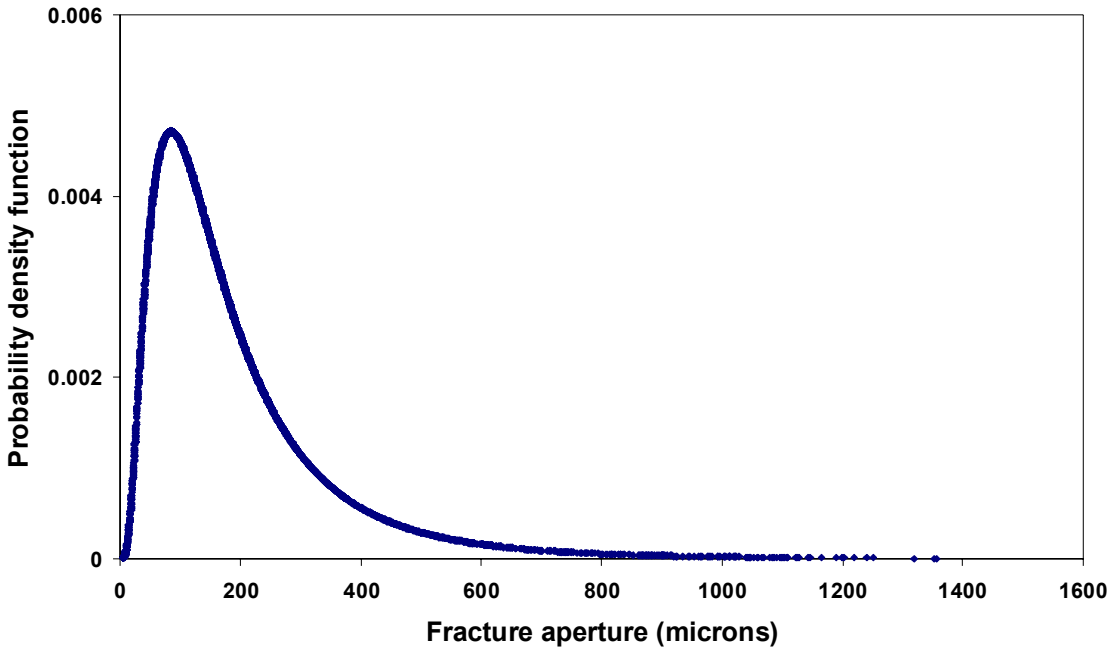

Fig. 5.38 – Lognormal distribution of fracture apertures at 500 psi overburden pressure.

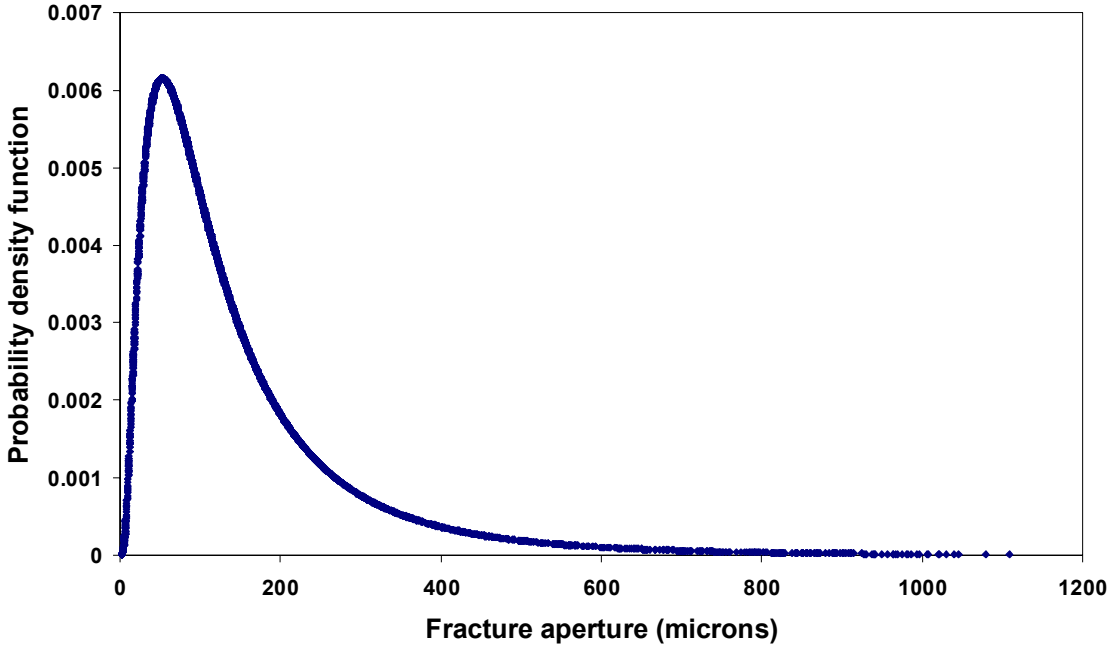

Fig. 5.39 – Lognormal distribution of fracture apertures at 1000 psi overburden pressure.

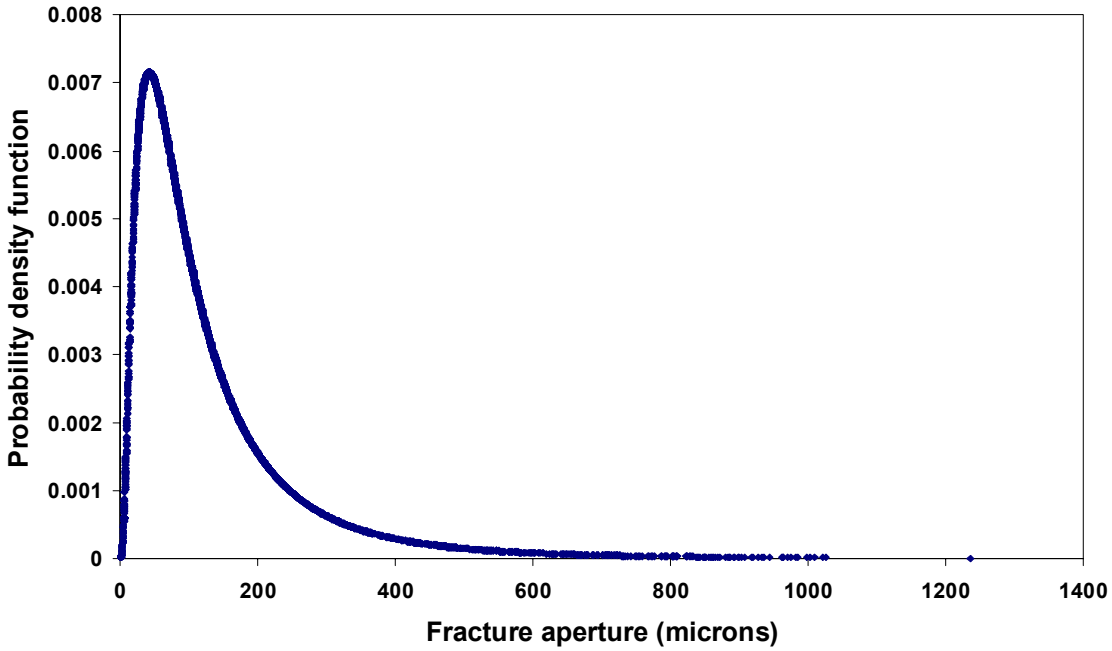

Fig. 5.40 – Lognormal distribution of fracture apertures at 1500 psi overburden pressure.

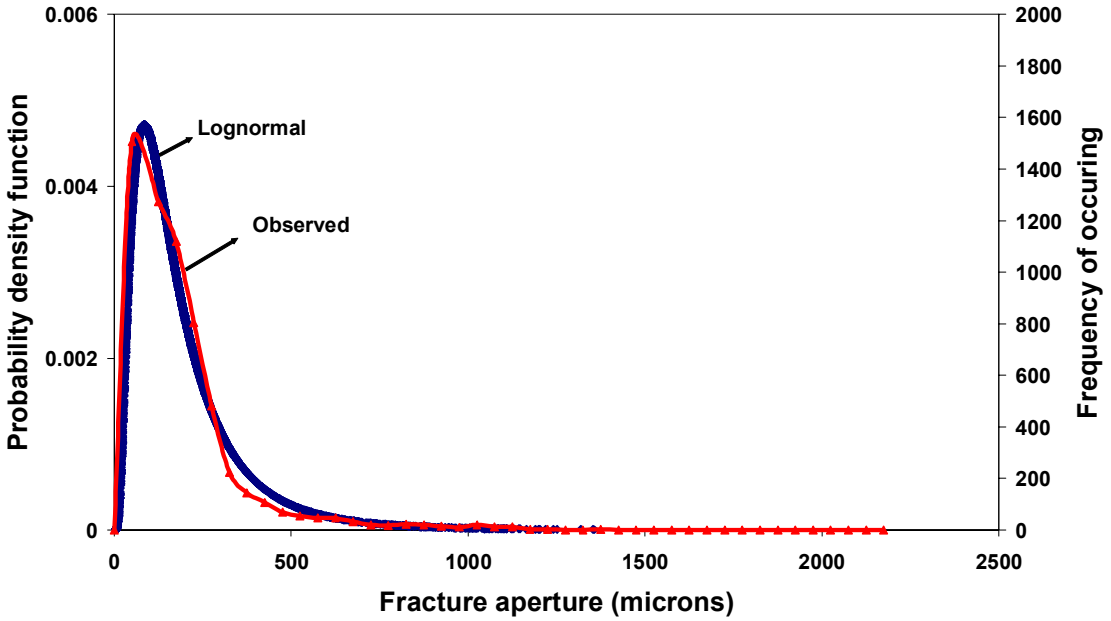

Fig. 5.41 – Comparison of observed and lognormal distributions of fracture apertures at 500 psi overburden pressure.

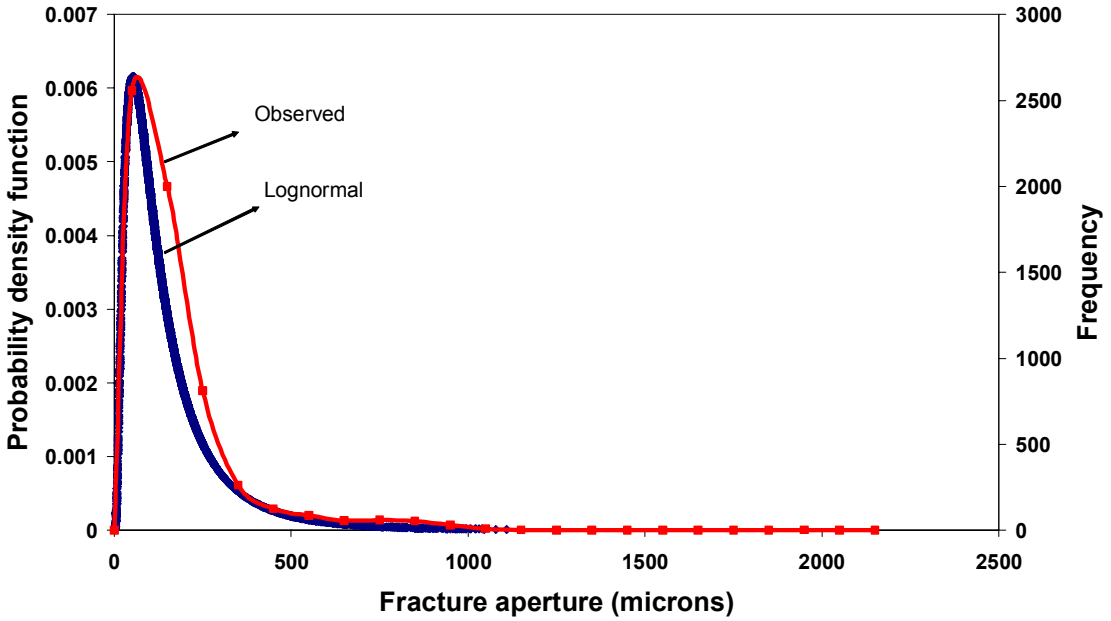

Fig. 5.42 – Comparison of observed and lognormal distributions of fracture apertures at 1000 psi overburden pressure.

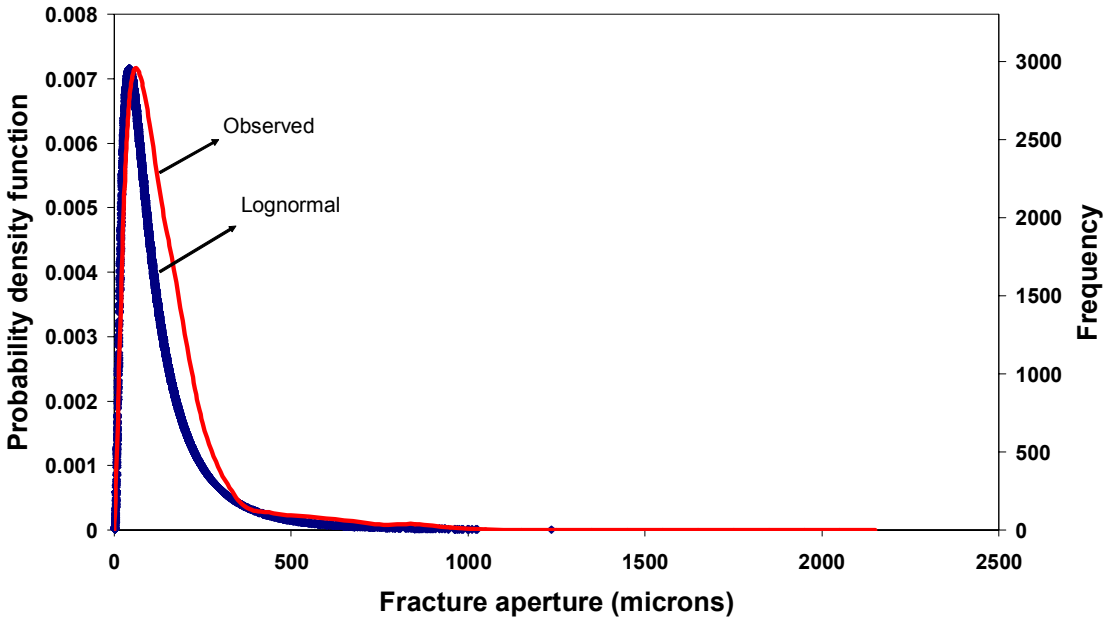

Fig. 5.43 – Comparison of observed and lognormal distributions of fracture apertures at 1500 psi overburden pressure.

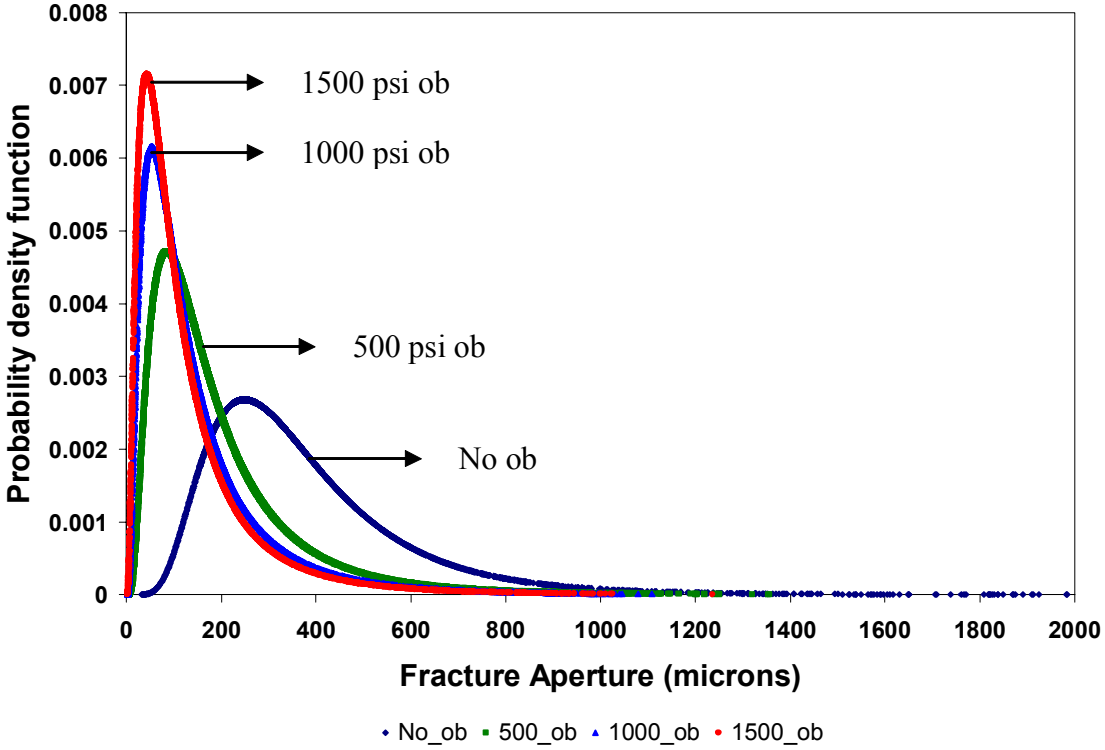

Fig. 5.44 – Comparison of lognormal distribution of fracture apertures at various overburden pressures.

CHAPTER VI

CONCLUDING REMARKS AND RECOMMENDATIONS

6.1 Conclusions

1. The change in matrix permeability with different injection rates under variable overburden pressures is not significant in contrast with that effect on fracture aperture and fracture permeability.
2. The experimental results of a core-induced fracture with high permeability matrix reveal that higher injection rates give smaller fracture aperture at constant high confining pressure.
3. The simulation model is obtained for modeling future stress-sensitive reservoirs.
4. The results also infer that the effect of stresses may be most pronounced in fractured reservoirs where large pressure changes can cause significant changes in fracture aperture and related changes in fracture permeability.
5. At high overburden pressure the influence of existing fracture permeability is not too significant. This conclusion is limited to the Berea core which has high matrix permeability.
6. The laboratory result shows that the change in overburden pressure significantly affects the reservoir properties such as fracture aperture and fracture permeability.
7. The hydrostatic stress has the greatest impact on the reduction of the matrix and fracture permeabilities and fracture aperture followed by the triaxial and uniaxial stresses.
8. Uniaxial stress condition may represent the actual condition in the reservoir while hydrostatic condition cannot represent the reservoir conditions.
9. Calibration curve is obtained for calculating fracture aperture from integrated CT signals.
10. Parallel plate approach of the fractures is no longer valid when the fracture aperture is small due to significant applied overburden pressure.
11. The simulation results suggest that a parallel plate model is insufficient to predict fluid flow in the fracture system. Consequently, the spatial heterogeneity in the

fracture aperture must be included in the modeling of fluid flow through fracture system.

12. The result of this study confirms the previous studies that fracture aperture distribution is lognormal distribution at no overburden pressure. Upon applied overburden pressure, the distribution still follows the common lognormal distribution.

6.2 Recommendations

The simulation results suggest that a parallel model is insufficient to predict fluid flow in the fracture system. Consequently, the spatial heterogeneity in the fracture aperture must be included in the modeling of fluid flow through the fracture system.

NOMENCLATURE

A = matrix area (cm^2)

f = friction factor

k_m = matrix permeability (Darcy)

k_f = fracture permeability (Darcy)

L = core length (cm)

l = diameter of the core (cm)

q_m = matrix flow rate (cc/sec)

q_f = fracture flow rate (cc/sec)

w = effective fracture width (cm)

Δp = pressure drop across the core (atm)

μ = viscosity (cp)

REFERENCES

1. Fatt, I. and Davis, D.H.: "Reduction in Permeability with Overburden Pressure," *Trans.*, AIME (1952) **195**, 329.

2. Gray H. D., Fatt, I., and Bergamini, G.: "The Effect of Stress on Permeability of Sandstone Cores," *SPEJ* (June 1963), 95-100.

3. Morita, N., Gray K. E., Srouji F. A. A., and Jogi P. N.: "Rock Property Change During Reservoir Compaction," paper SPE 13099 presented at the 1984 SPE Annual Technical Conference and Exhibition, Houston, Texas, 16-19 September.

4. Dobrynin, V. M: "The Effect of Overburden Pressure on Some Properties of Sandstones," *SPEJ* (Dec 1962), 360-366.

5. Keller, A.A.: "High Resolution CAT Imaging of Fractures in Consolidated Materials," *Int. J. Rock Mech. Min. Sci*. (1997) **34**, No. 3/4, 358-375.

6. He, M.: "Application of X-ray Tomography to Measurement of Fractures in Rocks," M.S. Thesis, Stanford University, Stanford, California (1998).

7. Bianchi, L. and Snow, D.: "Permeability Crystalline Rock Interpretated from Measured Orientations and Apertures of Fractures*," Annu. Arid Zone* (1968) **8**, No.2, 231-245.

8. Bourke, P. J., Dunance, E. M., Heath, M. J., and Hodgkinson, D. D.: "Fracture Hydrology Relevant to Radionuclide Transport, AERE *Rep.* 11414, Atomic Energy Res. Estab., Harwell, United Kingdom, 1985.

9. Tsang, Y. W. and Tsang, C. F.: "Flow Channeling in a Single Fracture as a Two Dimensional Strongly Heterogeneous Permeable Medium," *Water Resources Research* (1989) **25**, No. 9, 2076-2080.

10. Alfred, D.: "Modeling Fluid Flow Through a Single Fracture Using Experimental, Stochastic and Simulation Approaches," M.S. thesis, Texas A&M University, 2003.

11. Neuzil, C.E., and Tracy, J.V.: "Flow Through Fractures,"' *Water Resources Research* (1981) **17**, No. 1, 191-199.

12. Tsang, Y. W. and Tsang, C. F.: "Channel Model of Flow Through Fractured Media," *Water Resources Research* (1987) **23**, No.3, 467-479.

13. Wyble, D.O.: "Effect of Applied Pressure on the Conductivity, Porosity and Permeability on Sandstones," *Trans.*, AIME (1958) **213**, 430.

14. Mc Latchie, A. S., Hemstock, R. A. and Young, J. W: "The Effective Compressibility of Reservoir Rock and Its Effects on Permeability", *Trans.*, AIME (1958) **213**, 386-388.

15. Wilhelmi, B. and Somerton, W. H.: "Simultaneous Measurement of Pore and Elastic Properties of Rocks Under Triaxial Stress Conditions," paper SPE 1706 presented at the 1967 SPE Third Conference on Rock Mechanics, Austin, Texas, 25-26 January.

16. Holt, R. M.: "Permeability Reduction Induced by a Nonhydrostatic Stress Field," paper SPE 19595 presented at the 1989 SPE Annual Technical Conference and Exhibition, San Antonio, Texas, 8-11 October.

17. Zoback, M. D. and Byerlee, J. D.: "Permeability and Effective Stress," *AAPG Bulletin* (1975) **59**, 154-58.

18. Baker, W. J.: "Flow in Fissured Formations," in *Proceedings of the Fourth World Petroleum Congress*, sect. II/E, Carlo Colombo Publishers, Rome (1955), pp. 379-393.

19. Huitt, J. L.: "Fluid Flow in Simulated Fractures," *AIChE J.* (1956) **2**, 259.

20. Snow, D. T.: "Rock Fracture Spacings, Openings, and Porosities," *J. Soil Mech. Found. Div. Amer. Soc. Civ. Eng.* (1968) **94**, 73-91.

21. Gale, J. E.: "A Numerical Field and Laboratory Study of Flow in Rocks With Deformable Fractures," *Sci. Ser.* 72, Inland Waters Dir., Water Resour. Branch, Ottawa, Canada, 1977.

22. Lomize, G. M.: *Seepage in Fissured Rocks*, State Press, Moskow (1951).

23. Witherspoon, P. A., Wang, J. S. Y., Iwai, K., and Gale, J. E.: "Validity of Cubic Law for Fluid Flow in a Deformable Rock Fracture," *Water Resources Research* (1980) **16**, No. 6, 1016-1024.

24. Jones, T. A., Wooten, O. S., and Kaluza, T. J.: "Single-Phase Flow Through Natural Fractures," paper SPE 18175 presented at the 1988 SPE Annual Technical Conference and Exhibition, Houston, Texas, 2-5 October.

25. Hubbert, M. K. and Willis, D.G: "Mechanics of Hydraulic Fracturing", *Trans.*, AIME (1957) **210**, 153-168.

26. Jones, F. O: "A Laboratory Study of the Effects of Confining Pressure on Fracture Flow and Storage Capacity in Carbonate Rocks", paper SPE 4569 presented at the 1975 SPE-AIME 48th Annual Fall Meeting, Las Vegas, Nevada, Sept 30 – Oct 3.

27. Putra, E., Muralidharan, V., and Schechter, D.S.: "Overburden Pressure Affects Fracture Aperture and Fracture Permeability in a Fracture Reservoir," *SA Journal of Technology* (Fall 2003), pp 57-63.

28. Sharp, J. C.: "Fluid Flow Through Fissured Media," Ph.D. Thesis, University of London, Imp. Coll. of Science and Technology, London, 1970.

29. Schrauf, T. W. and Evans, D. D.: "Laboratory Studies of Gas Flow Through a Single Fracture," *Water Resources Research* (July 1986) **22**, No. 7, 1038-1050.

30. Johns, R. A., Steude, J. D., Castanier, L. M., and Roberts, P. V.: "Non-destructive Measurements of Fracture Aperture in a Crystalline Rock Using X-ray Computed Tomography," *J. Geophysical Research* (1993) **98**, 1899-1900.

31. Keller, A. A.: "Single and Multiphase Flow and Transport in Fractured Porous Media," Ph.D. dissertation, Stanford University, Stanford, California (1996).

32. Vinegar, H. J.: "X-ray CT and NMR Imaging of Rocks," *JPT* (March 1986), 257.

33. Wellington, S. L. and Vinegar, H. J.: "CT Studies of Surfactant- Induced CO_2 Mobility Control," paper SPE 14393 presented at the 1985 SPE Annual Technical Conference and Exhibition, Las Vegas, September 22-25.

34. Alajmi, A.F. and Grader, A.S.: "Analysis of Fracture-Matrix Fluid Flow Interactions Using X-ray CT," paper SPE 65628 presented at the 2000 Eastern Regional Meeting, Morgantown, West Virginia, October 17-19.

35. Burger, J.E., Bhogeswara R., and Mohanty K. K.: "Effect of Phase Behavior on Bypassing in Enriched Gasfloods,", paper SPE 25254 presented at the 1993 Symposium on Reservoir Simulation, New Orleans, LA, February 28 – March 3.

36. Stones, E.J., Marsden S. S., and Zimmermann S. A.: "Gravity-Induced Drainage from Fractured Porous Media," paper SPE 24042 presented at the 1992 Western Regional Meeting, Bakersfield, California, March 30 - April 1.

37. Hicks Jr., P.J., Narayanan K. R., and Deans H. A.: "An Experimental Study of Miscible Displacements in Heterogeneous Carbonate Cores Using X-ray CT," paper SPE 20492 presented at the 1990 SPE Annual Technical Conference, New Orleans, Louisiana, 23-26 September.

38. Snow, D. T.: "Anisotropic Permeability of Fractured Media," *Water Resources Research* (1969) **5**, No. 6, 1273-1289.

39. Wilson, C. R.: "An Investigation of Laminar Flow in Fractured Porous Rocks," Ph.D. dissertation, Univ. of California, Berkeley, 1970.

40. Bear, J.: *Dynamics of Fluids in Porous Media*, Elsevier, New York, 1972.

41. Tsang, Y. W. and Witherspoon, P. A.: "The Dependence of Fracture Mechanical and Fluid Properties on Fracture Roughness and Sample Size," *J. Geophys. Res.* (1983) **88**, No. B3, 2359-2366.

42. Tsang, Y. W.: "The Effect of Tortuosity on Fluid Flow Through a Single Fracture," *Water Resources Research* (1984) **20**, No. 9, 1209-1215.

43. Pyrak, L. R., Myer, L. R., and Cook, N. G. W.: "Determination of Fracture Void Geometry and Contact Area at Different Effective Stress," *EOS Trans. American Geophysical Union* (1985) **66**, No. 46, 903.

44. Gentier, S.: "Morphologie et comportement hydromécanique d'une fracture naturelle dans un granite sous contrainte normale," doctoral thesis, Univ. d'Orléans, France, 1986.

45. Moreno, L., Tsang, Y. W., Tsang, C. F., Hale, F. V., and Neretnieks, I.: "Flow and Tracer Transport in a Single Fracture: A Stochastic Model and Its Relation to Some Field Observations," *Water Resources Research* (1988) **24**, No. 12, 2033-2048.

46. Bourke, P. J.: "Channeling of Flow Through Fractures in Rock," in proceedings of *GEOVAL-87* International Symposium, Swed. Nucl. Power Inspectorate, Stockholm, Sweden, 1987.

47. Putra, E., Fidra, Y., and Schechter, D.S.: "Study of Waterflooding Process in Naturally Fractured Reservoirs from Static and Dynamic Imbibition Experiments," paper SCA 9910 presented at the 1999 International Symposium of the Society of Core Analysts, Colorado, 1-4 August.

48. Al-Harthy, S. S., Dennis, J. W., and Jing, X. D., and Marsden, J. R.: "Hysteresis, True-Triaxial Stress Path and Pore Pressure Effects on Permeability," SPE/ISRM 47269 presented at the 1998 SPE/ISRM Eurock '98, Trondheim, Norway, 8-10 July.

49. Qadeer, S., Dehgani K., Ogbe D. O., and Ostermann R. D.: "Correcting Oil/Water Relative Permeability Data for Capillary End Effect in Displacement Experiments," paper SPE 17423 presented at the 1988 SPE California Regional Meeting, Long Beach, California, 23-25 March.

APPENDIX A

PROCEDURES FOR CONDUCTING CORE FLOODING EXPERIMENTS AND PRECAUTIONS

For single phase experiments:

1. Wash the core before saturating the core at about 350°C temperature for about two days.
2. Saturate the core before starting the experiment for about two days.
3. Make sure the two valves between the pumps and the accumulators are turned off before refilling the pumps.
4. Obtain the desired overburden pressure using hydraulic jack. This may cause several attempts to stabilize, as there will be air trapped in line causing you to lose overburden pressure.
5. Fill brine in accumulator 1 and kerosene or oil in accumulator 2, if necessary.
6. Turn on the valve between the pump 1 and the accumulator 1, and turn the valves to on position on the permeameter.
7. Turn the red valve to on position, which connects accumulator 1 to the core holder. Make sure that the black valve connecting accumulator 2 and core holder is off.
8. Perform the core flooding experiment with different flow rates and note the pressure difference in the permeameter.
9. Change the overburden pressure and perform the experiment and note the readings.
10. Fracture the core and place it again in the core holder and apply overburden pressure. Close the black valve and open the red valve again and perform the core flooding experiment with brine. Note the readings.

Precautions:

1. Filter the brine to avoid any dissolved solids that choke the core.
2. Make sure the experiment is performed without any air trapped in the core.
3. While refilling the accumulators, care should be taken to close the valves between accumulator and core holder to avoid any air entering the pipelines.
4. Fracture the core as soon as possible to avoid much loss of fluid.
5. Note the volume of outlet pipeline from the core holder and subtract it from the amount of brine discharged while kerosene is injected.
6. After each flow, allow the pressure to drop close to atmospheric pressure before starting the next flow.

APPENDIX B

ERROR ANALYSIS

Any experimental data are subject to errors. So an error analysis was performed using the experimental data to quantify the range of error in the calculation of matrix and fracture flow rates. The summary of the error analysis for the injection rate case of 5 cc/min is presented in Table B.1. The parameter fracture flow rate (Q_f) in Table B.1 was calculated by subtracting the matrix flow rate from the total injection rate. From the table we find that the errors involved in the calculation of fracture flow rates are relatively small (< 8%), at lower overburden pressures (500 and 1000 psia) when compared to the high overburden pressure case (1500 psia). This indicates that the values obtained at high overburden pressure have a high degree of uncertainty.

This could be due to the fact that at high overburden pressures, the characteristics of the matrix have a dominant influence on fracture flow. Due to time constraint, the high levels of uncertainty at higher overburden pressures have not been explored or taken into account while modeling. This is an area where more analysis could be done in the future.

Table B.1 – Experimental error analysis.

Overburden Pressure, psia	K_m, md	Pressure Drop psia	Q_m cc/min	Q_m cc/min		Q_f cc/min		Error in Q_f, %
				mean	Std dev	mean	Std dev	
500.00	max = 299.96	1.00	1.21	1.44	±0.27	3.56	±0.27	7.59
		1.40	1.70					
	min= 292.44	1.00	1.18					
		1.40	1.66					
1000.00	max = 273.02	2.20	2.44	2.41	±0.11	2.59	±0.11	4.25
		2.30	2.55					
	min = 255.41	2.20	2.28					
		2.30	2.39					
1500.00	max = 240.12	4.20	4.11	4.34	±0.47	0.66	±0.47	70.68
		5.00	4.90					
	min = 222.23	4.20	3.80					
		5.00	4.53					

APPENDIX C

Table C.1 – Experimental observations for unfractured core (hydrostatic condition).

p-ob psia	Dp psi	Km md	Q CC/min
500	3.2	183.5079	5
502	6.5	180.6847	10
501	9.8	179.7628	15
500.9	13.4	175.2911	20
504	3.3	177.947	5
505.6	6.7	175.2911	10
501	9.9	177.947	15
503.3	13.5	173.9927	20
1002	3.9	150.5706	5
1004	8	146.8063	10
1001	11.8	149.2946	15
999	15.5	151.542	20
1002	4	146.8063	5
1015.7	7.9	148.6646	10
1006.6	11.9	148.04	15
1000.1	15.8	148.6646	20
1509.1	4.6	127.6577	5
1502.1	9.3	126.285	10
1500.6	13.9	126.7393	15
1508.1	18.5	126.9676	20
1510.2	4.7	124.9415	5
1499.9	9.4	124.9415	10
1501.1	14	125.834	15
1507.3	19	123.6264	20

Table C.2 – Experimental observations for fractured core (hydrostatic condition).

p-ob psia	Dp psia	Km md	Q CC/min
505	0.2	2936.126	5
498	0.5	2348.901	10
502	0.8	2202.095	15
500.1	0.9	2609.89	20
502	0.2	2936.126	5
505	0.4	2936.126	10
503.3	0.6	2936.126	15
502.7	0.8	2936.126	20
1011.9	0.6	978.7087	5
1006	1.2	978.7087	10
1003.4	1.8	978.7087	15
1001.2	2.5	939.5604	20
1001	0.7	838.8932	5
995	1.5	782.967	10
1001.3	2.2	800.7617	15
1011	2.8	838.8932	20
1501	2.7	217.4908	5
1513.3	5.5	213.5365	10
1511.3	8	220.2095	15
1509.7	11	213.5365	20
1508.2	3	195.7417	5
1507.9	6	195.7417	10
1506.5	9	195.7417	15
1502.8	12	195.7417	20

APPENDIX D

Table D.1 – Experimental observations for unfractured core (triaxial condition).

p-ob psia	Dp psia	Km md	Q CC/min
508.6	2.5	243.5375	5
506.9	4.9	248.5076	10
506	7.5	243.5375	15
506	9.8	248.5076	20
502.5	2.6	234.1706	5
502.2	5.3	229.7523	10
506	8	228.3164	15
499.6	10.3	236.4441	20
1005.1	3	202.9479	5
1002.5	6	202.9479	10
1002.4	9	202.9479	15
1004.1	12.2	199.6209	20
1004.5	3.1	196.4012	5
1013.9	6	202.9479	10
1002.3	9.1	200.7177	15
997.5	12.3	197.9979	20
1500	3.5	173.9553	5
1514.7	7	173.9553	10
1506.2	10.4	175.628	15
1502.8	14	173.9553	20
1500.8	3.6	169.1232	5
1505.3	7.1	171.5053	10
1522.4	10.7	170.7038	15
1517.3	14.5	167.9569	20

Table D.2 – Experimental observations for fractured core (triaxial condition).

p-ob psia	Dp psia	Km md	Q CC/min
499.6	0.6	1027.662	5
500.3	1.4	880.8529	10
503.9	2	924.8955	15
503.4	2.6	948.6108	20
500.3	0.7	880.8529	5
501.7	1.5	822.1293	10
501.7	2.1	880.8529	15
500.9	2.8	880.8529	20
990.6	1.6	385.3731	5
1002.6	3.2	385.3731	10
1000.7	4.9	377.5084	15
999.8	6.5	379.4443	20
1011.7	1.7	362.7041	5
1003.4	3.4	362.7041	10
1000.7	5.1	362.7041	15
1002.4	6.9	357.4475	20
1508.7	3.1	198.9023	5
1502	6.4	192.6866	10
1501.9	9.3	198.9023	15
1501.9	12.2	202.163	20
1507.9	3.3	186.8476	5
1507.4	6.7	184.0588	10
1507	9.8	188.7542	15
1507.9	13	189.7222	20

VITA

Vivek Muralidharan holds a B.E degree in mechanical engineering from the Regional Engineering College, Bhopal, India. Prior to joining TAMU he worked as an engineer with Bajaj Auto Ltd, India. He is currently involved with the U.S Department of Energy sponsored pilot project "Investigation of Efficiency Improvements during CO_2 Injection in Hydraulically and Naturally Fractured Reservoirs". His research areas include experimental analysis of petrophysical parameters using X-ray CT scanner, reservoir simulation and reservoir engineering.

His current address: Texas A&M University

Attn.: Dr. David S. Schechter

Harold Vance Department of Petroleum Engineering

3116 TAMU

College Station, TX 77843-3116

USA